

Old Dominion University

## ODU Digital Commons

---

Electrical & Computer Engineering Theses & Dissertations

Electrical & Computer Engineering

---

Fall 2017

# Computational Modeling for Abnormal Brain Tissue Segmentation, Brain Tumor Tracking, and Grading

Syed Mohammad Shamin Reza  
*Old Dominion University, sreza002@odu.edu*

Follow this and additional works at: [https://digitalcommons.odu.edu/ece\\_etds](https://digitalcommons.odu.edu/ece_etds)



Part of the [Bioimaging and Biomedical Optics Commons](#), [Computer Sciences Commons](#), and the [Pathology Commons](#)

---

### Recommended Citation

Reza, Syed M.. "Computational Modeling for Abnormal Brain Tissue Segmentation, Brain Tumor Tracking, and Grading" (2017). Doctor of Philosophy (PhD), Dissertation, Electrical & Computer Engineering, Old Dominion University, DOI: 10.25777/a851-j625  
[https://digitalcommons.odu.edu/ece\\_etds/27](https://digitalcommons.odu.edu/ece_etds/27)

This Dissertation is brought to you for free and open access by the Electrical & Computer Engineering at ODU Digital Commons. It has been accepted for inclusion in Electrical & Computer Engineering Theses & Dissertations by an authorized administrator of ODU Digital Commons. For more information, please contact [digitalcommons@odu.edu](mailto:digitalcommons@odu.edu).

**COMPUTATIONAL MODELING FOR ABNORMAL BRAIN  
TISSUE SEGMENTATION, BRAIN TUMOR TRACKING,  
AND GRADING**

by

Syed Mohammad Shamim Reza

B.Sc. June 2007, Bangladesh University of Engineering and Technology, Bangladesh

A Dissertation Submitted to the Faculty of  
Old Dominion University in Partial Fulfillment of the  
Requirements for the Degree of

DOCTOR OF PHILOSOPHY

ELECTRICAL AND COMPUTER ENGINEERING

OLD DOMINION UNIVERSITY

December 2017

Approved by:

Khan M. Iftekharuddin (Director)

Dean Krusienski (Member)

Jiang Li (Member)

Yaohang Li (Member)

## ABSTRACT

# COMPUTATIONAL MODELING FOR ABNORMAL BRAIN TISSUE SEGMENTATION, BRAIN TUMOR TRACKING, AND GRADING

Syed M. S. Reza

Old Dominion University, 2017

Director: Dr. Khan M. Iftekharuddin

This dissertation proposes novel texture feature-based computational models for quantitative analysis of abnormal tissues in two neurological disorders: brain tumor and stroke. Brain tumors are the cells with uncontrolled growth in the brain tissues and one of the major causes of death due to cancer. On the other hand, brain strokes occur due to the sudden interruption of the blood supply which damages the normal brain tissues and frequently causes death or persistent disability. Clinical management of these brain tumors and stroke lesions critically depends on robust quantitative analysis using different imaging modalities including Magnetic Resonance (MR) and Digital Pathology (DP) images. Due to uncontrolled growth and infiltration into the surrounding tissues, the tumor regions appear with a significant texture variation in the static MRI volume and also in the longitudinal imaging study. Consequently, this study developed computational models using novel texture features to segment abnormal brain tissues (tumor, and stroke lesions), tracking the change of tumor volume in longitudinal images, and tumor grading in MR images. Manual delineation and analysis of these abnormal tissues in large scale is tedious, error-prone, and often suffers from inter-observer variability. Therefore, efficient computational models for robust segmentation of different abnormal tissues is required to support the diagnosis and analysis processes. In this study, brain tissues are characterized with novel computational modeling of multi-fractal texture features for multi-class brain tumor tissue segmentation (BTS) and extend the method for ischemic stroke lesions in MRI. The robustness of the proposed segmentation methods is evaluated using a huge amount of private and public domain clinical data that offers competitive performance when compared with that of the state-of-the-art methods. Further, I analyze the dynamic texture behavior of tumor volume in longitudinal imaging and develop post-processing framework using three-dimensional (3D) texture features. These post-processing methods are shown to reduce the false positives in the BTS results and improve the overall segmentation result in longitudinal imaging. Furthermore, using this improved segmentation results the change of tumor volume has been quantified in three types such as stable, progress, and shrinkage as observed by the volumetric changes of different tumor tissues in longitudinal images. This study also investigates a novel non-invasive glioma grading, for the first time in literature, that uses structural MRI only. Such non-invasive glioma grading may be useful before an invasive biopsy is recommended. This study further developed an automatic glioma grading scheme using the invasive cell nuclei morphology in DP images for cross-validation with the same patients. In summary, the texture-based computational models proposed in this study are expected to facilitate the clinical management of patients with the brain tumors and strokes by automating large scale imaging data analysis, reducing human error, inter-observer variability, and producing repeatable brain tumor quantitation and grading.

© 2017

Syed Mohammad Shamim Reza

All Rights Reserved

## ACKNOWLEDGEMENTS

I would like to express my sincere gratitude to my advisor, Dr. Khan M. Iftekharuddin, for giving me the opportunity to work in his research group and providing guidance and advice with enthusiasm and patience. My special thanks to the members of my dissertation committee, Dr. Dean Krusienski, Dr. Jiang Li, and Dr. Yaohang Li for their time and willingness to advise on and review the dissertation. Their thoughtful comments had significant effects on the quality of this thesis. Throughout the course of my Ph.D. program, I have had the opportunity to work in a multidisciplinary research team, collaborate with external professionals in different hospitals, and play the lead role in several research activities toward the completion of my Ph.D. My profound appreciation goes to Dr. Atiq Islam who laid the foundation of tumor detection work that helped me to explore the field. I would like to thank our clinical collaborators Dr. Arastoo Vossough, Dr. Karra Jones, and Dr. James Chen for their generous time and support that helped me to understand the clinical significances of this study. My special thanks to my colleague, Linmin Pei, for helping me in pre-processing the huge amount of MRI images and all the members of the Old Dominion University Vision Lab for providing me a great deal of knowledge and instructions. I respectfully acknowledge my parents and relatives in my home country for their constant inspiration and encouragement. My American and international friends from different countries have been wonderful companions and have helped me beyond my studies. Finally and most importantly, I would like to thank my wife for her tremendous support and patience during my Ph.D. program.

## TABLE OF CONTENTS

	Page
LIST OF TABLES .....	vii
LIST OF FIGURES .....	viii
<b>Chapter</b>	
1 INTRODUCTION .....	1
1.1 PROBLEM STATEMENT AND DISSERTATION GOALS .....	3
1.2 ORGANIZATION OF THE DISSERTATION .....	8
2 BACKGROUND REVIEW .....	9
2.1 RELATED WORK IN ABNORMAL TISSUE SEGMENTATION .....	9
2.2 LONGITUDINAL TUMOR SEGMENTATION .....	11
2.3 GLIOMA GRADING .....	12
3 MULTI-RESOLUTION TEXTURE FEATURE FOR AUTOMATIC SEGMENTATION OF BRAIN ABNORMAL TISSUES .....	14
3.1 CHAPTER OVERVIEW .....	14
3.2 METHODOLOGY .....	14
3.3 RESULTS .....	22
3.4 ISCHEMIC STROKE LESION SEGMENTATION .....	27
4 LONGITUDINAL BRAIN TUMOR VOLUME SEGMENTATION AND TRACKI- NG USING 3D TEMPORAL HIERARCHICAL TEXTURE FEATURES IN MRI .....	31
4.1 CHAPTER OVERVIEW .....	31
4.2 THREE-DIMENSIONAL TEXTURE ANALYSIS .....	31
4.3 METHODOLOGY .....	37
4.4 EXPERIMENTS AND RESULTS .....	41
4.5 TRACKING THE CHANGE OF TUMOR VOLUME .....	54
4.6 DISCUSSION .....	59
5 TEXTURE-BASED RADIOMICS FOR GLIOMA GRADING AND VALIDA- TION USING HISTOPATHOLOGY IMAGES .....	61
5.1 CHAPTER OVERVIEW .....	61
5.2 NON-INVASIVE GLIOMA GRADING METHOD .....	61
5.3 AUTOMATIC GRADING USING DIGITAL PATHOLOGY IMAGES .....	68

	Page
5.4 EXPERIMENTS AND RESULTS .....	72
5.5 DISCUSSION.....	82
6 CONCLUSION AND FUTURE WORKS.....	83
6.1 CONCLUSION.....	83
6.2 FUTURE WORKS .....	84
BIBLIOGRAPHY .....	87
VITA .....	94

## LIST OF TABLES

Table	Page
1	Diversity in location, size and number of stroke lesions that represents the difficulties involved in the lesion segmentation task.....4
2	A quick look of all the proposed goals in the dissertation .....5
3	Average quantitative scores (Dice, Sensitivity) of multi-class tumor tissue segmentation (3-fold) in training dataset .....25
4	Average quantitative scores (Dice, Sensitivity) of multi-class tumor tissue segmentation using 213 patients as test dataset .....26
5	Final ranking of multimodal brain tumor segmentation (BRATS) 2013.....26
6	Patient-wise quantitative (Dice) scores of ischemic stroke (sub-acute) lesion segmentation results..... 29
7	Ranking of ISLES-2015 Sub-acute stroke lesion segmentation challenge.....30
8	Comparison of the quantitative scores for the original BTS segmentation and the improved result using the proposed 3D texture-based post-processing method.....53
9	Quantitative scores, subjects and designs for grading..... 82
10	Summary of the research findings related to the proposed method.....85



## LIST OF FIGURES

Figure	Page
1 Statistics on tumor in brain and other central nervous system from the fact sheet of National Cancer Institute .....	1
2 Variation in shape, size and location of different abnormal tissues in brain .....	3
3 Multi-tissue brain abnormal tissue segmentation pipeline .....	15
4 Example images of standard MRI preprocessing .....	16
5 Illustration of fractal PTPSA feature extraction process from a sub-image .....	18
6 Simulation of $fBm$ process using different <i>Hurst</i> , $H$ index, which determines the variation of signal roughness .....	18
7 Algorithm for tissue texture extraction using the $mBm$ process .....	20
8 Example images of multi-tissue (Edema, Necrosis, Enhanced and non-Enhanced active tumor) segmentation in training dataset .....	23
9 Example images of multi-tissue (Edema, Necrosis, Enhanced and non-Enhanced active tumor) segmentation in test dataset .....	24
10 Generalized flow diagram for ischemic stroke lesion segmentation.....	27
11 Example images of segmented lesions for two random patients .....	28
12 Example images at two time points for GBM tumors and MS lesions .....	32
13 Illustration of three dimensional spin image feature extraction .....	33
14 Algorithm for the 3D Spin image feature extraction.....	34
15 Illustration of three dimensional RIFT feature extraction process .....	35
16 Algorithm for the 3D RIFT texture feature extraction.....	35
17 Three dimensional LBP-TOP feature extraction process .....	36
18 The LBP-TOP texture extraction process.....	37
19 Simplified flow diagram of the proposed method for improving the brain tumor segmentation in longitudinal images .....	38
20 Demonstration of ROI for hierarchical feature extraction .....	39
21 Example images of BTS outcomes with the appearance of significant false positives.....	42
22 Three dimensional view of the false positives in BTS outcomes and the ground-truth.....	43
23 Data distribution for training, validation, and test for hierarchical texture feature extraction .....	44
24 Classifiers performance using the hierarchical texture features .....	45
25 Demonstration of finding optimal threshold.....	49
26 Improved segmentation outcomes using hierarchical texture-based post-processing method .....	50
27 Three dimensional visualization of the improved segmentation result.....	51
28 Plots of the quantitative scores of the improved segmentation results using the proposed.....	52
29 Example of some problematic images (imaging artifacts) in BRATS-2015 dataset	54
30 Plots of the volumetric changes in the longitudinal images.....	55

	Page
31	Original tumor volumes in longitudinal images of a patient..... 57
32	Overall flow diagram for automatic segmentation and classification of tumor grades in MR images ..... 62
33	Modified algorithm for texture extraction to classify brain gliomas using mBm process..... 63
34	Algorithm of feature extraction using Multifractal detrended fluctuation analysis (MFDFA)..... 65
35	Plots of significant features for grading brain gliomas in MR images using MFDFA..... 65
36	Framework for dynamic texture analysis using linear dynamic system ..... 66
37	Algorithm for dynamic texture analysis to extract useful feature..... 67
38	Algorithm for exhaustive feature search ..... 68
39	The significant presence of elongated nuclei in GBM in compared to LG images..... 69
40	The overall flow diagram for grading brain gliomas in digital pathology images..... 70
41	Example images of step by step nuclei segmentation in Digital Pathology images..... 72
42	Example images of tumor segmentation using BTS with the ROI for dynamic texture analysis ..... 74
43	Pole locations ( $\lambda_{max\_avg}$ ) of GBM and LG patients..... 75
44	K-mean cluster centroids that used as a final features for grading in pathology images..... 77
45	Classification performance of the optimal feature combinations using exhaustive feature search for classifying GBM/LG in MR images..... 78
46	Classification performance of the optimal feature combinations using exhaustive feature search for classifying GBM/LG in DP images..... 79
47	Corresponding ROC curve of LOO cross validation of proposed HG/LG grading..... 80
48	Corresponding ROC curve of LOO cross validation of proposed GBM/LG grading..... 81

## CHAPTER 1

### INTRODUCTION

Despite incredible advancements in medical imaging, diagnosis and the knowledge of human physiology, the prevalence of cancer in the brain or other central nervous system (CNS) is consistent over the last few decades. According to National Cancer Institute (NCI) [1], the number of new cases of brain and other CNS cancer is 6.4, and the number of deaths is 4.3 per 100,000 men and women per year during 2010-2014. Based on 2012-2014 data, approximately 0.6 percent of men and women are to be diagnosed with brain and other nervous systems at some point during their lifetime. In 2017, an average 23,800 estimated new cases are going to be added while 16,700 is the number of estimated deaths in the United States. Figure 1 shows the statistics of cancer in the brain and other CNS.

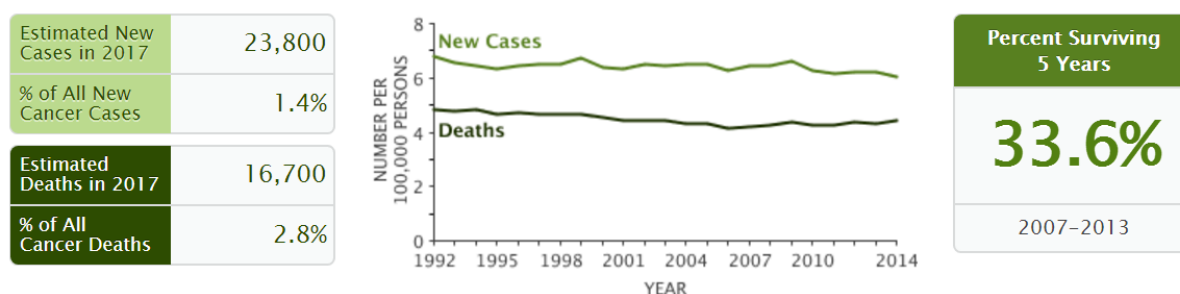


**Figure 1:** Statistics on tumor in brain and other central nervous system from the fact sheet of National Cancer Institute [1].

The above statistics on cancer in the brain and other CNS tumors clearly indicates that robust and efficient computational models are desired to improve the diagnosis and analysis processes. According to National Stroke Association [2], another life threatening incident is brain stroke that occurs due to sudden interruption or reduction of the blood supply to part of the brain or bleeding into or around the brain. As a consequence, the brain cells die or damage severely for receiving a lack of enough oxygen and nutrients. There are two forms of stroke; ischemic - blockage of a blood vessel supplying the brain, and hemorrhagic - bleeding into or around the brain. Brain stroke is one of the major causes of frequent death and persistent disability in the industrial countries [3]. Patients with cancer or experienced disability due to stroke are associated with high socioeconomic costs for their continuous treatments and cares. In regular clinical settings, different imaging modalities such as MR, DP, computerized tomography (CT), ultrasound etc. are used to diagnose the tumor, whereas MR is mostly common for brain tumor

imaging. Processing and analyzing the large set of images require efficient computer aided diagnosis techniques. Precise detection and segmentation of brain abnormal tissues (tumor, stroke) and different tumor tissues such as necrosis, edema, active tumor, cysts etc. in the MR images is the precondition for a reliable diagnosis. Further analysis using the segmented tumor volume provides essential information about the current stage, grade, and progress of the tumor, which in turn helps to determine the treatment procedure. There are two basic kinds of brain tumors – primary and metastatic [4]. Primary brain tumors originate and grow in the brain locally whereas the metastatic tumor originate in another part of the body but drift to spread in the brain. Disregarding their origination, all type brain tumors grow with an unpredictable and complex appearance in shape, size, and location. Due to the infiltration through different tissues, variation in intensities in the images, automatic tumor segmentation becomes a challenging task in the area of medical image analysis. Many different automatic brain tumor segmentation techniques proposed in the literature are based on either features, or atlas-dependent registration, or a combination of both. Feature-based segmentation methods extract and analyze different features extracted from the images whereas atlas-based method perform registration patient images with a template (atlas) image. The critical factor for atlas-based method is that it needs a sophisticated and careful registration of the images. The argument is that the complex structure of brain tumor in MRI may be more amenable to multi-resolution texture analysis. The success of multi-resolution texture-based brain tumor segmentation works [5][6][7] drive the motivation to extend the texture based method for ischemic stroke lesion segmentation. The extensions of BTS lie in using the diffusion weighted images and extracting structure tensor based local gradient information as a feature. Among all the primary brain tumors, gliomas are most frequent in adults which originate in the glial cells and show a wide range of aggressive infiltration [8] among the surrounding tissues. While the slower growing (grade I and II) astrocytomas or oligodendrogliomas have several years of survival period, the more aggressive (grade IV) glioblastoma multiforme (GBM) has less than a two year survival period. In the context of glioma analysis, it is very common to have multiple images of the same patient over time (longitudinal images). Specifically for GBM, it is important to monitor tumor progression over time and determine the treatment procedure and dose medication accordingly or to monitor whether the tumor has recurred. Despite considerable advances in tumor research, the use of their temporal information from longitudinal images is very rare. But it is intuitive that leveraging this temporal information can improve the segmentation accuracy by helping detect the potential tumor candidates from a high false positive (FP) outcomes. Therefore, this study focuses on using this temporal information by modeling the temporal texture behavior of the tumor to reduce the false positives from our original BTS outcomes. Another important diagnosis process is grading of the tumor, usually is an invasive process that relies almost entirely on the visual assessment of the tumor specimen under a microscope. However, the usual tumor grading procedure raises the concern of subjectivity and inter-observer variability; and clearly demands an efficient non-invasive method. Since gliomas are the most common forms of life-threatening tumors in the CNS, it is important to stratify these gliomas into two major groups GBM versus low-grade (LG) or high-grade (HG) versus LG to better understanding the disease progression, life expectancy, and eventually to facilitate plans for treatment. Depending

on the aggressiveness in cell reproduction rate and infiltration into the surrounding tissues the World Health Organization’s (WHO) grading scale [9] defines four grades (I-IV) of gliomas. The LG gliomas (grade I & II), such as low-grade astrocytomas and oligodendrogliomas that account for 10% [10] of primary brain tumors, are usually slow growing and involve the least malignancy. The HG gliomas (grade III and IV) show more abnormal cell reproduction rate and account for approximately 60-75 % [10] of the glioma cohorts. Specifically, the GBM (grade IV) is the most malignant and rapidly growing tumor in the adult brain. However, in regular clinical practice grading is an invasive process and relies on the visual observation of microscopy tissue slide images. This work proposes a novel non-invasive glioma grading using structural MR images that may be useful before an invasive biopsy is recommended. The proposed method suggests that grading of glioma tumors is possible using novel radiomic texture features in MRI. This dissertation also proposes a computationally efficient cell nuclei morphologic feature analysis technique for grading brain gliomas into GBM versus LG in tissue slide DP images.

## 1.1 PROBLEM STATEMENT AND DISSERTATION GOALS

The above discussions demand highly efficient automatic computational models being evaluated with a large scale multi-center dataset. Automatic processes are well known for their fast and accurate reproducibility. In the case of handling large scale data and finding the intrinsic properties from those big data, a fully automatic process is the ultimate choice. However, automatic computation of brain abnormal tissues is always challenging due to their unpredictable appearance with a wide range of variation in size, shape, location, and number. Figure 2 shows example images having the tumor with different size and shapes.

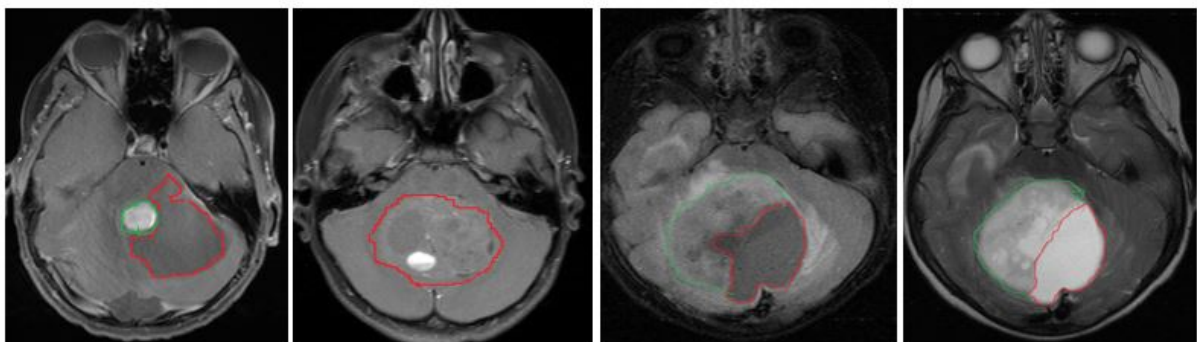


**Figure 2:** Variation in shape, size and location of different abnormal tissues in brain. Tumor core (red) and edema (green).

Especially, in the case of ischemic stroke lesion (sub-acute), the strong diversity emphasizes the difficulty of the segmentation task. Table 1 shows the characteristics diversity of sub-acute ischemic stroke lesions present in 64 patients used in the ISLES-2015 challenge [3].

**Table 1:** Diversity in location, size and number of stroke lesions that represents the difficulties involved in the lesion segmentation task. Lesions diversity is summarized for 64 sub-acute ischemic stroke lesion cases in the ISLES-2015 challenge dataset. The strong diversity represents the difficulties involved in the lesion segmentation task.  $\mu$  denotes the mean value,  $[\min, \max]$  is the interval and the total number of lesion counted in the dataset, anterior cerebral artery (ACA), middle cerebral artery (MCA), posterior cerebral artery (PCA) and basilar artery (BA).

Lesion count	$\mu = 2.49$ [1, 14]
Lesion volume	$\mu = 17.59ml$ [0.001, 346.064]
Haemorrhage present	$n = 12$ 0=yes, 1=no
Non-stroke white matter lesion load	$\mu = 1.34$ 0=none, 1=small, 2=medium, 3=large
Lesion localization (lobes)	$n_1 = 11, n_2 = 24, n_3 = 42, n_4 = 17, n_5 = 2, n_6 = 6$ 1=frontal, 2=temporal, 3=parietal, 4=occipital, 5=midbrain, 6=cerebellum
Lesion localization (cortical/subcortical)	$n_1 = 36, n_2 = 49$ 1=cortical, 2=subcortical
Affected artery	$n_1 = 6, n_2 = 45, n_3 = 11, n_4 = 5, n_5 = 0$ 1=ACA, 2=ACM, 3=ACP, 4=BA, 5=other
Midline shift observable	$n_0 = 51, n_1 = 5, n_2 = 0$ 0=none, 1=slight, 2=strong
Ventricular enhancement observable	$n_0 = 38, n_1 = 15, n_2 = 3$ 0=none, 1=slight, 2=strong
Laterality	$n_1 = 18, n_2 = 35, n_3 = 3$ 1=left, 2=right, 3=both

The presence of MR imaging artifacts such as intensity inhomogeneity and the bias of the magnetic field makes the automatic computation more challenging. Furthermore, noise in the images, patient movement at the time of acquisition makes the automatic processing challenging. Uneven contrast enhancement and different settings of acquisition parameters across the multi-center datasets further complicates the computational modeling for a consistent performance over the whole dataset. Consequently, state-of-the-art automatic segmentation and classification methods suffer from false positives and inconsistency even in the follow-up images. This study proposes computational models for automatic segmentation, tracking, and grading of brain lesions. Several experiments are performed and validated with large-scale dataset related to few of the above challenges. The first goal of this dissertation is to obtain a robust automatic segmentation method for abnormal brain tissues. The detail multi-resolution analysis of multi-fractal Brownian motion (mBm) [5] enables to capture the randomly varying spatial tumor texture at different scales. In this work, using these sophisticated texture features such as fractal piece-wise triangular prism surface area (PTPSA) [11] and mBm along with intensity is used for characterizing the different abnormal brain tissues such as tumor and lesions.

The second goal of this dissertation is designed to reduce the FPs from the outcomes of the automatic segmentation method proposed in the first goal. A complete post-processing scheme has been developed using the temporal behavior of texture variation in longitudinal images. Despite considerable advances in tumor research, the use of temporal information from the longitudinal image is very infrequent. However, it is intuitive that leveraging this temporal information can improve tissue segmentation accuracy by helping to detect the potential tumor candidates with high false positive values. The improved segmentation method is then used for longitudinal tumor volume assessment which requires consistent segmentation performance among the follow-up images. In the third goal, 3D texture feature-based novel non-invasive glioma grading using only structural MR images is proposed in order to provide a useful grading tool that may be useful before an invasive biopsy is recommended. A combination of novel radiomic texture features in MRI are developed to characterize tumor texture. Tumor grading from microscopy tissue slide images is an invasive diagnosis process to assess tumor progression, proliferation, and invasion. Many automatic cyto-/histological image analysis methods have been reported in the literature for classification of breast cancers, follicular lymphoma, bone marrow, and brain tumors. The goals of this dissertation are summarized in Table 2.

**Table 2:** Proposed goals in this dissertation.

<b>Dissertation Goals</b>	<b>Description</b>	<b>Proposed Methods</b>
Multi-tissue BTS and lesion segmentation	Multiclass abnormal tissue (edema, necrosis, enhanced and non-enhanced) segmentation.	Novel texture features (mBm, PTPSA). Random Forest (RF) as classifier.
	Ischemic stroke lesion (sub-acute) segmentation.	Structure tensor based local gradient, mBm, and PTPSA texture features. RF as classifier.
Improved BTS using 3D texture features for tumor volume tracking	Improved BTS in longitudinal MRIs	Original BTS with longitudinal information, False positive reduction using Spin image, RIFT, LBP feature. Relevance Vector Machine (RVM) and RF as classifier.
	Tracking the Tumor volume as stable, progress or shrinkage.	Ratio of the tumor volumes in the follow-up images.
Tumor grading using texture radiomics and its validation using histopathology data	Non-invasive grading using only structural (T1c, T2, Flair) MR images.	Dynamic texture, MFDFFA, and mBm features. Support Vector Machine (SVM) as classifier.
	Invasive grading in histopathology images.	Cell nuclei morphology with k-mean clustering. SVM as classifier.

This dissertation proposes several texture-based computational models for analyzing brain tumors. First a texture-based computational model is proposed for effective segmentation of brain abnormal tissues (tumor, stroke lesion) in multi-modal MR images. The proposed texture based method has been improved with a complete post-processing using three dimensional hierarchical texture features in longitudinal MRIs. The volumetric ratios of the tumor tissues in the longitudinal images are used to propose a method for tracking the change of tumor volume in longitudinal images. The consistency of the improved segmentation result in the follow-up images is the key for such tumor tracking. Finally, texture based non-invasive grading method has been proposed and validated with an invasive grading scheme. The contributions of this dissertation can be summarized as follows:

*An efficient multi-class tumor tissue and ischemic stroke lesion segmentation method*

While the previous works [12] [5] studied the effectiveness of the multi-resolution texture for segmenting posterior-fossa tumor in [12] and different types of tumor such as medulloblastoma, astrocytoma and low-grade gliomas [5], this study extends texture feature-based technique for multiclass tumor tissue (necrosis, edema, enhances, and non-enhanced) segmentation. In the prior work [5], SVM is exploited as weak classifier with a novel modified Adaboost algorithm for two-class (e.g. tumor and rest of the brain) tissue segmentation. In contrast, this work involves Random Forest [13] as the classifier for its excellent multiclass handling capability. Furthermore, the method has been successfully extended for ischemic stroke lesion segmentation. The extensions lie in the MR image intensity inhomogeneity correction, adding new features and feature ranking. In this work, the brain abnormal tissues (tumor, lesion) are characterized using local texture features; PTPSA, mBm, structure tensor based local gradient with global features like regular intensities, and intensity differences of MRI modalities. Finally, extensive state-of-art comparison by participating multiple global tissue segmentation challenges is performed to ascertain the effectiveness of the proposed technique.

*The first method uses three dimensional hierarchical texture features to improve tumor segmentation*

This study focuses on using the temporal information from longitudinal images. Due to their uncontrolled growth and infiltration into the surrounding tissues, the tumor regions appear with a significant texture variation in longitudinal imaging while the texture of non-tumor regions remains fairly same. Analyzing this temporal behavior using specific 3D texture features such as spin image [14][15], rotation invariant feature transform (RIFT) [15] and local binary profile (LBP) [16] may be useful to discriminate the original tumor volumes from the pool of non-tumors. While these features are widely used in computer vision algorithms for different types of object recognition, this work uses these texture features in tumor analysis for possibly the first time. We extend the 2D spin image and RIFT features into 3D, and added the LBP of three orthogonal planes (LBP-TOP) [17] features and develop an effective post-processing method to reduce the false positives. In addition, the method quantifies the pattern of tumor volume change as stable, progressing, and shrinking using the volumetric ratios of different tumor tissues.



*Non-invasive grading method using only structural MR images*

This study proposes a non-invasive glioma grading method using commonly available structural MRI. Although few non-invasive methods using advanced MRI modalities (perfusion, spectroscopy etc.) with structural images are found in the literature, this is the first method that uses structural MRI only. The proposed method is further validated using DP images. This work proposes novel non-invasive glioma grading using structural MR images that may be useful before an invasive biopsy is recommended. The proposed method suggests that grading of glioma tumors is possible using novel radiomic texture features in MRI. Tumor texture is characterized by employing a combination of dynamic texture (DT) analysis [18], Multi-fractal Detrended Fluctuation Analysis (MFDFA) [19], and mBm. For the first time in the literature, DT has been used in medical MR image analysis and MFDFA in brain tumor analysis through this work.

*A novel technique to analyze the cell nuclei morphological features for glioma grading in DP images*

In this work, a novel glioma grading technique using cell nuclei morphology in DP image is also proposed. The contribution of the method is in extracting representative features by k-mean clustering of nuclei morphologic features including area, perimeter, eccentricity, and major axis length. This clustering based representative feature extraction avoids shortcomings of extensive tile [20][21] and nuclear score [22] based methods for brain glioma grading in pathology images.

*Validation of proposed non-invasive grading in MR with the invasive method in DP images using the corresponding dataset of common patients*

As discussed above, few non-invasive grading methods are found in the literature using the advanced MRI modalities (e.g., perfusion, spectroscopy) which are not commonly practiced in regular clinical settings. Moreover, none of their performances are validated with the regular invasive grading results using DP images. In this work, performance of the proposed non-invasive grading is validated with that of the proposed invasive one.

## **1.2 ORGANIZATION OF THE DISSERTATION**

The rest of the dissertation is organized as follows. Chapter 2 provides a background review on automatic segmentation of multi-class tumor tissues, stroke lesions, quantification of tumor growth in longitudinal images and non-invasive glioma grading in multimodal MR images. Chapter 3 proposes novel texture feature-based brain abnormal tissue and ischemic stroke lesion segmentation in multimodal MR images. State-of-the-art comparison, ranking and results in multiple global tissue segmentation challenges of the proposed segmentation methods are also provided in Chapter 3. Chapter 4 investigates the efficacy of the proposed 3D texture feature-based post-processing method to reduce the FPs from BTS outcome. Computational

models for tumor growth estimation using the different tumor tissues volumetric ratio is also proposed in this chapter. The study of non-invasive glioma grading using specific radiomic features is provided in Chapter 5 with the experimental results of HG versus LG and GBM versus LG. The automatic glioma grading using cell nuclei morphological features for GBM versus LG in DP images is provided. The validation of the non-invasive grading performance with that of the invasive method is also provided in Chapter 5. The dissertation concludes with future plans in Chapter 6.

## CHAPTER 2

### BACKGROUND REVIEW

This chapter reviews the relevant previous work on tumor segmentation, tracking, and grading in MR images.

#### 2.1 RELATED WORK IN ABNORMAL TISSUE SEGMENTATION

##### 2.1.1 AUTOMATIC TUMOR SEGMENTATION

Over the last decade, clinical studies related to brain tumor quantification in medical images have increased significantly. About one fourth of these studies involve automatic segmentation of tumors. Numerous algorithms for automatic, semi-automatic, and interactive segmentation of brain tumors are found in the literature. Due to the unpredictable and complex appearance of the brain tumors, researchers have been studying both generative and discriminative approaches to address this challenging segmentation task [4]. Generative methods usually combine domain-specific prior knowledge with the tissue anatomy and appearance of the brain to obtain automated segmentations. Atlas-dependent registration is one of the generative methods that register the tumor image with the brain atlas, where the atlas is composed of healthy or diseased developing or adult human brain. Although generative methods often offer good generalization to unseen images, encoding prior knowledge is difficult. On the other hand, discriminative approaches directly learn from the image intensities and its corresponding segmentation labels without any prior knowledge. In addition to the image intensities, useful features are also incorporated in the discriminative methods. Since the developed texture-based tumor segmentation method is a feature-based method, briefly a literature review on recent-feature based techniques is provided. Among the recent feature-based techniques, Lee et al. [23] propose support vector machine (SVM) based discriminative random fields with a set of multi-scale image and spatial alignment driven features, spatial probabilities of normal tissues (white matter, gray matter, cerebrospinal fluid), spatial expected intensity maps, and a left-to-right symmetry characteristics. However, the method does not allow training and inter-patient testing across the different patients. Corso et al. [24] use the conditional random field (CRF) in modeling a cascade of boosted discriminative classifier. Popuri et al. [25] study Dirichlet-priors, Gabor-like texton [26], and level-set features to build a statistical model for brain tissues. However, level-set techniques are very sensitive to initialization and tend to suffer from boundary leaking problems. Zikic et al. [27] use spatial non-local features and initial probabilities with the classification forest (CF) to segment the brain tumor. Bauer et al. [28] integrate random forest (RF) classification with hierarchical CRF

regularization in an energy minimization scheme. In [29], Geremia et al. introduce a symmetry feature and use discriminative random decision forest for voxel-wise classification of tumor voxels. Tustison et al. [30] use Gaussian mixture model (GMM) and maximum a priori estimation using Markov random fields (MAP-MRF) to generate connected component based geometric features for brain tumor classification. Meier et al. in [31] extend the discriminative model [32], to a generative-discriminative hybrid model which generates initial tissue probabilities for enhancing the classification and spatial regularization. The authors extract 44 features including first-order texture, gradient information, symmetry features and 7 voxel-wise tissue probabilities for brain tumor segmentation. Other important texture-based techniques are also found in the literature. Ghoneim et al. [33] have proposed a 3D co-occurrence matrix-based texture analysis to classify gliomas. However, they use a manually segmented volume for the region of interest. Pachai et al. [34] have shown a multi-resolution pyramid algorithm to segment multiple sclerosis lesions in brain MR image. Pitiot et al. [35] present a texture-based MR image segmentation approach with a novel combination of two-stage hybrid neural classifier. However, none of the above features capture the multi-resolution spatially varying properties of the brain tissues. This study argues that the complex structure of brain tumor in MRI may be more amenable to multi-scale spatially variable texture analysis such as PTPSA [11] and mBm [5]. The detail multi-resolution analysis of fractal feature such as mBm [16] enables capturing the randomly varying spatial tumor texture at different scales. In our prior work [12], we study the effectiveness of these features and feature selection methods for segmenting posterior-fossa tumor. In [5], we show that fractal feature based technique is also efficient in segmenting different types of tumor such as medulloblastoma, astrocytoma and LG gliomas. In [6], [7], these sophisticated texture features; fractal PTPSA and mBm along with intensity and intensity differences among the modalities are used to analyze multimodal MRI for characterizing the different abnormal and normal brain tissue.

### 2.1.2 ISCHEMIC STROKE LESION SEGMENTATION

In recent years, quantification of stroke lesions has gained increasing attention. However, efficient automatic segmentation is still required. Stroke lesion segmentation is very challenging not only for their diverse characteristic (Table 1) but also their acquisition time-dependent appearance in MR images. A collection of recent studies for stroke lesion segmentation is found at the ischemic stroke lesion segmentation challenges (ISLES-2015) [3]. Among the automatic algorithms, both generative probabilistic (Derntl et al. [36], Menze et al. [4], Forbes et al. [37], Kabir et al. [38], Martel et al. [39]) and discriminative in a pattern classification frame-work (Maier et al. [40],[41]) are found. However, due to the strong diversity of the used dataset, state-of-the-art comparison with their advantages and disadvantages are tough to explain. This study also extends the proposed BTS method by adding local gradient features and diffusion-weighted imaging (DWI) for sub-acute ischemic stroke lesion segmentation.

## 2.2 LONGITUDINAL TUMOR SEGMENTATION

In the context of glioma analysis, it is very common to have multiple images of the same patient over time (longitudinal images). Specifically for GBM, it is important to monitor tumor progression over time and determine the treatment procedure and dose medication accordingly or monitor whether the tumor has recurred. Detailed segmentation of brain tumor and its different tissues (necrosis, edema, enhanced active, cyst etc.) is the precondition for a reliable diagnosis such as growth monitoring, dose determination, and estimating drug and therapy response. A number of state-of-the-art segmentation methods of brain tumors, as well as classification of different tumor tissues, have been found in the literature, whereas many of them have been reported at the annual workshop on Multimodal Brain Tumor Segmentation (BRATS) challenges [4]. However, most of these methods are designed to take input MR scans in a time-independent framework without accounting for the longitudinal information. Moreover, most of the post-processing techniques mentioned in these studies are not clearly outlined and thus suffer a lack of reproducibility. It is intuitive that over the time the texture of the tumor region changes due to uncontrolled growth while the non-tumor regions remain the fairly same. Specific features that quantify this temporal information may be useful in modeling a generalized post-processing technique to discriminate the tumor volumes from the non-tumor volumes. Recently, quantification of longitudinal changes in brain MRI has been investigated in few studies. Chitphakdithai et al. [42] performed registration among the follow-up MR scans and analyze the label changes between the two consecutive scans for metastatic tumor tracking. However, due to irregular appearance and fast evolution of GBM, registration methods are not well suited. Elliott et al. [43] propose a Bayesian framework using the subtraction of two consecutive scans to estimate the progress of multiple sclerosis (MS). However, MS lesions do not deform normal brain tissues and thus retain the spatial correspondence among the longitudinal scans, which allow the method to use subtraction. In the case of GBM, the tumor grows fast and deformations take place in the tumor locality as well as in the surrounding normal tissues, hence simple subtraction is not effective. Angelini et al. [44] address the nonlinear contrast change between the two follow-up scans with normalization via midway histogram equalization to predict the growth of LG tumors. While the method [44] is effective for slow growing LG tumors, its performance is not justified of more aggressive GBM. A semi-automatic segmentation method is also proposed by Weizman et al. in [45] use the change of gray levels in longitudinal scans that start with the prior information of the first MR scan for LG tumors. However, the method's performance highly relies on the segmentation accuracy of the first scan. Bauer et al. [46] propose a conditional random field(CRF) based method to integrate the four-dimensional (4D) spatio-temporal cliques for longitudinal tumor segmentation. Alberts et al. [47] use a graphical method in a CRF for tumor segmentation. However, parameter learning of CRF methods for higher order cliques in a multi-class scenario is challenging. The temporal variation of tumor can be quantified effectively by some specific hierarchical texture features such as Spin image, rotation invariant feature transform and local binary profile. This study is greatly inspired by [48], in which Karimaghhaloo et al. first use two-dimensional hierarchical feature to reduce the false positives in detecting small gadolinium-enhanced lesions in longitudinal images. In general,

MS lesion enhancement by gadolinium agent slowly diminishes over 6 months period whereas non-lesional tissue enhancement remains same. However, the method is limitedly applicable on the dataset that consists of longitudinal scans with at least six months apart so that the lesion's enhancement at time  $t$  appears non-enhanced at time  $t'$ . This study used brain tumor images that are always scanned with gadolinium agents and differs from MS lesions which have enhancement at time  $t$  and non-enhancement at time  $t'$ . Moreover, GBM grows rapidly, as a result, significant spatial deformations occur in the follow up scans. In order to use the temporal information, it is important to relate the corresponding points or locality in the follow-up images. Therefore, in the cases of large deformations spatial correspondence considerably reduced among the follow-up images for tumor and non-tumor tissues. This study argues that 3D texture analysis is more suitable than 2D texture to capture the temporal variation of the detected pathology. In this study, the proposed method quantifies the temporal variation using specific 3D texture features; spin image, RIFT and LBP to reduce the false positives from segmentation outcomes. Although these features are widely used in computer vision algorithms for different types of object recognition their efficacy is not investigated in medical image analysis.

## 2.3 GLIOMA GRADING

### 2.3.1 NON-INVASIVE GLIOMA GRADING

In the literature, several non-invasive computer aided techniques are proposed. Among recent work, Weber et al. [49] capture the inherent heterogeneity properties of brain neoplasms from spectroscopy and perfusion MR images. In [50], Wang et al. classify malignant and benign brain neoplasm using the spectroscopy and conventional MR images. Zacharaki et al. [51] extract shape and Gabor-like texton [26] features from perfusion and conventional MRIs for tumor grading. However, none of the above methods employ only structural MRI, that is the most routinely available imaging modalities. Devising a texture-based non-invasive structural MRI method for tumor grading is useful. This study proposes a novel non-invasive brain tumor type classification using MF DFA [18], DT [19], mBm in structural MR images. In this study, the efficacy of texture feature in classifying (grading) brain tumors as HG versus LG and GBM versus LG is investigated. As the aggressiveness of different glioma grades differs significantly, the texture in structural MR images may be a useful feature to discriminate them.

### 2.3.2 AUTOMATIC GLIOMA GRADING IN DP IMAGES

In regular a clinical setting, tumor grading is an invasive process that performed by the visual observation in the microscopy tissue slide images. Many automatic cyto-/histological image analysis methods have been reported in the literature for classification of breast cancers, follicular lymphoma, bone marrow, and brain tumors. Among the recent automatic tumor classification works, Kong et al. [22] use a computationally extensive nuclear score(NS) based quantification of

oligodendroglioma component(OC) population to classify GBM subtypes. Barker et al. [20] use local textures in a tile-based framework, which is also computationally extensive and needs a more sophisticated image matching algorithm. Apart from the aforementioned feature-based method, Xu et al. [21] use the deep convolution activation features to classify GBM and LG. However, the method needs an extremely large number of training data for effective feature extraction. This work proposes a computationally efficient feature analysis and classification method using the morphological features of cell nuclei for tumor grading. The proposed classification method simply uses the k-mean clusters centroids of the morphologic features to avoid NS calculation and searching of a suitable candidate tile.

## CHAPTER 3

# MULTI-RESOLUTION TEXTURE FEATURE FOR AUTOMATIC SEGMENTATION OF BRAIN ABNORMAL TISSUES

### 3.1 CHAPTER OVERVIEW

Different techniques mentioned in the previous section clearly indicate that extracting effective feature is one of the key factors for successful segmentation. Fractal-based spatially varying textures can be one of the effective features for the segmentation of abnormal brain tissues in MRI. This chapter discusses multi-fractal texture estimation and characterization of abnormal brain lesions (necrosis, edema, enhanced tumor, non-enhanced tumor etc.) and ischemic stroke lesions in magnetic resonance (MR) images. This work formulates the complex abnormal tumor texture in MR images using a stochastic model known as multi-fractional Brownian motion (mBm). Mathematical derivations of the mBm model and corresponding algorithm to extract the spatially-varying multi-fractal texture feature are discussed. Extracted multi-fractal texture features are fused with other effective features to enhance the tissue characteristics. Segmentation of the tissues is performed by using a feature based classification method. The efficacy of the mBm texture feature in segmenting different abnormal tissues is demonstrated using a large-scale publicly available clinical dataset. Experimental results and performance of the methods confirm the efficacy of the proposed technique in an automatic segmentation of abnormal tissues in multimodal (T1, T2, Flair and T1contrast) brain MRIs.

### 3.2 METHODOLOGY

This section describes the developed pipeline for abnormal brain tissue segmentation from the 3D MRI volume images (T1, T2, T1c and Flair). Figure 3 shows the steps in the pipeline, which is the proposed method in the previous work [7]. The process starts with linear co-registration among the modalities, which reduces the alignment, rotation, and scaling mismatches. Then 2D MRI slices are obtained from the 3D volume for subsequent processing. A brief discussion on each of the steps in Figure 3, is given below.



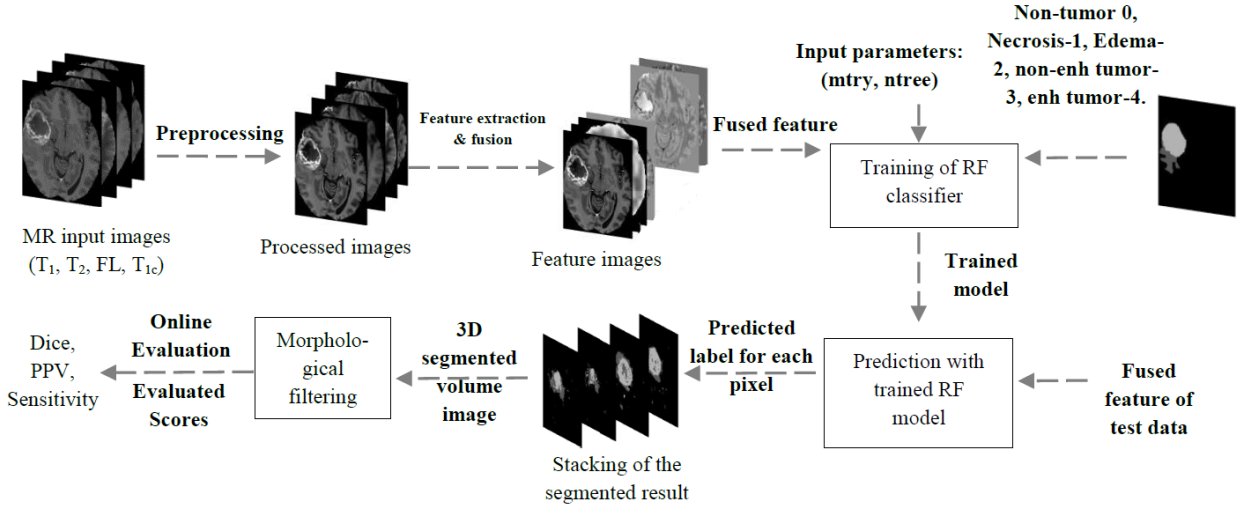


**Figure 3:** Multi-tissue brain abnormal tissue segmentation pipeline [7].

### 3.2.1 PRE-PROCESSING

The preprocessing step involves aligning and co-registration among the channels, resampling, skull stripping, a MR bias field, and intensity inhomogeneity correction. Co-registration is performed to correct the miss-alignment among the modalities and can be done with several tools such as SPM, ITK, and Slicer3D. A MR bias field signal is a low-frequency and very smooth signal that blurs an image and reduces the high-frequency components from the images. Therefore, it is very important to reduce the MR bias field and thus several techniques are found in the literature. This work performs MRI bias correction with a N4ITK [52] MRI bias correction tool of slicer3D. In order to minimize the intensity inhomogeneity of the MR image, intensity normalization is performed. The intensity normalization for MR images is very important because the intensity of the same tissue type can vary from patient to patient and even slice to slice of the same patient. Several MR intensity inhomogeneity correction techniques [53][54] are available in the literature. The intensity inhomogeneity correction method in [53] is a two-step normalization method, where the image histograms are modified such that the histograms match a mean histogram obtained using the training data. After inhomogeneity correction, the intensity values for the same tissue in different MR images fall into a single range of the scale. The method in [54] also comprises two steps. In the first step, 10 point histogram matching is performed, where the reference images of four modalities are arbitrary set from a single patient data. Intensity values below the mean of the input volume are considered as the background pixel and excluded from the histogram matching process. The next step is normalizing all the intensity values around the mean intensity value of cerebrospinal fluid (CSF). In [54], two class classification (CSF vs. Rest) is performed using the random forest to separate the CSF from the other tissues. It is noticed that simply threshold the intensity differences among the modalities gives a fair output to get the CSF mask. The method takes the histogram matched images, inhomogeneity corrected images, and this CSF mask as the features. Figure 4

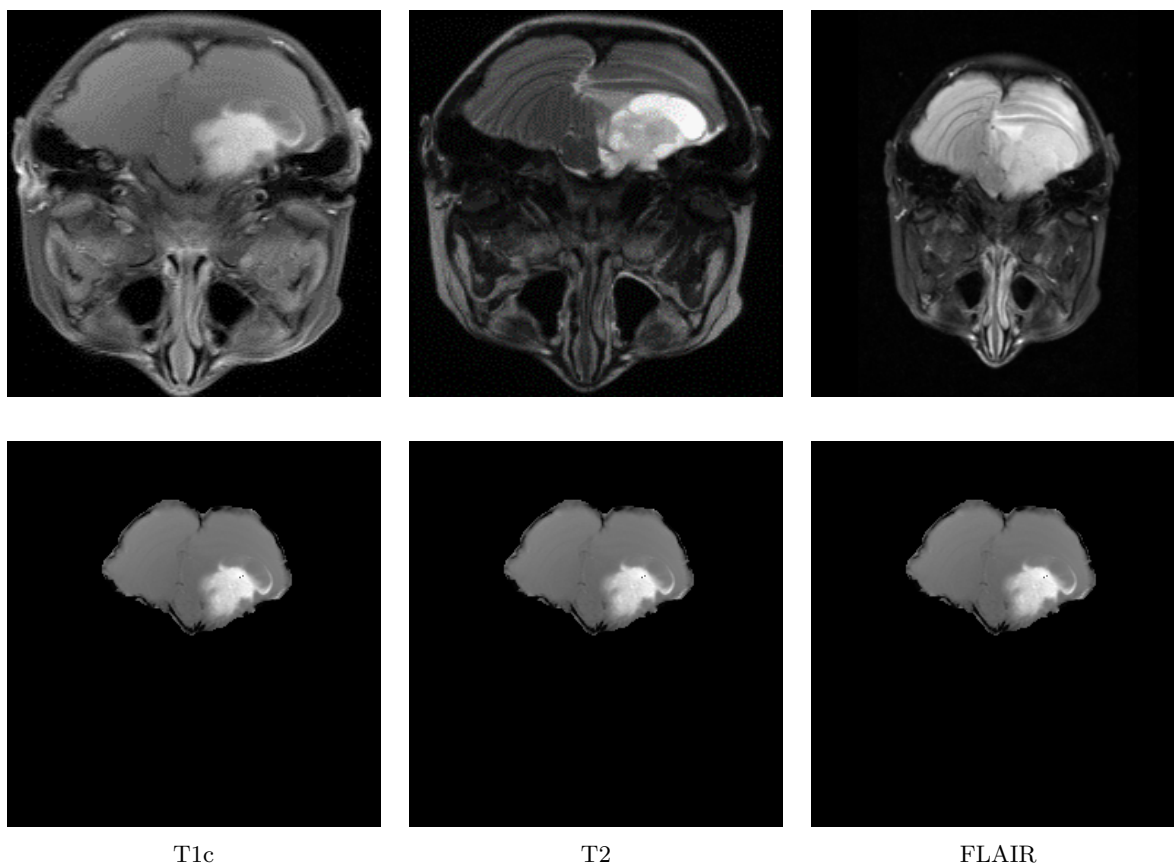


**Figure 4:** Example images of standard MRI preprocessing. This involves aligning and co-registration among the channels, resampling, skull stripping, MR bias field and intensity inhomogeneity correction. Figure shows the original images (top row) and preprocessed images (bottom row). After preprocessing the images are skull-stripped, aligned to the intra-modalities, and channel-wise intensities are normalized.

shows example images of original and preprocessed images.

### 3.2.2 FEATURE EXTRACTION, FUSION, RANKING AND SELECTION

For each slice of the input images, the method extracts two primary sets of features such as non-local and spatial/texture.

#### 3.2.2.1 FEATURE TYPE-1 (NON-LOCAL FEATURE)

The non-local features are the pixel intensities of four MRI modalities and corresponding differences of pixel intensities among the modalities. These features do not depend on the local texture patterns and thus are named as non-local features. The proposed method uses the

intensities ( $I_{T_1}, I_{T_2}, I_{Fl}, I_{T_{1c}}$ ) and the intensity differences ( $d_1 = I_{T_1} - I_{T_2}, d_2 = I_{T_2} - I_{Fl}, d_3 = I_{Fl} - I_{T_{1c}}$ ) to capture the global characteristics of different tissues. This difference features ( $d_1, d_2, d_3$ ) describe the amount of intensity variation at each pixel among the MR modalities. It is instinctive that different tissues (WM, GM, CSF, Tumor-core, Necrosis, and Edema) may display a different amount of intensity variation among the modalities. A similar type of difference features is also used in [27].

### 3.2.2.2 FEATURE TYPE-2 (SPATIAL/TEXTURE FEATURE)

The spatial or texture features are those features that depend on the local texture pattern of an area. As the tumor is the uncontrolled growth of the tissues, it infiltrates into the surroundings and takes a different texture pattern which is expected to be different from the non-tumor region. In order to characterize the tumor surface variation, the method employs novel fractal texture features such as fractal PTPSA, mBm. It also uses regular Gabor-like texton since these features have an important association for image segmentation. The texton features are useful to decompose an image into its constituent components and reduce the redundant information. In general, total 48 filters including 3-scales, 6-orientations, 2-phases, 8 Laplacian of Gaussian (LOG), and 4 Gaussian filters are used in the texton feature extraction process. Instead of using all 48 texton filter outputs, manually few filters are selected which show visually significant differences among the abnormal and normal tissue regions. The extensions of tumor segmentation for ischemic stroke lesion lie in replacing  $T_{1c}$  with new MR modality DWI and adding new feature, structure tensor based local gradient information from all four modalities ( $T_1, T_2, Flair$  and DWI). As in tumor segmentation, the rest of the features and procedure remain the same. While more details on fractal texture features can be found in [11] and [55], this section briefly describes the PTPSA, mBm and structure tensor based local gradient feature extraction process.

#### FRACTAL (PTPSA) TEXTURE FEATURE EXTRACTION

Fractal is an irregular geometric object with infinite nesting of a self-similar structure at multiple scales. The concept of the fractal is first proposed by Mandelbrot [56] to describe the geometry of the natural objects. The fractal dimension (FD) feature is a non-integer real number that characterizes the texture of objects. In a prior work [11], statistically the effectiveness of PTPSA feature is investigated for brain tumor detection. In PTPSA, the image is divided into several equal sub-images. For each sub-image as shown in Figure 5, the intensities of the four corners ( $I_1, I_2, I_3, I_4$ ) and their average ( $I_c$ ) at the center pixel form four triangles ( $ABE, ADE, BCE, DCE$ ). The FD is calculated by the slope of the log-log plot of the total surface areas of the four triangles vs. sub-image size.

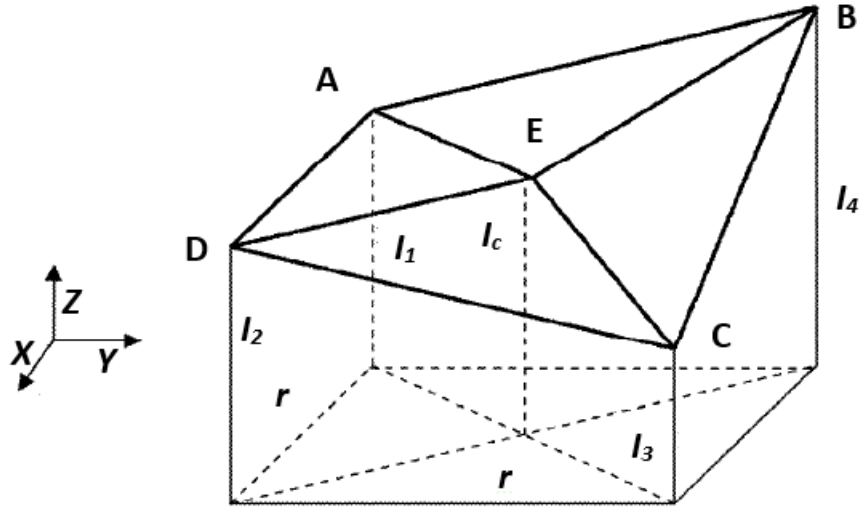


**Figure 5:** Illustration of fractal PTPSA feature extraction for a sub-image [12].

### MULTI-RESOLUTION TEXTURE FEATURE

The mBm is a non-stationary zero-mean Gaussian random process that corresponds to the generalization of fractional Brownian motion (fBm). The fBm is a part of the set  $(1/f)$  process and is considered to be homogeneous or mono-fractal. The Hurst index (Holder exponent),  $H$  in fBm process is same at all-time instances. The value of  $H(0 < H < 1)$  determines the randomness of the fBm process. For example, if  $H = 0.01$  the signal is very smooth, while for  $H = 0.99$ , the signal is very rough. Figure 6 shows an example of a simulated 1-D fBm process vs. time plots for different  $H$  values.

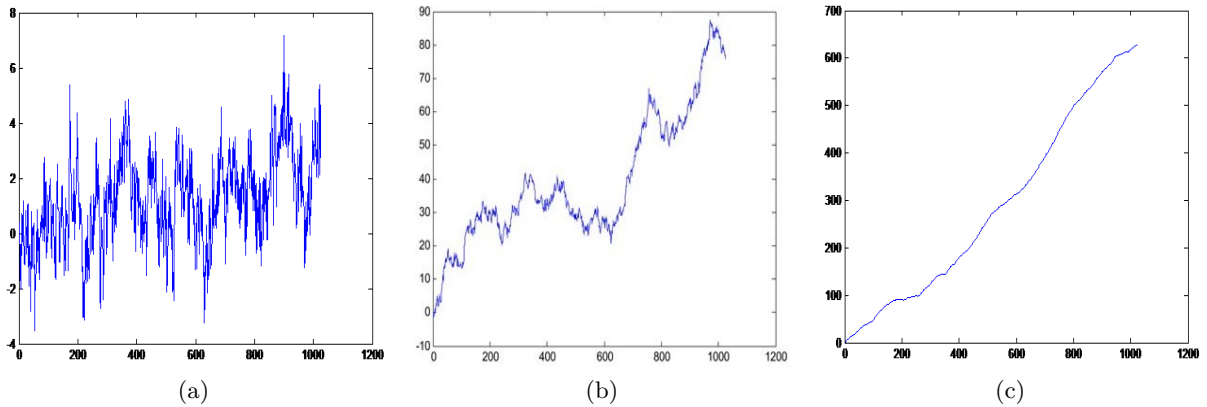


**Figure 6:** Simulation of  $fBm$  process using different *Hurst*,  $H$  index, which determines the variation of signal roughness. (a)  $H = 0.01$ , (b)  $H = 0.50$ , and (c)  $H = 0.99$ .

Figure 6 confirms variation of signal roughness with the variation of values. However, like many other natural signals the roughness of the tumor texture varies in space, therefore tumor texture is more amenable to the multi-fractal structure. Consequently, this work attempts to estimate tumor texture using the *mBm* process. In *mBm* process the Hurst index,  $H$  is a time varying parameter, which effectively captures the spatially varying heterogeneous texture of brain tissues. The *mBm* process is defined as,  $x(at) = a^{H(t)}H(t)$ , where  $x(t)$  is the *mBm* process with the scaling factor,  $a$  and the time varying Hurst index,  $H(t)$ . The covariance function of a 2-D *mBm* process is given as

$$E(z(\vec{u})z(\vec{v})) = \frac{\sigma_{\vec{u}}^2}{2} [|\vec{u}|^{2H(\vec{u})} + |\vec{v}|^{2H(\vec{v})} - |\vec{u} - \vec{v}|^{2H(\vec{u})}]; \quad (1)$$

where,  $z(\vec{u})$  is the *mBm* process,  $\vec{u}$  denotes the vector position  $(u_x, u_y)$  of a point in the process,  $\sigma_{\vec{u}}^2$  is the variance and  $H(\vec{u})$  is the Hurst index for a 2-D signal. After a series of mathematical derivations, the expectation of the squared magnitude of wavelet coefficients  $E\{|W_z(\vec{b}, a)|^2\}$  is given by

$$E\{|W_z(\vec{b}, a)|^2\} = \frac{1}{M+N} \sum_{x=0}^{N-1} \sum_{y=0}^{M-1} |W_z(\vec{b}, a)|^2, \quad (2)$$

Here,  $a$  is the scaling factor and  $\vec{b}$  is the 2-D translation vector of the wavelet basis. Also,  $N$  and  $M$  are the dimensions of the image. The Hurst index for 2-D image is calculated as follows

$$2H(\vec{u}) = \lim_{a \rightarrow 0^+} \frac{\log\left(\frac{1}{M+N} \sum_{x=0}^{N-1} \sum_{y=0}^{M-1} |W_z(\vec{b}, a)|^2\right)}{\log a}. \quad (3)$$

Finally, the fractal dimension (FD) is obtained as

$$FD = E + 1 - H(u), \quad (4)$$

where,  $E$  is the Euclidean dimension ( $E = 2$  for 2-D images). For a given image, the method first divides the image into non-overlapping blocks or sub-images and calculate the FD for that corresponding sub-image. The process is repeated for all the sub-images. The simplified algorithm for *mBm* texture feature extraction is shown in Figure 7. The detail mathematical derivations of *mBm* and the description of the above algorithm shown in Figure 7 for *mBm* texture feature can be found in [5].

---

```

Input: image, wavelet, level
// image : N × M MRI image
Output: MultiFD
a. for a in 1 to level do
  | i. compute the wavelet coefficients at scale a as shown in (2)
  | ii. compute  $E\{|W_z(\vec{b}, a)|^2\}$ 
end
b. Compute  $H(\vec{u})$  using  $\log(E\{|W_z(\vec{b}, a)|^2\})$ 
  versus  $\log(a)$  as shown in (3)
c. Compute  $FD = 2 + 1 - H(\vec{u})$ 
return FD

```

---

**Figure 7:** Algorithm for tissue texture extraction using the mBm process.

**STRUCTURE TENSOR BASED LOCAL GRADIENT FEATURE** Eigen value decomposition of the 2D structure tensor matrix [57] is performed to capture the local gradient information. From all four modalities, Eigen values ( $\lambda_1, \lambda_2$ ) are used as new features which allow a more precise description of the local gradient characteristics.

### 3.2.3 FEATURE FUSION

After feature extraction from each corresponding slices, the method performs a feature domain fusion. Each row of resulting in a fused feature matrix represents all the feature values for a corresponding pixel location of the brain. To illustrate this fusion, let us consider each of the input image volumes is of size  $V(= X \times Y \times Z)$ , where  $X, Y, Z$  indicates the number of row, column, and slices of an input image respectively. For  $N_f$  number of features extracted, the 3D-fused feature matrix will be of size  $(N_r \times N_f \times Z)$ , where  $N_r(= X \times Y)$  is the number of rows in the feature matrix,  $N_f$  is the number of columns, and  $Z$  is the number of slices as usual.

### 3.2.4 FEATURE RANKING AND SELECTION

All the features are not equally important and redundancy among the features degrades the classifier's performance. To identify the most useful features from the whole feature set, different feature ranking and selection methods are used. From the recent techniques, the method uses a mutual information based implementation of minimum redundancy maximum relevance (mRMR) [58] feature ranking technique. The method works in two steps. In the first step, it uses mutual information to search the maximum relevance between the individual feature and the class label. However, the features selected with the maximum relevance could have high redundancy among them, and it is intuitive that combination of these redundant features

may have poor class-discriminating power. Therefore, in the second step, the method uses the minimal redundancy to select the mutually exclusive features. In this work, the method performs the feature ranking on the whole feature set and then heuristically select 19 top ranked features out of 38 features. Among all the features, it is noticed that the intensity, intensity differences, and the mBm features are in the top ranking list. This confirms the effectiveness of novel texture features (mBm and PTPSA) in segmenting posterior-fossa brain tumor in the previous works [5][12].

### 3.2.5 CLASSIFICATION WITH RANDOM FOREST

Because of fast and efficient multiclass handling capability, RF [13] is used for the tissue classification. In the prediction level as shown in Figure 3, the RF classifier assigns a label for each point of the test data. The method assigns the predicted labels (0, 1, 2, 3, 4) to represent different tissues as non-tumor, necrosis, edema, non-enhanced, and enhanced tumor respectively in the final segmented image. The RF [13] is an ensemble learning algorithm that generates many classification trees. Each tree offers a classification that is known as votes for that class. The forest chooses the classification having the most votes over all trees in the forest. The additional layer of randomness to bagging and the randomly selected subset of predictors [59] helps RF to perform better classification compared to other classifiers such as support vector machines and neural networks. The classical random forests algorithm for both classification and regression can be described as follows [59].

- Draw  $N_{tree}$  bootstrap samples from training dataset.  $N_{tree}$  is the number of trees necessary for good predictions suggested by a subset of data samples. The best way to select  $N_{tree}$  is the overall performance comparison for different settings.
- For each bootstrap data sample, grow a classification tree where at each node, randomly sample  $m_{try}$  predictors and choose the best split from the chosen predictors.
- Predict new data using the collective predictions of  $N_{tree}$  number of classification trees.

In this case, the method gradually increases  $N_{tree}$  and  $m_{try}$  each at a time and observed the overall classification performance. After extensive investigation,  $N_{tree} = 150$  and  $m_{try} = 4$  are set for this work. RF for classification is also known as Classification Forests (CFs). The Classification Forests are ensembles of binary classification trees [7]. At each node,  $n$  classification tree randomly takes a subset of training samples,  $X_n$  and predicts a class  $P_t^n(\Omega_i|x)$ , where  $P_t$  is the probability of the sample  $x$  in class  $\Omega_i$  [7]. There are five classes;  $\Omega = \{\Omega_0, \Omega_1, \Omega_2, \Omega_3, \text{and } \Omega_4\}$  as non-tumor, necrosis, edema, non-enhanced, and enhanced tumor. Depending on the feature dimension, CF continually chooses a random dimension to split the training samples at every node and assigns the partitions  $X_L$  and  $X_R$  to the left/right nodes. Tree growing continues up to a certain tree depth,  $D_T$ . In the testing phase, data points to be classified are pushed through each tree  $t$ , with the learned split functions. The leaf node probability is directly used as the

tree probability i.e.

$$p_t(\Omega_i|x) = p_t^l(\Omega_i|x) \quad (5)$$

where,  $p_t^l$  denotes the probability of sample  $x$  at leaf node  $l$  in class  $\Omega_i$ .

The overall probability is calculated by the following equation,

$$p(\Omega_i|x) = \frac{1}{T} \sum_{t=1}^T p_t(\Omega_i|x) \quad (6)$$

where,  $p(\Omega_i|x)$  is the average probability of sample  $x$  in class  $\Omega_i$  and  $T$  is the total number of trees. Finally, the class with the highest probability is estimated  $\hat{\Omega}_i$  as the actual class

$$\hat{\Omega}_i = \underset{\Omega_i}{\operatorname{argmax}} p(\Omega_i|x) \quad (7)$$

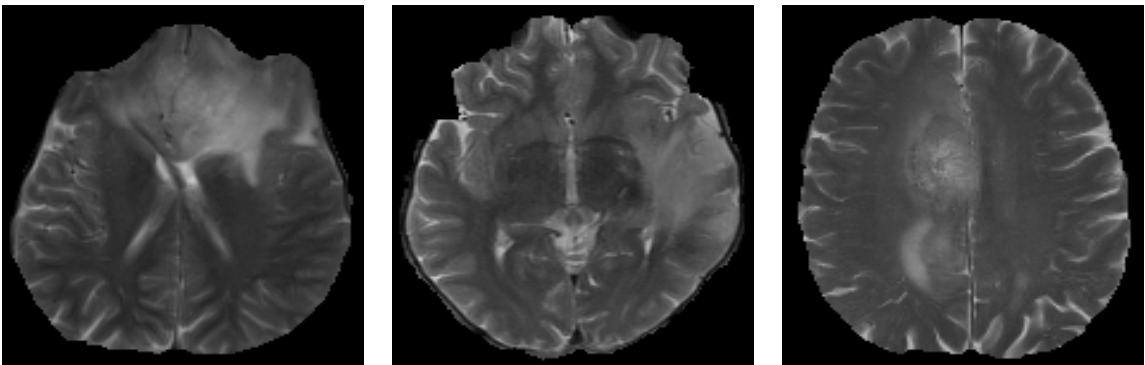
More details about CF can be found in [60].

### 3.3 RESULTS

This section reports the segmentation results obtained from the predicted pixel labels of the RF classifier. These 2D abnormal tissue segments are then stacked to generate volume image.

#### 3.3.1 MULTI-CLASS TUMOR TISSUE SEGMENTATION

Figure 8 and 9 show example tissue segments using three slices taken from randomly chosen patients of training and test cases respectively.





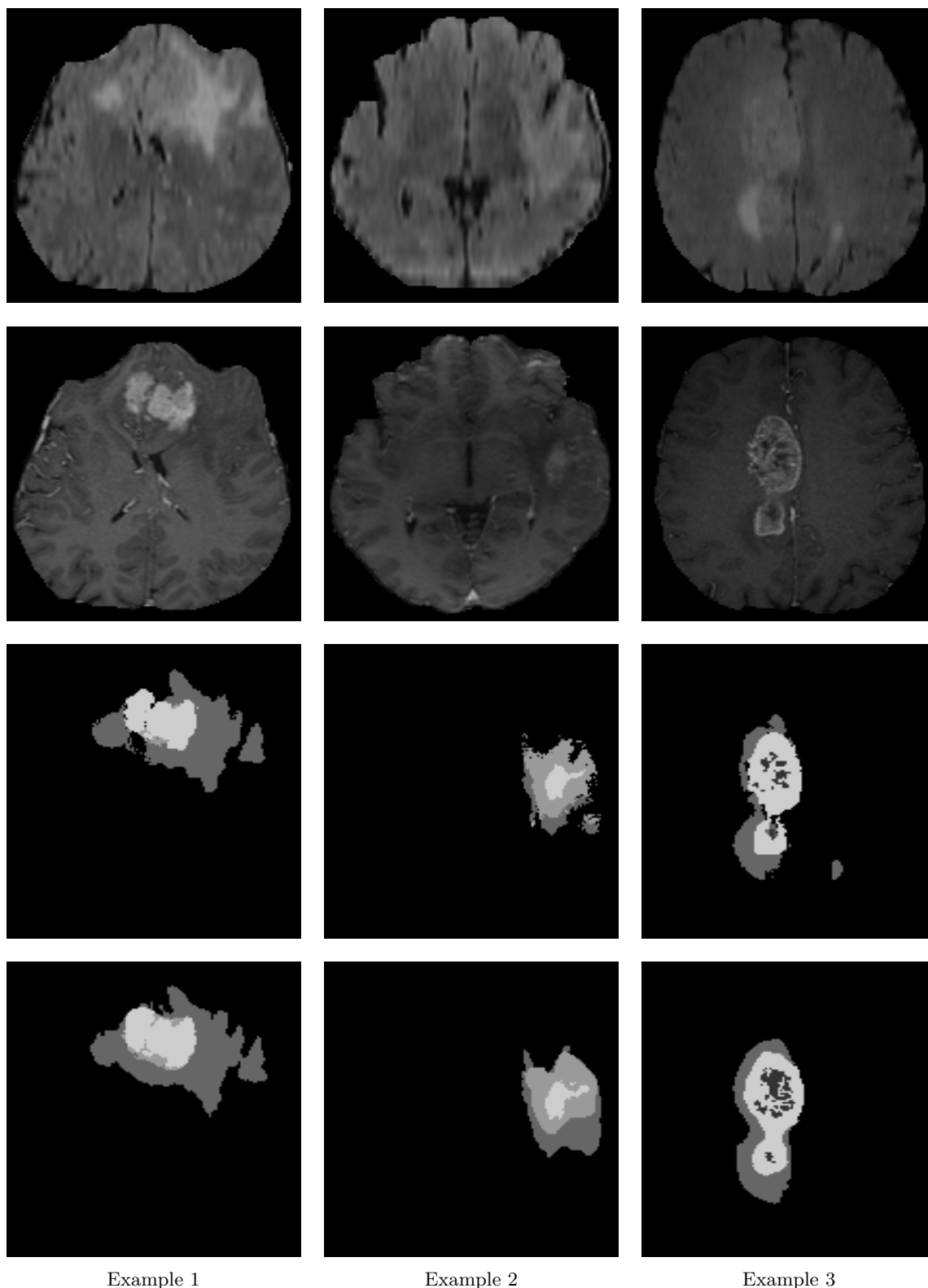
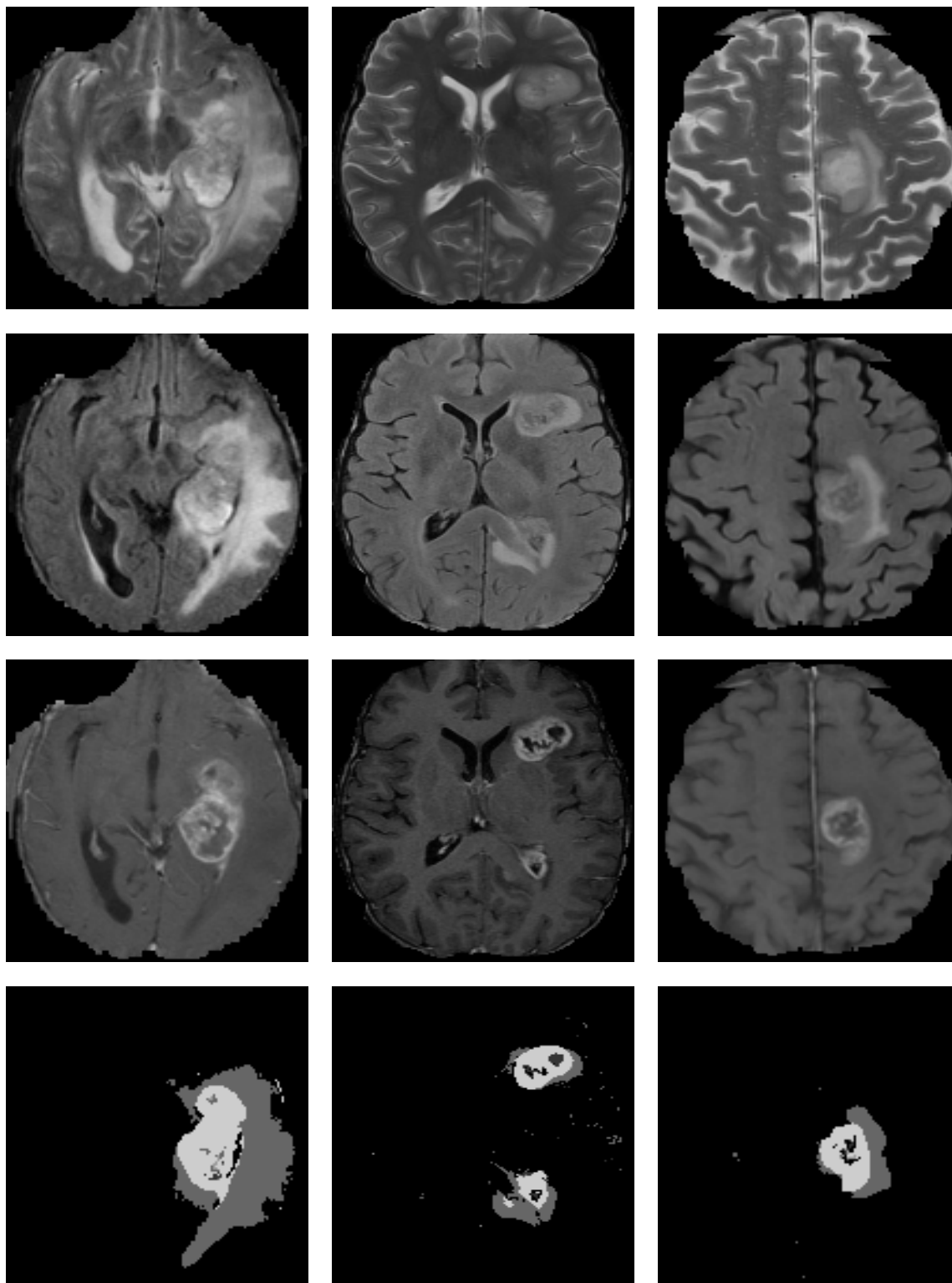


**Figure 8:** Example images of multi-tissue (Edema, Necrosis, Enhanced and non-Enhanced active tumor) segmentation in training dataset. Each column represents an example set of multimodality MRI slices. Row (1-5) T2, Flair, T1c segmented image and ground-truth. Labels in the ground-truth: 1-necrosis, 2-edema, 3-non-enhancing tumor, 4-enhancing tumor, 0-everything else. (Note: Although all four modalities; T1, T2, Flair, T1c, are used by the method for the sake of clear view T1 modality is dropped in the figure).



Example 1

Example 2

Example 3

**Figure 9:** Example images of multi-tissue (Edema, Necrosis, Enhanced and non-Enhanced active tumor) segmentation in test dataset. Each column represents an example set of multimodality MRI slices. Row (1-4) T2, Flair, T1contrast, and segmented image.

### 3.3.1.1 EVALUATION

The following similarity coefficients are exploited to evaluate any of our segmentation performance.

$$1. \text{ Dice} = \frac{2TP}{2TP + (FP + FN)}$$

$$2. \text{ Sensitivity} = \frac{TP}{TP + FN}$$

where TP= True positive, FP=False positive and FN= False negative. Three different categories such as the complete tumor, tumor core, and other tissues are considered for the evaluation. The details on these three categories are as follows: Complete Tumor: (1-necrosis, 2-Edema, 3-non-enhancing tumor, 4-enhance tumor); Tumor Core: (3-non-enhance tumor, 4-enhance tumor); and other tissues.

### 3.3.1.2 QUANTITATIVE EVALUATION

In this work, the preliminary abnormal tissue segmentation results are evaluated using the BRATS-2013 [61] and BRATS-2014 [62] clinical dataset. BRATS-2013 dataset consists of multi-contrast MR scans from 65 glioma patients with LG (astrocytoma or oligoastrocytomas) and HG (anaplastic astrocytoma and glioblastoma multiforme) tumors. Similarly, BRATS-2014 dataset consists of MR images of around 350 patients. The method performs a 3-fold within patient cross-validation on 213 training patients of the BRATS-2014 dataset, the average scores using the proposed method are shown in Table 3. The segmentation rate using 3-fold cross-validation varies 73% to 87% using Dice overlap metric for tumor core and complete tumor respectively. Low standard deviation, 8% - 24% indicates that the proposed method offers consistent results for different abnormal tissue segmentation.

**Table 3:** Average quantitative scores (Dice, Sensitivity) of multi-class tumor tissue segmentation (3-fold) in training dataset. Results of 213 patients (BRATS-2014) using the proposed method [63].

	Dice						Sensitivity					
	<i>Necrosis</i>	<i>Edema</i>	<i>non-Enh</i>	<i>Enh</i>	<i>Core</i>	<i>Complete</i>	<i>Necrosis</i>	<i>Edema</i>	<i>non-Enh</i>	<i>Enh</i>	<i>Core</i>	<i>Complete</i>
Mean	0.42	0.76	0.13	0.74	0.73	0.87	0.72	0.80	0.09	0.84	0.72	0.89
Std.	0.30	0.13	0.13	0.23	0.24	0.08	0.34	0.15	0.11	0.21	0.26	0.09

The patient-wise cross-validation results using the proposed algorithm in Table 3 suggest that one

may obtain reasonably good results for any representative patient dataset. In order to measure the robustness of the method, the trained RF classifier with BRATS-2013 data is applied on the BRATS-2014 dataset. Quantitative scores of 213 training patients of BRATS-2014 with the proposed method (Figure 3) are shown in Table 4.

**Table 4:** Average quantitative scores (Dice, Sensitivity) of multi-class tumor tissue segmentation using 213 patients as test dataset. RF classifier is trained with 20 HG patients of BRATS-2013 [63] and tested on 213 patients of BRATS-2014 dataset.

	Dice						Sensitivity					
	<i>Necrosis</i>	<i>Edema</i>	<i>non-Enh</i>	<i>Enh</i>	<i>Core</i>	<i>Complete</i>	<i>Necrosis</i>	<i>Edema</i>	<i>non-Enh</i>	<i>Enh</i>	<i>Core</i>	<i>Complete</i>
Mean	0.31	0.62	0.03	0.63	0.63	0.76	0.49	0.59	0.02	0.85	0.62	0.71
Std.	0.27	0.17	0.05	0.28	0.22	0.15	0.31	0.18	0.03	0.18	0.23	0.18

Results in Table 4 shows that the *Dice* score varies from 63% to 76% using the proposed method, which is very promising.

### 3.3.1.3 STATE-OF-THE-ART COMPARISON

Having participated in multiple global tissue segmentation challenge, the method ranked 3<sup>rd</sup> out of 7 in BRATS-2013 (in Japan) [61], 4<sup>th</sup> out of 15 in BRATS 2014 (in Boston) [62] organized by NCI and MICCAI. Table 5 shows the final ranking of the participants in the BRATS-2013 challenge.

Patient														
Position	User	Dice			Positive Predictive Value			Sensitivity			Kappa	Complete tumor Rank	Tumor core Rank	Enhancing tumor Rank
		complete	core	enhancing	complete	core	enhancing	complete	core	enhancing				
1	Nick Tustison	0.87 (1)	0.78 (1)	0.74 (1)	0.85 (2)	0.74 (4)	0.69 (4)	0.89 (2)	0.88 (1)	0.83 (1)	0.99 (1)	1.67	2.00	1.89
2	Raphael Meier	0.82 (5)	0.73 (2)	0.69 (3)	0.76 (6)	0.78 (2)	0.71 (1)	0.92 (1)	0.72 (4)	0.73 (3)	0.99 (4)	4.00	2.67	3.00
3	Syed Reza	0.83 (4)	0.72 (3)	0.72 (2)	0.82 (3)	0.81 (1)	0.70 (3)	0.86 (5)	0.69 (6)	0.76 (2)	0.99 (3)	4.00	3.33	3.22
4	Liang Zhao	0.84 (3)	0.70 (4)	0.65 (5)	0.80 (4)	0.67 (5)	0.65 (6)	0.89 (3)	0.79 (3)	0.70 (4)	0.99 (5)	3.33	4.00	4.11
5	Nicolas Cordier	0.84 (2)	0.68 (5)	0.65 (6)	0.88 (1)	0.63 (6)	0.68 (5)	0.81 (6)	0.82 (2)	0.66 (6)	0.99 (2)	3.00	4.33	4.33
6	Joana Festa	0.72 (6)	0.66 (6)	0.67 (4)	0.77 (5)	0.77 (3)	0.70 (2)	0.72 (7)	0.60 (7)	0.70 (5)	0.98 (6)	6.00	5.33	5.00
7	Senan Doyle	0.71 (7)	0.46 (7)	0.52 (7)	0.66 (7)	0.38 (7)	0.58 (7)	0.87 (4)	0.70 (5)	0.55 (7)	0.98 (7)	6.00	6.33	6.44

**Table 5:** Final ranking of multimodal brain tumor segmentation (BRATS) 2013. The proposed method ranked 3<sup>rd</sup> in BRATS-2013 (Japan) on the final challenge [61].

### 3.3.1.4 DISCUSSION ON TUMOR SEGMENTATION RESULT

In summary, the results in Tables 3, 4, and 5 show that the proposed method is effective in segmenting different tissues of glioma tumors. From the tissue-wise results, it is noticed that the texture-based method performs comparatively better for larger lesion size while for smaller lesions the performance is compromised. It is also realized that the interpolation method in the texture feature extraction process penalizes the detail of the smaller lesions and thus the classification performance is less than satisfactory. Again from the patient-wise results, it is noticed that the proposed algorithm usually performs better for High grade (HG) tumors than Low grade (LG). Therefore, the observation suggests that the MRI containing HG tumor surface may contain higher randomness in texture.

## 3.4 ISCHEMIC STROKE LESION SEGMENTATION

This section describes the extended study of BTS for lesion segmentation.

### 3.4.1 MODIFIED BTS FOR LESION SEGMENTATION

The overall flow diagram of the proposed approach is shown in Figure 10.

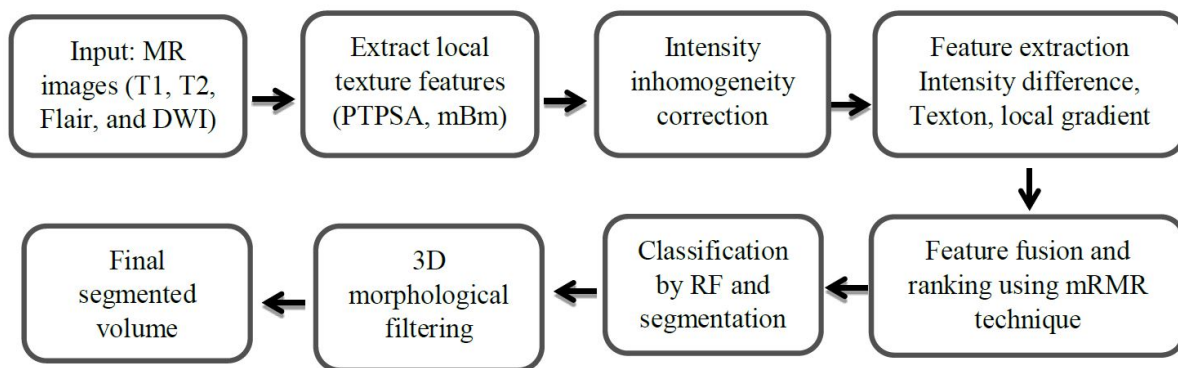


**Figure 10:** Generalized flow diagram for ischemic stroke lesion segmentation. An extension of the multi-tissue tumor tissue segmentation method [64].

The detail description of the above method is similar to the previous BTS method.

#### 3.4.1.1 THE LESION DATA

The method is evaluated on the images of 28 patients having sub-acute ischemic stroke lesions collected from the training dataset of ISLES2015 challenge [3]. The detail of this work can also be found in [64].

#### 3.4.1.2 RESULTS OF LESION SEGMENTATION

The 2D segmented tissues are obtained using the predicted pixel labels from RF. These 2D segments are then stacked to generate volume image. Example images of lesion segmentation of two random patients are shown in Figure 11 [64].

#### 3.4.1.3 QUANTITATIVE EVALUATION

The preliminary lesion segmentation results are evaluated using of the ISLES-2015 SISS training dataset having images of 28 patients. The efficiency of the method is investigated by cross-patient cross-validation, where odd patients are used in training to test the even patients and vice versa. On an average, the 59 % Dice score overlaps with 23% standard deviation are obtained from the cross-patient cross-validation. Moreover, comparatively higher scores are noticed for lesions with bigger size than the smaller ones. A summary of the quantitative scores are presented in Table 6 [64].

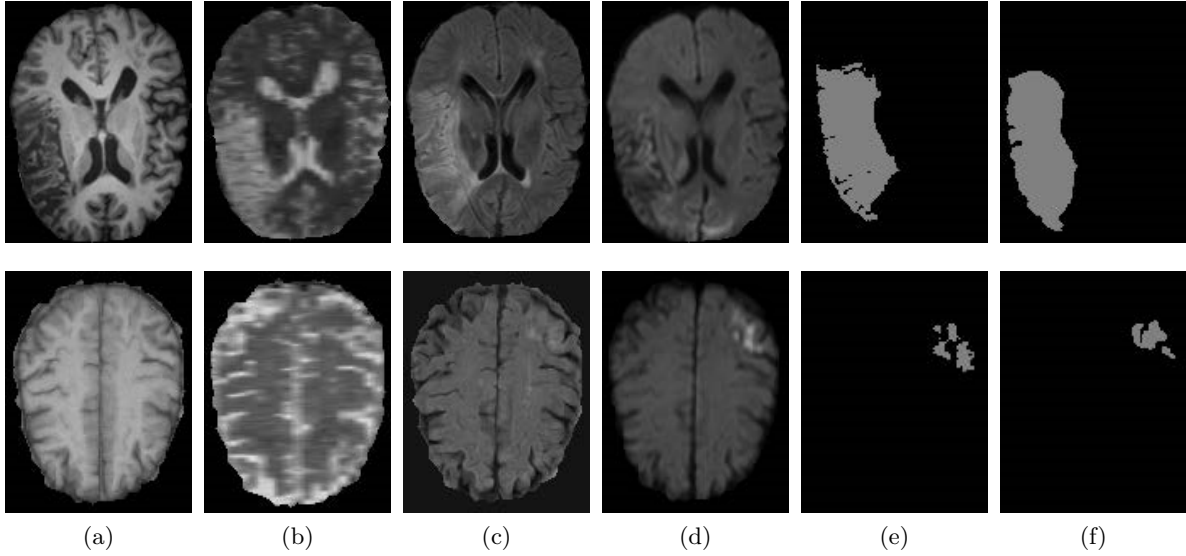


**Figure 11:** Example images of segmented lesions for two random patients. Each row represents an example set of multimodality MRI slices. Input: (a) T1, (b) T2, (c) Flair (d) DWI. (e) Segmented lesion (f) ground-truth. Labels in the ground-truth: 1-lesion, 0-background.

**Table 6:** Patient-wise quantitative (Dice) scores of ischemic stroke (sub-acute) lesion segmentation results. The scores are obtained using 28 patients data. The RF classifier is trained with the odd numbered cases to test the even numbered cases and vice versa.

Pat 01	Pat 02	Pat 03	Pat 04	Pat 05	Pat 06	Pat 07	Pat 08	Pat 09	Pat 10	Pat 11	Pat 12	Pat 13	Pat 14	Average 0.59, Std. 0.23
0.89	0.75	0.35	0.75	0.81	0.89	0.81	0.77	0.83	0.53	0.60	0.65	0.13	0.80	
Pat 15	Pat 16	Pat 17	Pat 18	Pat 19	Pat 20	Pat 21	Pat 22	Pat 23	Pat 24	Pat 25	Pat 26	Pat 27	Pat 28	
0.74	0.47	0.51	0.55	0.26	0.73	0.08	0.55	0.56	0.56	0.62	0.27	0.26	0.79	















#### 3.4.1.4 STATE-OF-THE-ART COMPARISON

The method ranked 4<sup>th</sup> out of 14 in Ischemic Stroke Lesion (ISLES-2015) challenge [3] organized by NCI/MICCAI in Germany. The results of the challenge are shown in Table 7. The results in Tables 6 and 7 show that the proposed method is effective in segmenting sub-acute ischemic stroke lesions. However, the overall performance of the reported method are far from the manual outline and need further improvement.

### 3.4.1.5 DISCUSSION ON LESION SEGMENTATION

In this work, an automatic lesion segmentation method is proposed and investigated the efficacy of texture-based segmentation technique. Experimental results with clinical patient data confirm the efficacy of the method for sub-acute ischemic stroke lesion segmentation. The training results show comparable performance when compared to other state-of-the-art works posted on the VSD website [65]. However, a lot of false positives are noticed in the detections that compromise the overall results. More investigation for the smaller sized lesions is required. Also presence of holes in the segmented lesion area are noticed. The method reduces most of the holes by a morphological filtering. Future study can be conducted with more effective features and sophisticated feature selection technique. It is also in future plan to deploy convolution neural network (CNN) based segmentation technique to develop a generalized method for both sub-acute and acute ischemic lesion segmentation.

**Table 7:** Ranking of ISLES-2015 Sub-acute stroke lesion segmentation challenge. The method ranked 4th out of 14 participants [3].

SISS						
rank <sup>2</sup> <sup>▲</sup>	first author (VSD-name) & affiliation	cases	ASSD <sup>1</sup>	DC	HD <sup>1</sup>	
3.25	Konstantinos Kamnitsas (kamnk1) Biomedical Image Analysis Group, Imperial College London	34/36	5.96±9.38	0.59±0.31	37.88±30.06	
3.82	Chaolu Feng (fengc1) College of Inform. Science and Eng., Northeastern University, Shenyang	32/36	3.27±3.62	0.55±0.30	19.78±15.65	
5.63	Hanna Halme (halmh1) HUS Medical Imaging Center, University of Helsinki and Helsinki University Hospital	31/36	8.05±9.57	0.47±0.32	40.23±33.17	
6.40	Syed Reza (rezas1) Vision Lab, Old Dominion University, Norfolk	33/36	6.24±5.21	0.43±0.27	41.76±25.11	
6.67	David Robben (robbd1) ESAT/PSI, Dept. of Electrical Engineering, KU Leuven	33/36	11.27±10.17	0.43±0.30	60.79±31.14	
6.70	Oskar Maier (maieo1) Institute of Medical Informatics, Universität zu Lübeck	31/36	10.21±9.44	0.42±0.33	49.17±29.6	
7.07	John Muschelli (muscj1) Johns Hopkins Bloomberg School of Public Health	33/36	11.54±11.14	0.42±0.32	62.43±28.64	
7.54	Liang Chen (chenl2) Biomedical Image Analysis Group, Imperial College London	34/36	11.71±10.12	0.44±0.30	70.61±24.59	
7.66	Francis Dutil (dutil1) Université de Sherbrooke, Sherbrooke	27/36	9.25±9.79	0.35±0.32	44.91±32.53	
7.92	Tom Haeck (haect1) ESAT/PSI, Dept. of Electrical Engineering, KU Leuven	30/36	12.24±13.49	0.37±0.33	58.65±29.99	
7.97	Andrew Jesson (jessa3) Centre for Intelligent Machines, McGill University	31/36	11.04±13.68	0.32±0.26	40.42±26.98	
9.18	Mahmood Qaiser (mahmq2) Signals and Systems, Chalmers University of Technology, Gothenburg	30/36	10.00±6.61	0.38±0.28	72.16±17.32	
9.21	Michael Goetz (goetm2) Junior Group Med. Img. Comp., German Cancer Research Center (DKFZ), Heidelberg	35/36	14.20±10.41	0.33±0.28	77.95±22.13	
10.99	Ching-Wei Wang (wangc2) Grad. Inst. of Biomed. Eng., National Taiwan University of Science and Technology	15/36	7.59±6.24	0.16±0.26	38.54±20.36	



# CHAPTER 4

## LONGITUDINAL BRAIN TUMOR VOLUME SEGMENTATION AND TRACKING USING 3D TEMPORAL HIERARCHICAL TEXTURE FEATURES IN MRI

### 4.1 CHAPTER OVERVIEW

Automatic segmentation and longitudinal tracking of brain tumors in MRI is an active research area. Even though state-of-the-art tumor segmentation methods often show high sensitivity, their performances are compromised due to the substantial presence of FP. Due to uncontrolled growth and infiltration into the surrounding tissues, the tumor regions usually show significant texture variation in longitudinal imaging while the texture of non-tumor regions remains fairly same. Analyzing this temporal behavior using specific 3D texture features such as spin image, RIFT and LBP may be useful to discriminate the tumor volumes from non-tumors. This study develops an effective post-processing method by employing a combination of 3D temporal texture features to reduce the false positives and thus improve the original segmentation. The proposed method is evaluated using 96 longitudinal MRI scans from 19 patients in a multi-center dataset. On an average 62% of FP are reduced and the average dice score for tumor segmentation has been improved from 52% to 57% compared to the original segmentation results. In addition, the proposed method quantifies the pattern of tumor volume change into three categories such as stable, progressing, and shrinking using the volumetric changes of different tumor tissues.

### 4.2 THREE-DIMENSIONAL TEXTURE ANALYSIS

As discussed in Chapter 2, GBM grows rapidly, as a result, significant spatial deformations occur in the follow-up scans. In order to use the temporal information, it is important to relate the corresponding points or locality in the follow-up images. Therefore, in the case of large deformations spatial correspondence considerably reduces among the follow-up images for tumor and non-tumor tissues. For the comparison of deformations by GBM with that of the MS lesions, Figure 12 shows example images of GBM tumors and MS lesions at two different time points. In Figure 12, GBM tumors show significant deformations while MS lesion has no noticeable deformations.

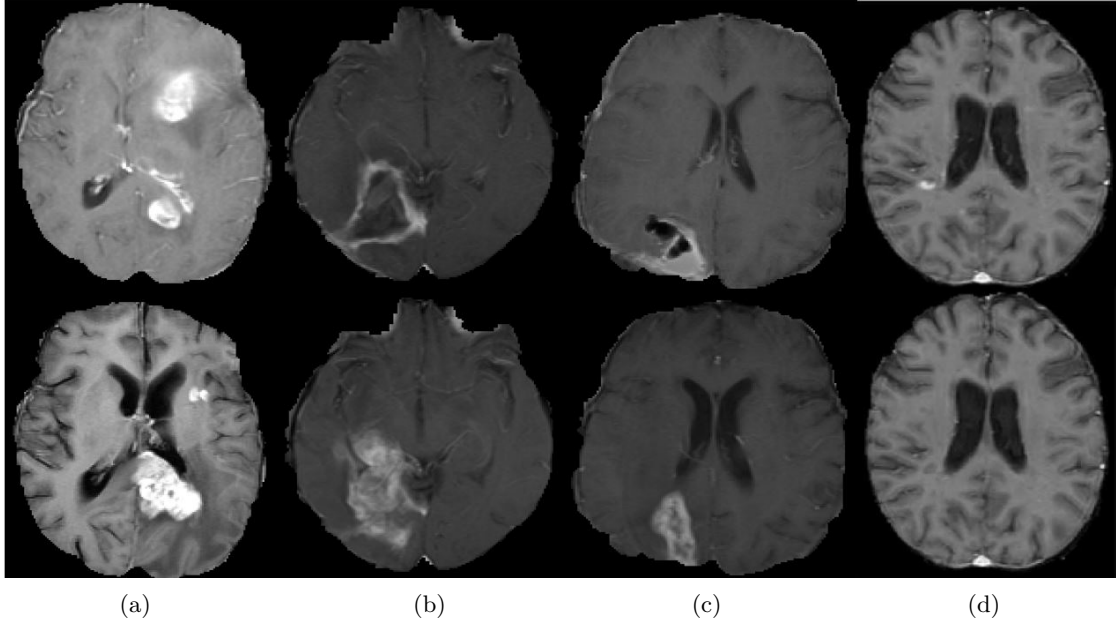


**Figure 12:** Example images at two time points for GBM tumors and MS lesions. The difference of spatial deformation and enhancement in tumors (a)-(c) and MS lesion (d) are easily identifiable at time,  $t$  and  $t'$ .

This study argues that unlike 2D texture analysis of MS lesions shown in [48], 3D texture analysis is more suitable for GBM tumor. The study also quantifies the temporal variation using specific 3D texture features; spin image, RIFT, and LBP to reduce the false positives from segmentation outcomes. Although these features are widely used in computer vision algorithms for different types of object recognition their efficacy is not investigated in medical image analysis. The primary goals of this work are to modeling a post-processing step to reduce the false positives in the results of an automatic BTS method in longitudinal MRIs, and assessing the tumor volume change over time using the improved segmentation output. Therefore, this study employed the previously proposed BTS [7] for the voxel-wise classification to demonstrate the proposed method for post-processing and tracking the change of tumor volume. In this study, the goal is two-fold: 1) model effective post-processing steps to reduce the false positives in the results of BTS methods in longitudinal MRIs, and 2) assess the tumor volume change over time using the improved segmentation output. As discussed above, due to the large-scale deformation of the tumor, the 3D texture is more amenable to relate the spatial correspondence among the follow-up images. This section provides brief discussions on the 3D hierarchical texture features that are used in this study.

#### 4.2.0.1 SPIN IMAGE FEATURE

The spin image feature first introduced in [14] to match the range data and later used as a feature in [15] for texture classification. The spin image is a 2D histogram that encodes the

intensity pattern along some concentric rings centered on a reference point. The two axes of the spin image histogram are the distance of the concentric spherical rings from the center and the normalized intensity values. Intuitively, this 2D histogram consists of a series of 1D histograms each corresponding to the intensity values of the voxels located at a fixed distance from the center. It should be noted that since these 1D intensity histograms are considered within a spherical region around the center, the spin image feature is rotation invariant. Rotation invariance is a desired property for modeling the textures of the tumor volume as they do not have a specific shape. Prior to computing the spin image feature, the intensity inhomogeneity correction and normalization to the  $[0, 1]$  range. In this work, a soft implementation as in (8) is chosen for the 2D histogram. The process allows every voxel in the detected volume to contribute at all the bins according to its location and intensity. The contribution of a voxel  $p$  with the intensity of  $I$  to the location  $(r, i)$  in the histogram is given by

$$\exp\left(-\frac{(\|p - p_0\| - r)^2}{2\alpha^2} - \frac{(I - i)^2}{2\beta^2}\right); \quad (8)$$

where,  $p_0$  is the reference/center point of the circular patch,  $r$  is the distance of the concentric rings from the center point, and the parameters  $\alpha$  and  $\beta$  are the smoothness factors along the two dimensions of the histogram. Figure 13 demonstrates the extraction process of spin image feature. Figure 14 shows the algorithm for the spin image feature extraction process.

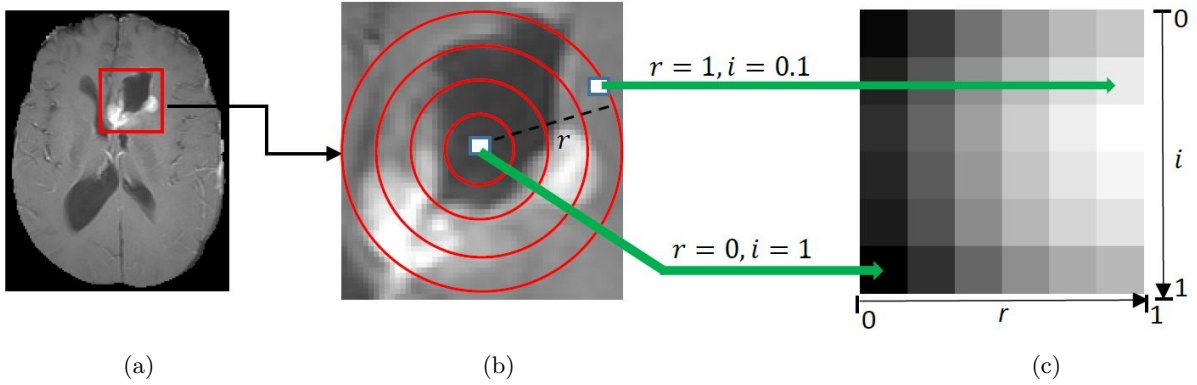


**Figure 13:** Illustration of three dimensional spin image feature extraction. a) Original image with the region of interest (ROI) in red box. Though the actual ROI is a 3D volume for the sake of clear view 2D images are shown, b) actual 3D concentric spherical rings are shown as 2D circles, and c) spin image feature extracted from a 3D volume image.

---

```

Input: 3D volume image
// image of size : L × N × M
Output: 2D histogram image
R = 0 : 0.2 : 1.0
I = 0 : 0.2 : 1.0
for each value of R do
|   for each value of I do
|   |   for each voxel do
|   |   |   Find the contribution by Eqn.(8)
|   |   |   Add the contribution to the 2D histogram at bin (I,R)
|   |   end
|   end
end
end
Normalize the histogram
return 2D histogram image

```

---

**Figure 14:** Algorithm for the 3D Spin image feature extraction.

#### 4.2.1 ROTATION INVARIANT FEATURE TRANSFORM

The Rotation Invariant Feature Transform (RIFT) [11] is the rotation invariant version of the powerful Scale Invariant Feature Transform (SIFT) [12]. It is a 2D histogram that encodes the gradient information of a sub-image. In 3D, the sub-image is actually a 3D volume image. The two dimensions of the histogram are intensity gradients of the volume image and distance of the voxels from the center of the original volume. The gradient information is collected commonly along eleven orientations of a voxel location. Similar to the spin image feature, concentric rings are used as to distance locator from the center point of the original image. Accordingly, the RIFT feature is constructed by dividing the 3D region into concentric spherical rings with equal distances from each other and computing the histogram of gradient orientations on each ring. The gradient orientation at each point is measured relative to the outward direction of the radial line passing through that point. Similar to the spin image feature, each voxel inside the region contributes to all histogram bins according to the equation (2). Note that in computing the orientation of the gradient, this implementation always picks the smaller angle between the two lines, resulting in an angle in  $[0 \pi]$ .

$$\exp\left(-\frac{(\|p - p_0\| - d)^2}{2\alpha^2} - \frac{(\theta)^2}{2\beta^2}\right); \quad (9)$$

where,  $p_0$  is the reference/center point of the circular patch,  $d$  is the distance from the center point, and the parameters  $\alpha$  and  $\beta$  are the smoothness factors along the two dimensions of the histogram. The RIFT feature extraction process and algorithm are shown in Figure 15 and 16, respectively.

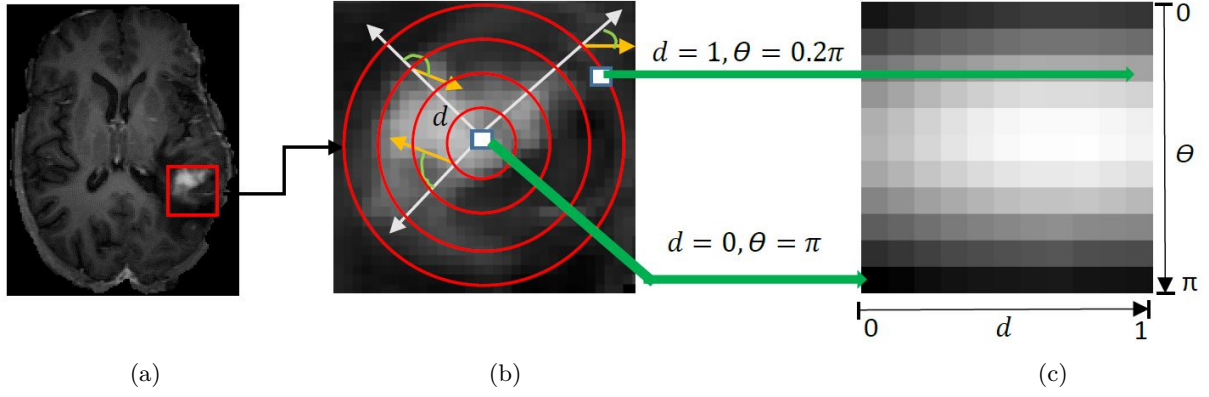


**Figure 15:** Illustration of three dimensional RIFT feature extraction process. a) Original image with the region of interest (ROI) in red box. Though the actual ROI is a 3D volume for the sake of clear visualization 2D images are shown, b) actual 3D concentric spherical rings are shown as 2D circles, and c) extracted RIFT feature.

---

```

Input: 3D volume image
// image of size :  $L \times N \times M$ 
Output: 2D histogram image
 $D = 0 : 0.2 : 1.0$ 
 $\Theta = 0 : 0.2\pi : \pi$ 
for each value of  $D$  do
  for each value of  $\Theta$  do
    for each voxel do
      Find the gradient direction
      Compute the angle,  $\theta$  as shown in Fig. 15
      Compute the contribution by Eqn.(9)
      Add the contribution to the 2D histogram at bin  $(\Theta, D)$ 
    end
  end
end
end
Normalize the histogram
return 2D histogram image

```

---

**Figure 16:** Algorithm for the 3D RIFT texture feature extraction.

#### 4.2.2 Local Binary Pattern

The Local Binary Pattern (LBP) feature extracts the local binary patterns for a point from its surrounding neighborhoods. By thresholding with its own intensity, a label [0 or 1] is assigned to every neighbor points in the image. These assigned labels are then sequentially collected to construct a binary number. The descriptor is a 1D histogram of the labels of all the points inside

the volume [16]. This study used the three dimensional LBP proposed in [17] that concatenates LBP on three orthogonal planes (LBP-TOP) of the center voxel. Figure 17 demonstrates the LBP-TOP feature extraction process while Figure 18 shows the algorithm.

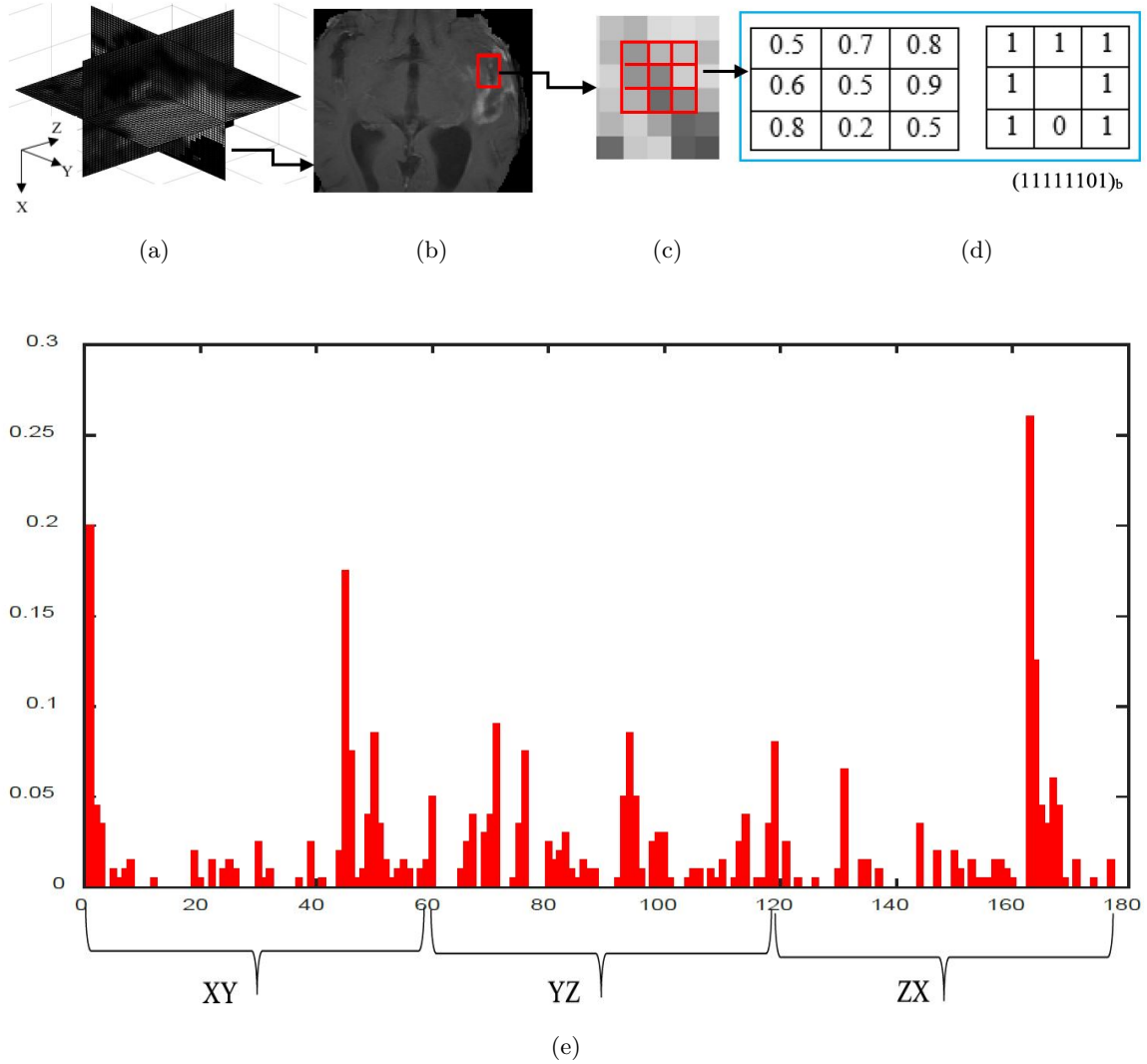


**Figure 17:** Three dimensional LBP-TOP feature extraction process. a) Three orthogonal planes of a center voxel, b) a particular plane with the region of interest, c) the  $3 \times 3$  sub-image for LBP feature extraction, d) intensity thresholding with the center pixel and the resulting binary code, and e) the LBP-TOP descriptor, concatenated histograms of three orthogonal planes.

In this work, the histogram of each plane is constructed using an operator called “*uniform patterns*” [67]. The uniformity of a pattern is defined by the number of bitwise transitions from 0 to 1 or vice versa considering the bit pattern as circular. All the binary patterns with at most two bitwise transitions are uniform and else are non-uniform. For example, the patterns

11111111 (0 transitions), 00011000 (2 transitions) and 10001111 (2 transitions) are uniform

---

```

Input: 3D volume image
// image of size :  $L \times N \times M$ 
Output: 1 – D histogram
for each voxel do
    Find the three orthogonal planes, XY, YZ, ZX
    for each plane do
        Extract the  $3 \times 3$  image patch centering the voxel
        Perform threshold to get the binary profile as in Fig. 17
        Map the binary code to the histogram bin
        using “Uniform pattern”
        Increase the counter of corresponding bin
    end
    Normalize the histogram
end
Concatenate the 3 histograms
return Concatenated 1 – D histogram

```

---

**Figure 18:** The LBP-TOP texture extraction process.

whereas the patterns 10011001 (4 transitions) and 01001001 (6 transitions) are non-uniform. In uniform LBP coding, each uniform pattern has a separate bin in the histogram while all the non-uniform patterns are assigned to a single bin. Accordingly, for eight neighbor points, there are 59 histogram bins. Therefore, for three orthogonal planes total 177 bins are seen in the concatenated histogram in Figure 17. In this study, *Uniform Patterns* is chosen for two reasons; i) most of the local binary patterns in natural images are uniform, and ii) it is statistically robust being less prone to noise. For the sake of simplicity, LBP-TOP is referred as LBP in the rest of this dissertation.

### 4.3 METHODOLOGY

The method starts with voxel-wise classification using our previously proposed automatic BTS [7]. Details about the parameter setting of the random forest classifier for this multiclass segmentation can be found in [7]. The simplified flow diagram of the proposed method to improve the segmentation and assess the tumor volume change is shown in Figure 19.

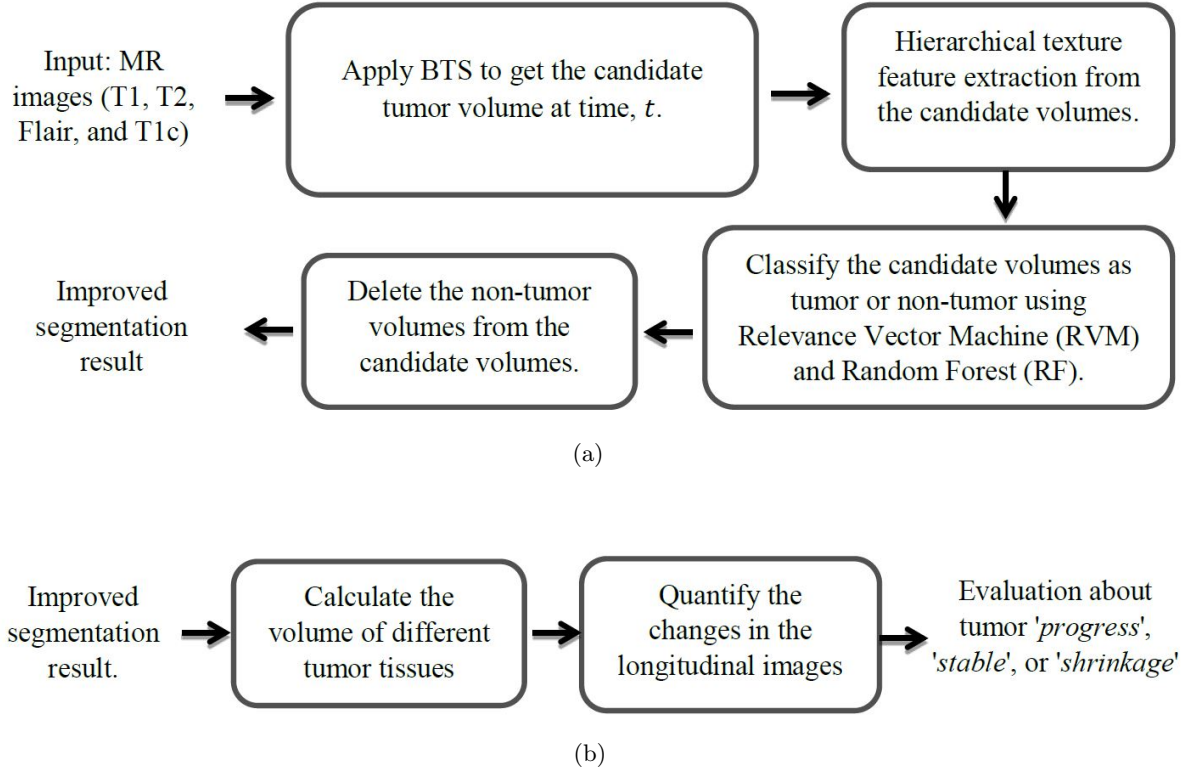


**Figure 19:** Simplified flow diagram of the proposed method for improving the brain tumor segmentation in longitudinal images. a) Improving the segmentation, and b) assessing the change of volume in longitudinal images.

A brief description of the above methods is given below.

#### 4.3.1 CANDIDATE VOLUME GENERATION USING BTS

The method starts with the multiclass voxel-wise classification of brain abnormal tissues at time  $t$ . Any automatic segmentation method with high sensitivity and moderate FP can be employed for this task. In this study, BTS [7] method is used to classify the brain abnormal tissues as necrosis, edema, enhanced, and non-enhanced tumors. The efficacy of BTS method is statistically validated using BRATS-2013/2014 challenge [61][62] dataset. Despite excellent ranking in the challenges, significant false positives outside of the tumor regions appeared to have compromised the overall performance of the method. This work aims to reduce the false positives from the BTS outcome. These detected volumes are referred as candidate volumes. Prior to the feature extraction, each candidate volume is labeled ( $y_{vol}$ ) with  $1$  if it contains any tumor voxels, else the label is  $0$ .



### 4.3.2 HIERARCHICAL TEXTURE FEATURE EXTRACTION

In the second step, the original input image regions inside the bounding box of the candidate volumes are considered as the region of interest (ROI) for feature extraction. The aforementioned 3D textures features (spin image, RIFT and LBP) are defined in two categories; stationary texture features ( $H_{v,t} \in \{spin^t, RIFT^t, LBP^t\}$ ) and temporal texture ( $H_{v,t'} \in \{spin^{t'}, RIFT^{t'}, LBP^{t'}\}$ ) features. The features are called stationary texture when it is extracted from the images at time  $t$  and temporal textures when the images are at time  $t'$ . Both stationary and temporal textures are extracted using the same bounding boxes which is derived from the candidate volumes at time  $t$ . Figure 20 demonstrates about the ROIs for the stationary and temporal texture feature extraction with 2D slice images. It should be noted that the 3D texture (spin image, RIFT, LBP) for both stationary and temporal cases are extracted from the four MR image modalities: T1, T1c, T2, and Flair.

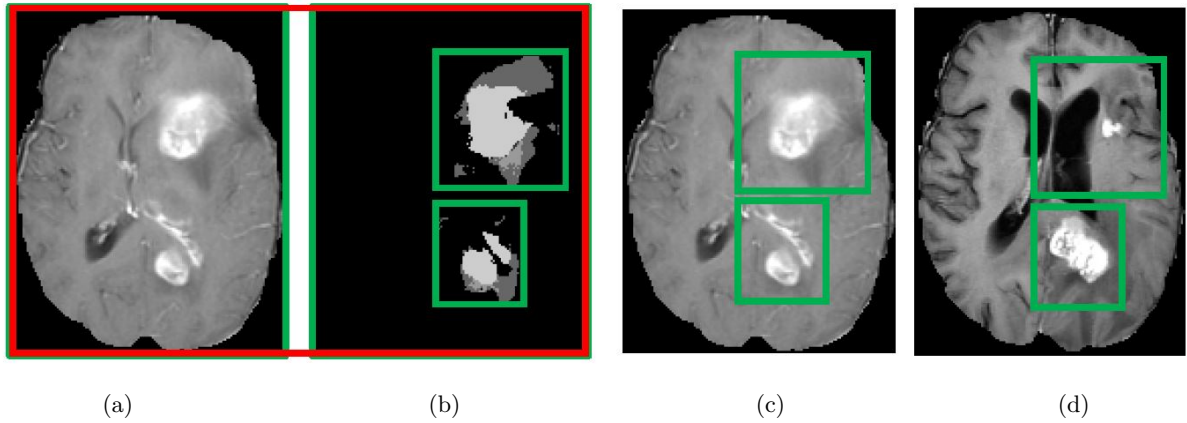


**Figure 20:** Demonstration of ROI for hierarchical feature extraction. The regions are extracted from the original detection of BTS for both stationary and temporal features. a) Image T1c at time  $t$ , b) the detected tumor with the bounding boxes for the image at time  $t$ , although four modalities (T1, T1c, T2 and Flair) are used but for the sake of clear view we show only T1c, c) stationary feature are extracted from the image at time  $t$  using its bounding box, and d) temporal features are extracted from the image at time  $t'$ .

### 4.3.3 CANDIDATE VOLUME CLASSIFICATION AS TUMOR/ NON-TUMOR

After the hierarchical (stationary and temporal) texture feature extraction, the next step is to classify each candidate volume as tumor or non-tumor. For the above two types of texture features ‘stationary’ and ‘temporal’ two separate classifiers ‘*stationary classifier*’ and ‘*temporal classifier*’ are obtained respectively. The goal of the ‘stationary classifier’ is to find the probability  $p(y_{vol}|H_{v,t})$  of the candidate volumes where  $p(y_{vol}|H_{v,t})$  determines whether the stationary texture

( $H_{v^t}$ ) of a candidate volume is more similar to a texture of a tumor volume or to that of a non-tumor. Therefore, from all the candidate volumes at time  $t$  in the training data, a randomly  $N_s$  number of volumes with an equal number of tumor and non-tumor labels are selected as a static set ( $C_S$ ) and fixed for the rest of the steps. The stationary feature of a new candidate volume is compared with the features of each member of the static set ( $C_s$ ). Instead of comparing the features directly, a histogram-based distance metric named as earth movers distance (EMD) [68] is used to measure the distance between  $H_{v^t}$  and  $C_{sH_{v^t}}$ , where  $H_{v^t}$  is the stationary textures of a candidate volume and  $C_{sH_{v^t}} \in \{H_{v_1^t}, H_{v_2^t}, \dots, H_{v_{N_s}^t}\}$  is stationary features of the static set. The EMD is calculated for each texture features (spin image, RIFT, LBP) and three separate relevance vector machine (RVM) [69][70] classifiers are used to find the desired probabilities. Similarly, the remaining  $N_T$  candidate volumes of the training set is named as the temporal set ( $C_T$ ). From the temporal set, both stationary  $H_{v^t}$  and temporal  $H_{v^{t'}}$  features extracted. The temporal classifier uses the EMD [71] distance between  $H_{v^t}$  and  $H_{v^{t'}}$ , which finds the probability  $p(y_{vol}|H_{v^t}, H_{v^{t'}})$ . Where  $p(y_{vol}|H_{v^t}, H_{v^{t'}}$  determines whether the temporal behavior in the follow-up images of a candidate volume are more similar to a tumor or to that of a non-tumor. The random forest (RF) [60] is used as the temporal classifier to classify all three texture (spin, RIFT, LBP) features of all four modalities. In short, the stationary feature of a test volume is compared with 1) the stationary features of the static set, and 2) its own temporal features.

#### 4.3.4 FINAL PREDICTION ABOUT THE CANDIDATE VOLUMES

Finally, the probabilities provided by the classifiers (RVM, RF) are averaged and threshold to get the binary decision of the test volume. The test volumes with zero labels are removed from the original detection and thus output is the improved segmentation result with less false positives. As part of this goal for tumor volume tracking, we quantify the tumor changes in longitudinal images.

#### 4.3.5 CORE AND ACTIVE TUMOR VOLUME CALCULATION

The changes of tumor core (sum of necrosis, enhanced, non-enhanced) and active tumor (enhanced and non-enhanced) volumes are measured in terms of the cubic millimeter ( $\text{mm}^3$ ).

#### 4.3.6 QUANTIFICATION OF CHANGES

The ratio of the volumes ( $V^{t'}/V^t$ ) of both tumor core and active tumor (enhanced) are used and identified the change of tumor volume as 'progressing', 'stable', or 'shrinking'.

## 4.4 EXPERIMENTS AND RESULTS

This section provides the tumor segmentation and growth assessment in longitudinal MRIs.

### 4.4.1 DATASET

For this study, total 96 longitudinal MR images of 19 patients are collected from BRATS-2015 [72] multi-center datasets. Additional MRI images of 30 patients in BRATS-2013 training dataset are used for training the classifier used for automatic segmentation of the candidate volumes. In this study, four MR modalities: T1, T1c, T2 and Flair images are used. Since MR images in BRATS dataset are already skull-stripped and co-registered, the method performs intensity inhomogeneity correction through channel-wise histogram matching with the images of a randomly selected patient as the reference.

### 4.4.2 AUTOMATIC SEGMENTATION OF BRAIN TUMOR

For candidate volume segmentation, the BTS method is trained with MR images of 30 patients in the BRATS-2013 training dataset and tested on 96 longitudinal scans of BRATS-2015. Details about the parameter setting of the random forest classifier for this multiclass segmentation can be found in [6], in which we develop an automatic brain tumor segmentation (BTS) method and statistically validated [7][4] its efficacy using BRATS-2013/2014 dataset. Despite excellent ranking of our BTS method in the challenges, significant false positives outside of the tumor regions appeared to have compromised the overall performance. Based on 26 connected components all 3D objects less than 50 voxels are removed from the BTS outcome and the remaining 3D objects are considered as candidate volumes. In this work, it is assumed that tumor volumes are above 50 voxels. In addition, the method carefully applies a morphological operation that fills the small holes in the detected regions either with a necrosis or an enhanced label which is decided by the neighbors' majority labels. Figure 21 shows two example images with BTS outcome and the radiologist's outline.

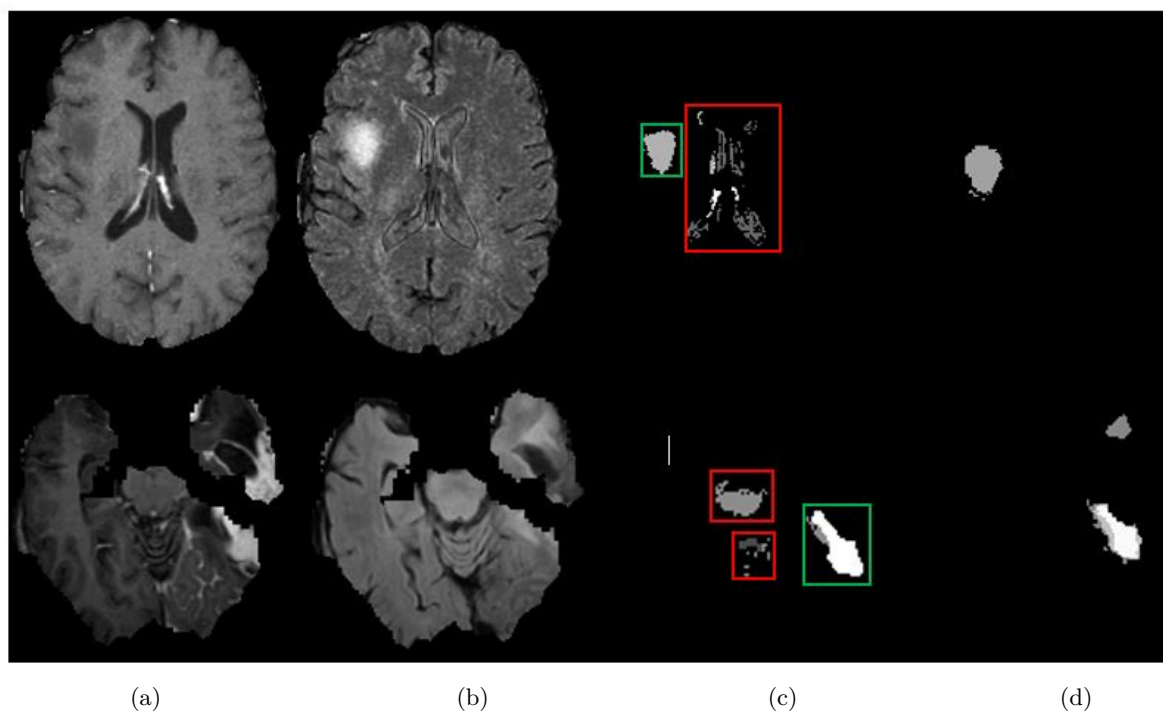


**Figure 21:** Example images of BTS outcomes with the appearance of significant false positives. Input images a) T1c & b) Flair, c) output of the BTS method, all the candidate volumes are marked with boxes, and d) radiologists' manual outline (ground-truth). Actually, four modalities (T1, T1c, T2 and Flair) are used but for the sake of a clear view only T1c and Flair are shown in figure. The red box indicates false positives outside of the tumor regions and the green box is the actual tumor region.

In Figure 21, MR slice images are shown for two arbitrary patients. The red boxes are the non-tumor detection (FP) and the green boxes are the tumor detection (TP) in the BTS outcome. For a clear understanding about the TP and FP in the segmentation outcome, 3D view is given in Figure 22. The FPs in the original segmentations are easily seen in Figure 22. However, the image in Figure 22(a) is slightly rotated and scaled to show all the FPs.

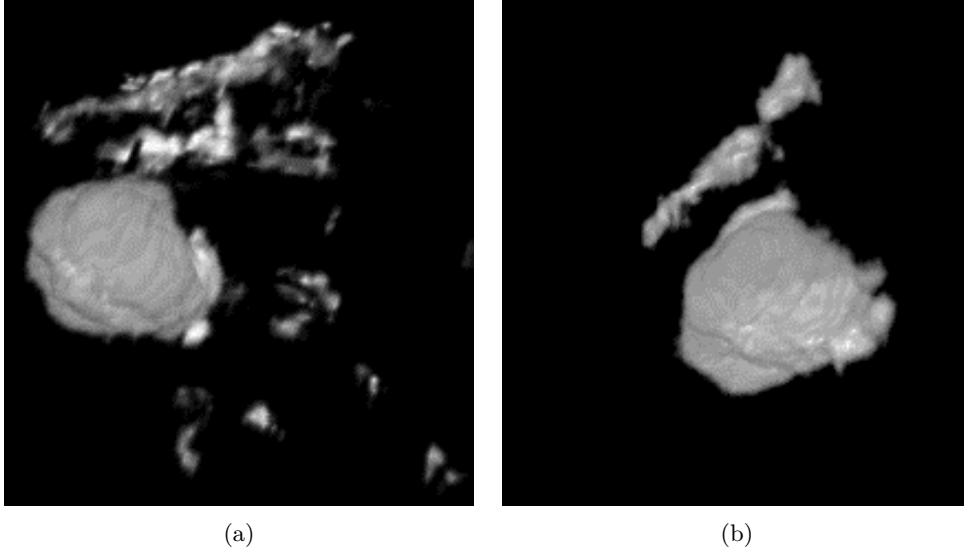


**Figure 22:** Three dimensional view of the false positives in BTS outcomes and the ground-truth. (a) BTS outcome and (b) ground-truth. The false positives in the original detections are easily seen in (a).

#### 4.4.3 STATIC AND TEMPORAL FEATURE EXTRACTION

Prior to feature extraction, the 96 MRI scans of 19 patients are redistributed in such a way that each MR scan has a pair with its closest follow-up scan. For example, if a patient has five time-scan data at time  $t_1, t_2 \dots t_5$ , then they are distributed in three pairs  $t_1 - t_2, t_3 - t_4$ , and  $t_4 - t_5$  for the temporal analysis. In this dissertation, the first time point of each pair is denoted as  $t$  and second time point as  $t'$ , respectively. Pairing the images with their follow-up scans results in 51 possible pairs for the whole dataset. As mentioned in the methodology section, static and temporal texture features are then extracted at time  $t$  and  $t'$  respectively.

#### 4.4.4 TRAINING AND TESTING OF THE CLASSIFIERS

The method is evaluated with a 10 fold cross validation using the paired dataset, which means in a single fold around 45 pairs are used for training and 5 pairs are in testing. All the candidate volumes in the training dataset are randomized and further divided into two sets ( $S_1$  &  $S_2$ ) with 70:30 ratio. In this work, the dataset  $S_2$  is used as a validation set. From  $S_1$ , randomly 50 candidate voxels are selected with an equal number of tumor and non-tumor candidates as the static set,  $C_s$ . The remaining candidate volumes in  $S_1$  are considered as the temporal set,  $C_T$ . Figure 23 demonstrates the dataset distribution for a single fold.

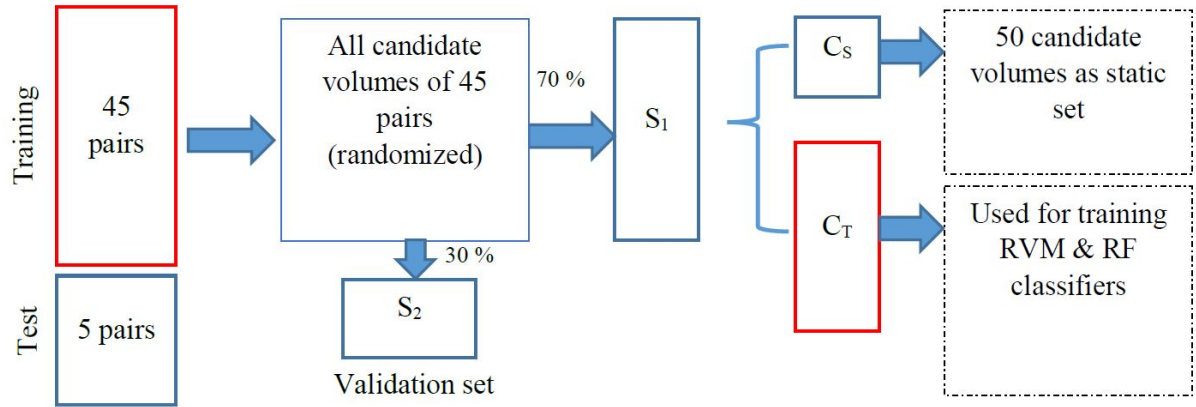


**Figure 23:** Data distribution for training, validation, and test for hierarchical texture feature extraction. In figure data distribution is shown for a single fold.

Three RVM classifiers are trained using the EMD-L1 [68][73] distances between the stationary texture features of set  $C_s$  and  $C_T$ . Similarly, the single RF classifier is trained using the EMD-L1 distances between the stationary and temporal texture features of the set,  $C_T$ . The trained classifiers are then applied on both validation ( $S_2$ ) and the original test datasets. Figure 24 shows the receivers operating characteristics curve (ROC) of the four classifiers for the validation dataset of a randomly selected fold.

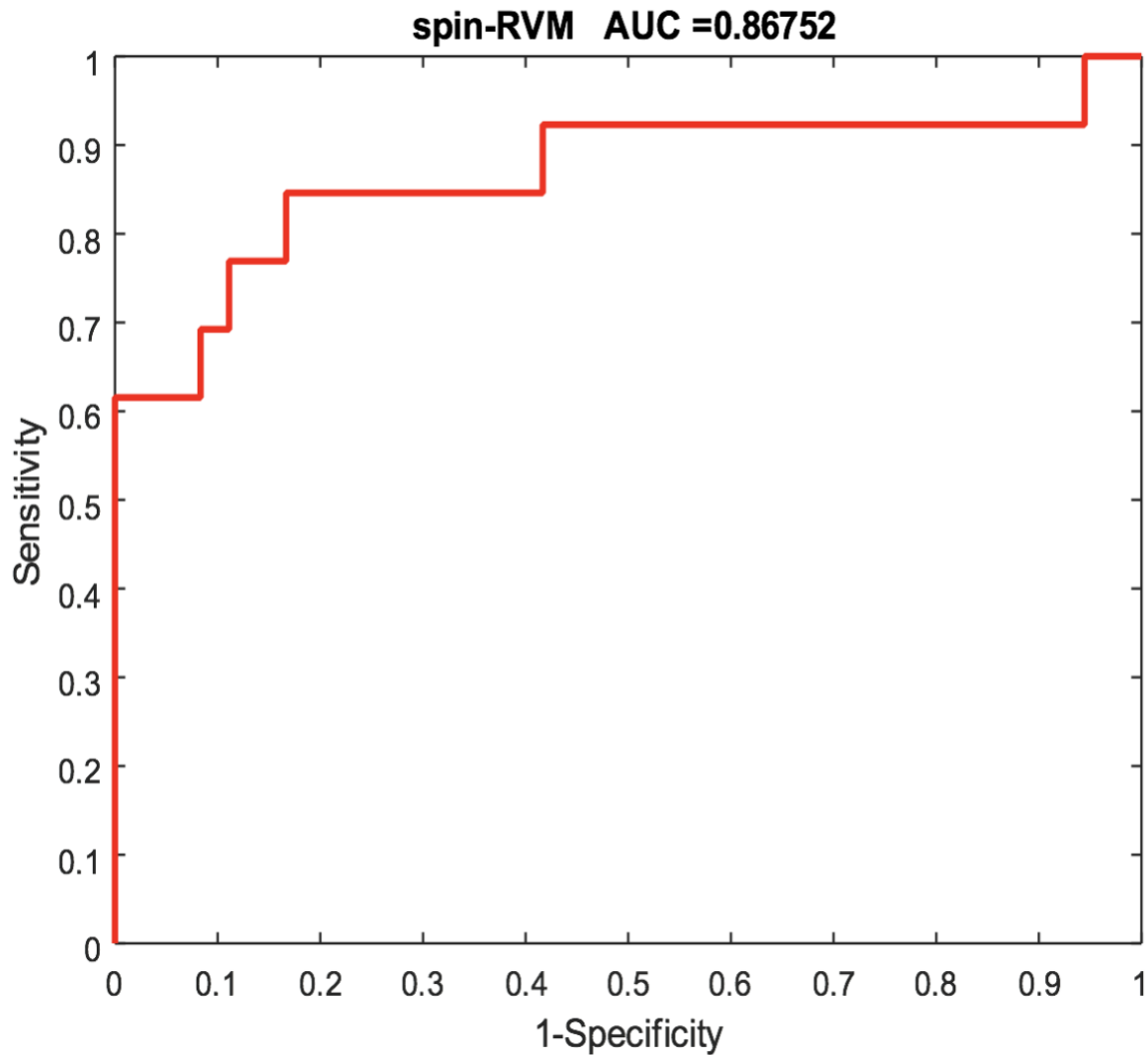
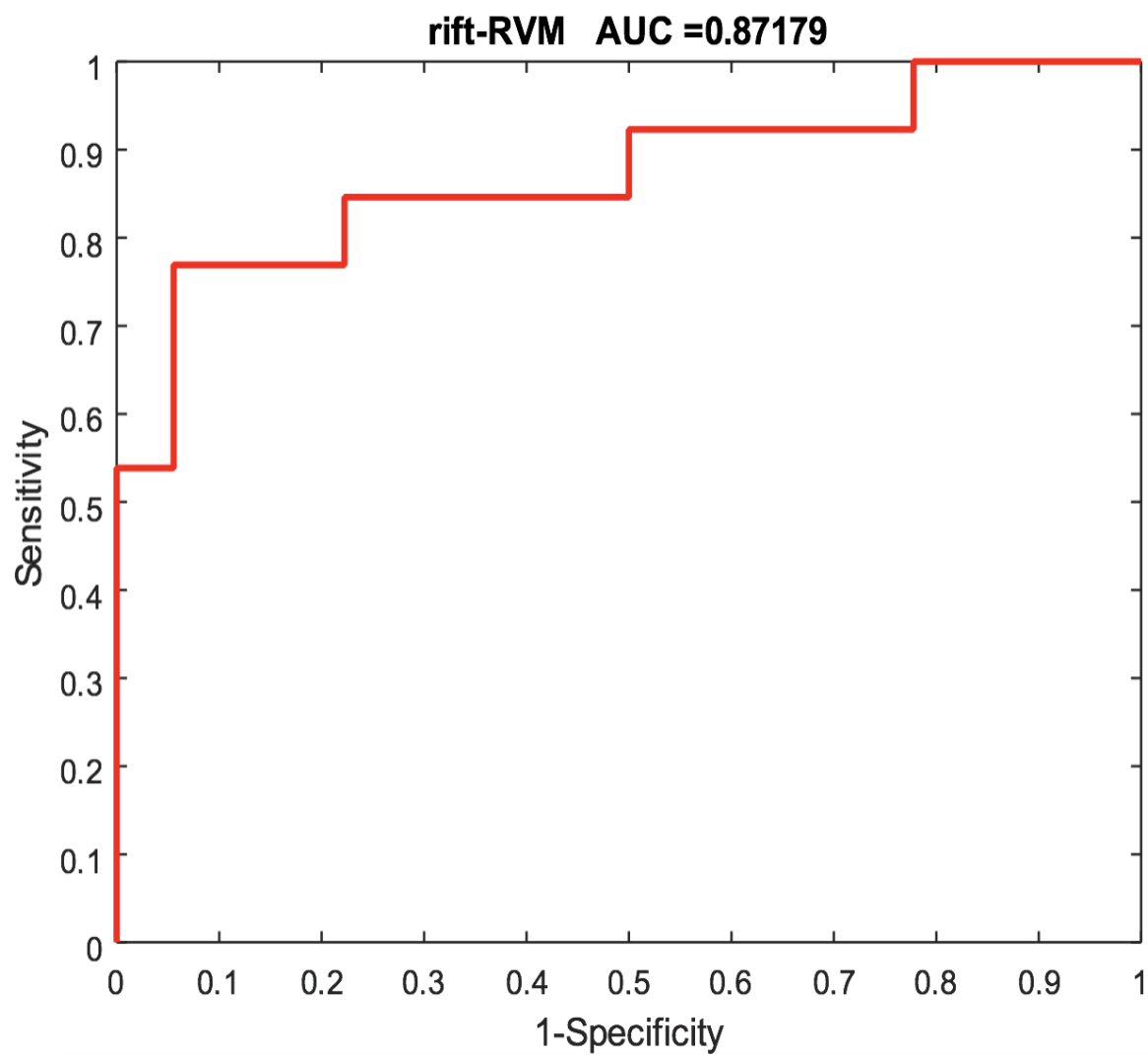


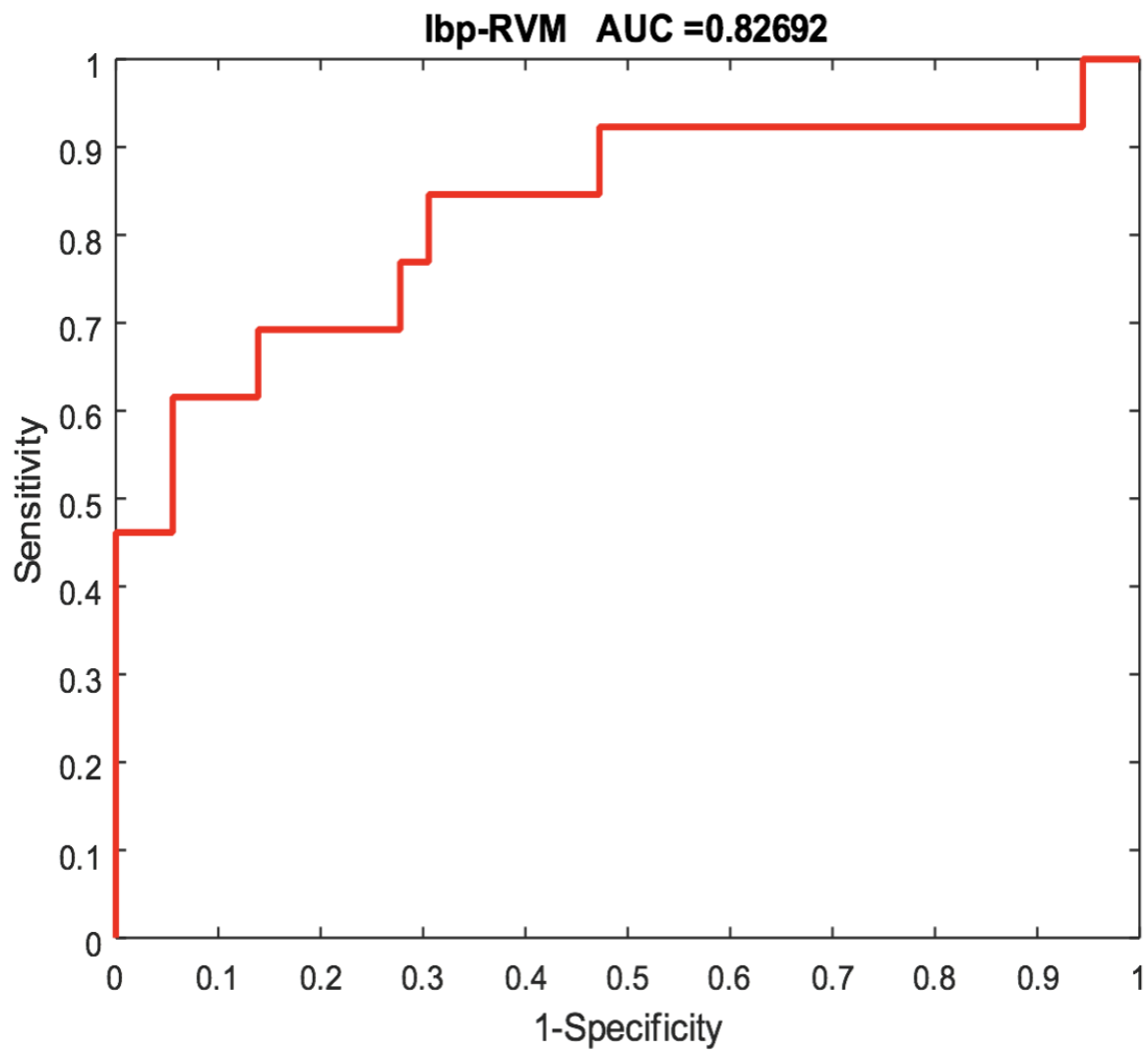
**Figure 24:** Classifiers performance using the hierarchical texture features. Candidate volumes are classified as tumor and non-tumor. The four classifiers (3 RVM and a single RF) are used. The three stationary texture features are classified separately by RVM; a) Spin image, b) RIFT, c) LBP, and d) all three temporal features are classified using a single RF classifier.



(b)

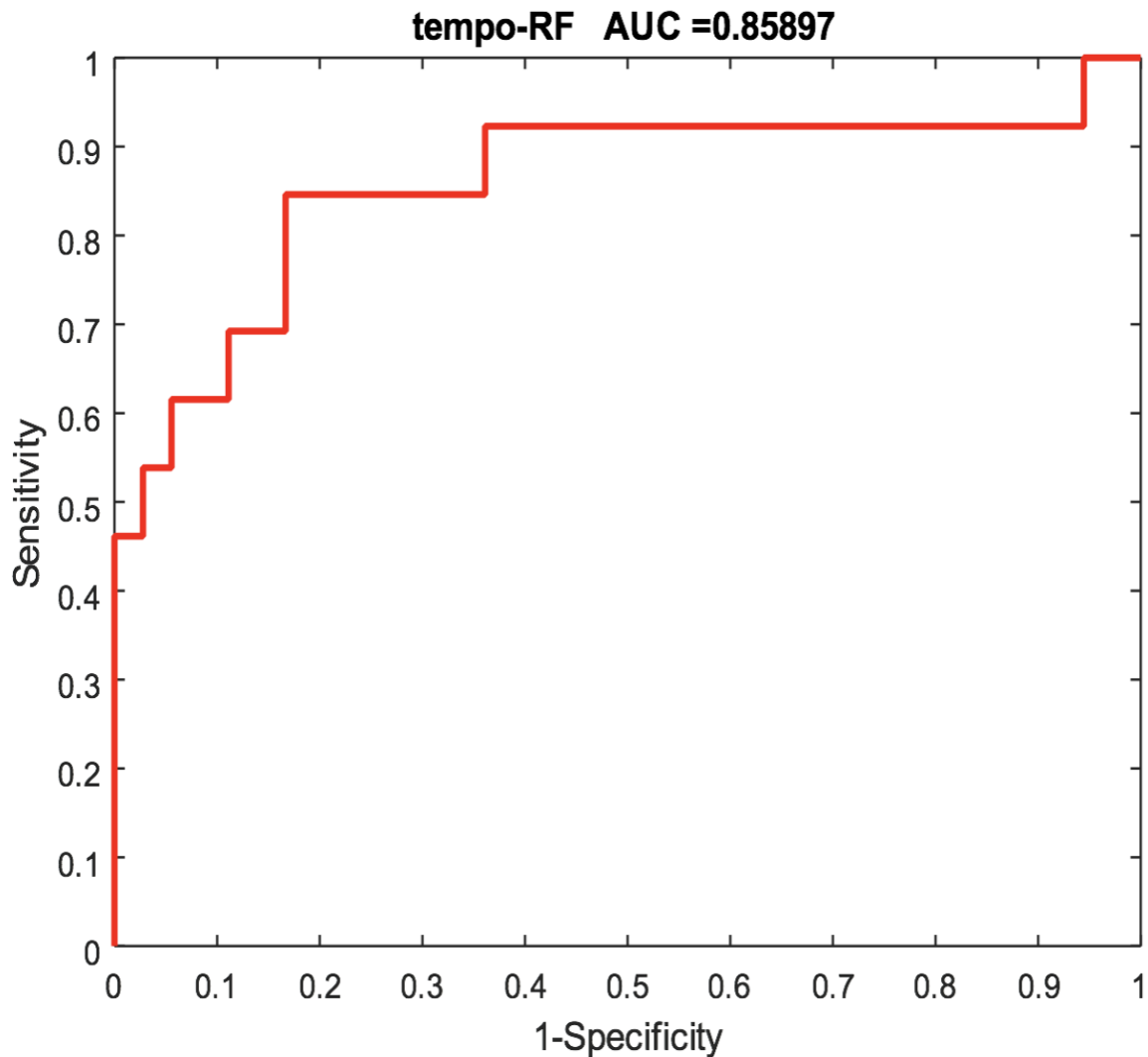
Figure 24. (continued)





(c)

Figure 24. (continued)



(d)

Figure 24. (continued)

The obtained AUCs of these classifiers varies from 83% to 87%, which indicates that the defined classifiers are effective in discriminating the tumor volumes from non-tumors. However, observation of this study suggests that averaging the scores of the four classifiers yield consistent performance over all the folds. Therefore, the final probability  $p(y_{vol})$  of each candidate volume is obtained by averaging the weighted scores of the four classifiers. The weights are the ratio of the volume of that candidate to the total volumes of all the candidates for a corresponding patient. The final probability  $p(y_{vol})$  is thresholded to obtain a binary decision for each candidate volume. The optimal threshold value is obtained using the weighted average scores of the validation dataset. MATLAB performance curve analysis [74] function “*perfcurve*” is employed to obtain

the optimal operating point for the ROC curve which uses the slope,  $m$  given by equation (10)

$$m = \frac{Cost(\frac{P}{N}) - Cost(\frac{N}{N})}{Cost(\frac{N}{P}) - Cost(\frac{P}{P})} \times \frac{N}{P}; \quad (10)$$

where,  $Cost(N|P)$  is the cost of misclassifying a positive class as a negative class and  $Cost(P|N)$  is the cost of misclassifying a negative class as a positive class,  $P$  and  $N$  are the total instance counts in the positive and negative class, respectively. Finally a straight line with slope,  $m$  is moved from the upper left corner to the bottom right corner of the ROC plot, until it intersects the ROC curve. The threshold value corresponding to that intersecting point is found to be optimal. Figure 25 demonstrates the procedure of finding the optimal threshold from a ROC curve. Note that due to our small sample size, the ROC curve of the validation dataset is very discrete. In order to find the suitable threshold value, we use a polynomial fit of degree two and then apply the above procedure. The obtained threshold value is shown by the cross mark on the fitted curve.

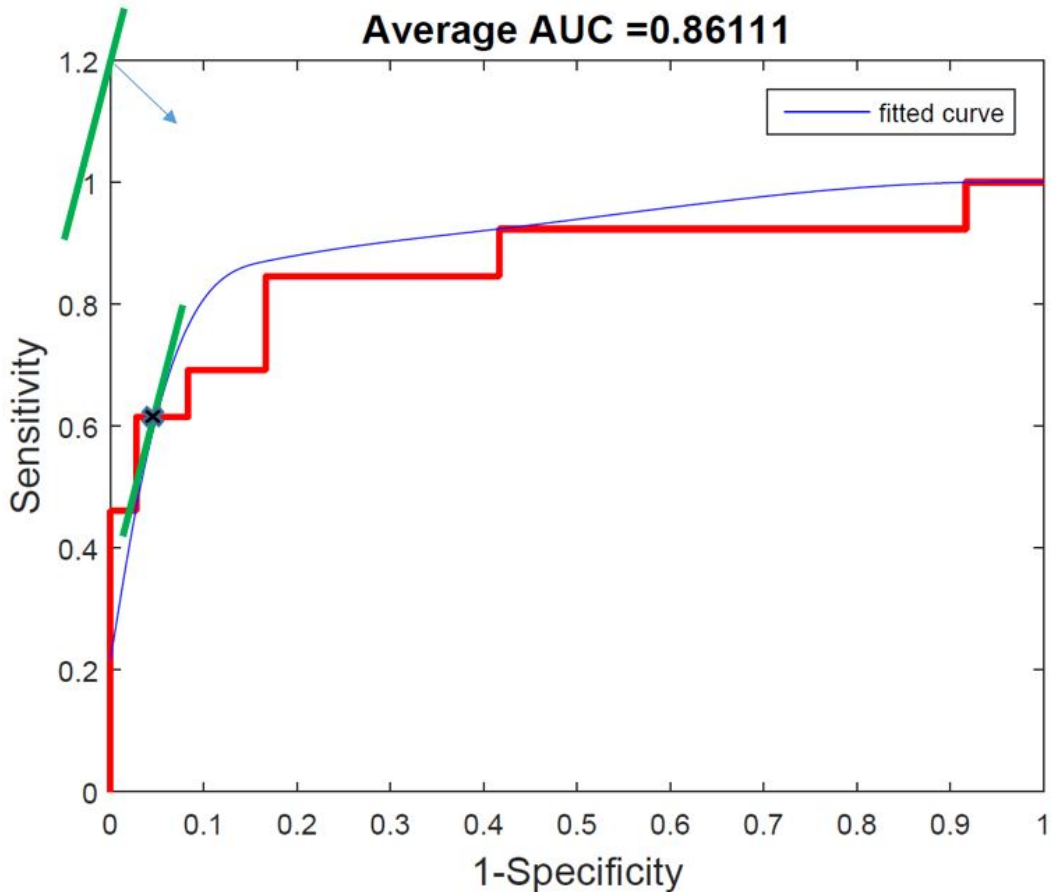


**Figure 25:** Demonstration of finding optimal threshold. Cost and slope of the ROC curve are used by the MATLAB performance curve analysis function, “*perfcurve*” [74].

#### 4.4.5 IMPROVED SEGMENTATION RESULT

In order to obtain improved segmentation result, the optimal threshold value identified using the validation set is applied on the final probabilities of the test dataset. Probabilities below the threshold value are labeled as '0' and the corresponding candidate volumes are removed from the original detection. Figure 26 shows example images of the segmentation results. Note that the tumor segmentation is done in 3D, however, for visualization purposed only 2D image are shown in Figure 26.

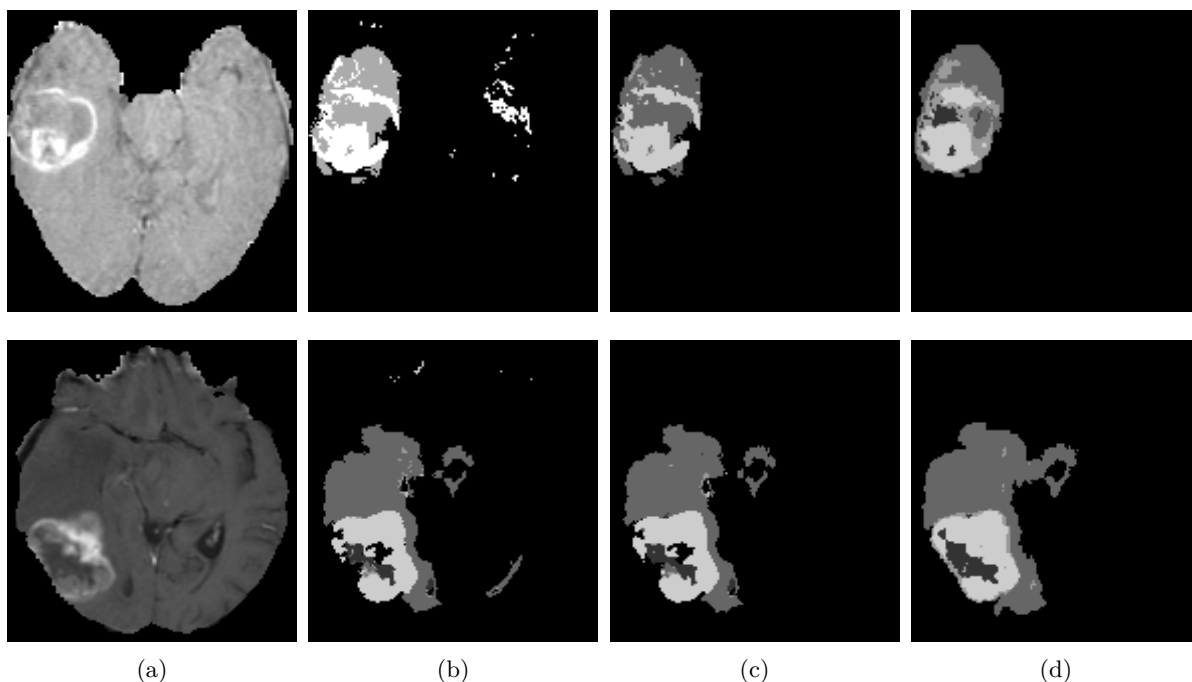


**Figure 26:** Improved segmentation outcomes using hierarchical texture-based post-processing method. Example images of improved segmentation outcomes for two arbitrary MR slices, a) T1c input image, b) original segmentation by BTS, c) improved segmentation outcome by the proposed method, and d) manual outline. The reduced false positives are seen in the refined result (c).

Figure 27 shows the original segmented tumor using BTS, the improved segmentation with reduced FPs, and the manual outline.

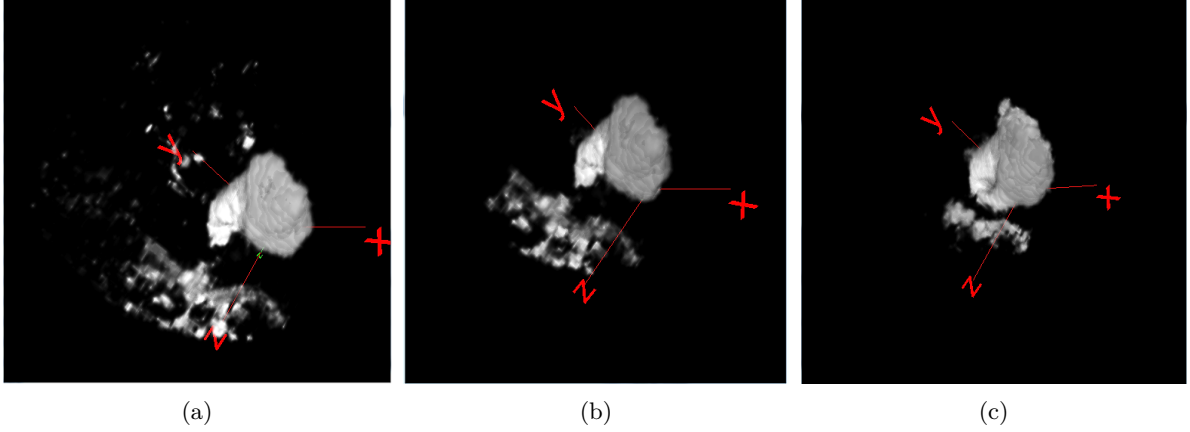


**Figure 27:** Three dimensional visualization of the improved segmentation result. Example images are shown for a) original BTS outcome, b) improved segmentation outcome by the proposed method, and c) manual outline. The reduced false positives are seen in the improved result (b).

*Quantitative evaluation:* The proposed method is evaluated using 96 longitudinal MRI scans of 19 patients using BRATS-2015 clinical dataset. Three different categories such as the complete tumor, tumor core, and other tissues are considered for the evaluation. The details on these three categories are as follows: Complete Tumor: (1-necrosis, 2-Edema, 3-non-enhancing tumor, 4-enhance tumor); Tumor Core: (3-non-enhance tumor, 4-enhance tumor); and other tissues. The performance of the proposed method is evaluated by following four metrics: percentage of reduced false positive (PRFP), positive predictive value (PPV), Dice, and sensitivity. The metrics are defined as follows;

$$\begin{aligned}
 PRFP &= \frac{(\sum FP)_{before} - (\sum FP)_{after}}{(\sum FP)_{before}}, & PPV &= \frac{\sum TP}{\sum (TP + FP)}, \\
 Dice &= \frac{2TP}{2TP + (FP + FN)}, & \text{and } Sensitivity &= \frac{\sum TP}{\sum (TP + FN)}
 \end{aligned} \tag{11}$$

where TP, FP and FN are the true positive, false positive and false negative, respectively. The PRFP, PPV, Dice overlap, and sensitivity are plotted using the original segmentation by BTS and the refined segmentation in Figure 28.

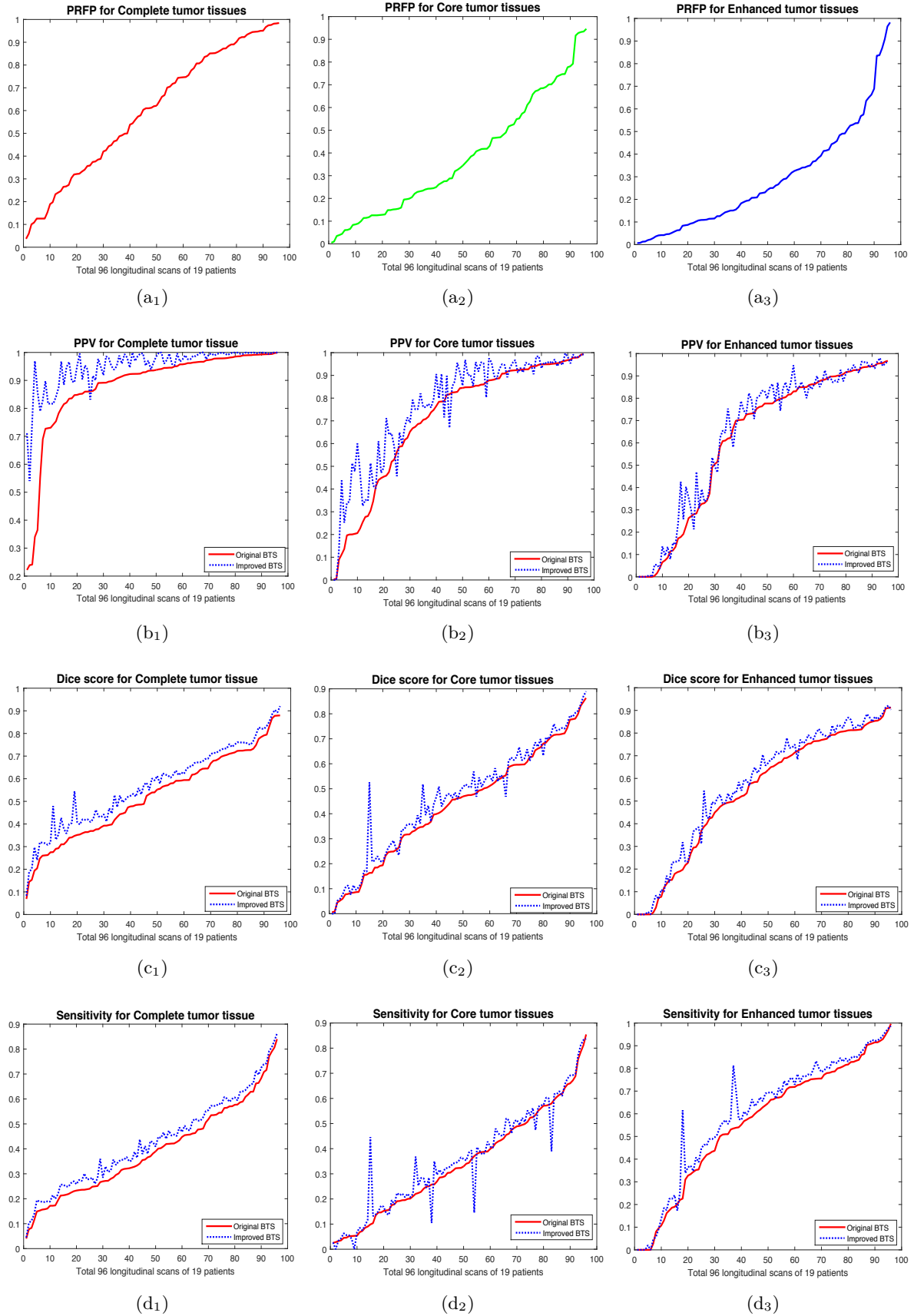


**Figure 28:** Plots of the quantitative scores of the improved segmentation results using the proposed. Plots are shown for the 96 time scan data of 19 patients. a) PRFP, b) PPV, c) Dice coefficient, and d) Sensitivity. Dashed line indicates the scores obtained using the improved segmentation result and the solid line using the original BTS outcomes.

Plots in Figure 28 (a) show that significant amount of FPs are reduced in all three categories, specifically for the complete tumor. Note the FPs in the original detections appear as edema which are included in the complete tumor category, and hence reductions of these falsely detected edema tissues greatly improves the complete tumor. Few other candidate volumes are also detected as other tissue types, which improves the core and enhanced category. On an average 62%, 40%, and 30% of FPs are reduced from the original detections for complete, core, and enhanced tumors, respectively. Following Equation (11), PPV has a strong relation to the FPs and thus PPV score is also improved significantly. Similarly, the Dice score is also improved by an average 5% for the complete tumor. However, the total volume of the FPs are very low compared to the tumor volumes, hence reducing the FPs even by 62% has marginal effects on the Dice score. Although sensitivity is not related to the FP, an improvement in this score is also noticed due to the morphological operation. Note that in the first step of this preprocessing step, we carefully apply a morphological operation that fills the small holes and thus improved the sensitivity. In Table 8, all the quantitative scores are shown using the original segmentation and improved segmentation. The overall performance for this dataset is compromised by the imaging artifacts in the MRI, as shown in Figure 29.

**Table 8:** Comparison of the quantitative scores for the original BTS segmentation and the improved result using the proposed 3D texture-based post-processing method.

	Scores	PRFP			PPV			Dice			Sensitivity		
		<i>Complete</i>	<i>Core</i>	<i>Enhanced</i>	<i>Complete</i>	<i>Core</i>	<i>Enhanced</i>	<i>Complete</i>	<i>Core</i>	<i>Enhanced</i>	<i>Complete</i>	<i>Core</i>	<i>Enhanced</i>
Original BTS	Avg.				0.88	0.71	0.62	0.52	0.44	0.54	0.39	0.34	0.59
	Std.	0.62	0.40	0.30	0.16	0.28	0.33	0.19	0.23	0.28	0.18	0.21	0.26
Improved BTS	Avg.	0.26	0.26	0.25	0.95	0.77	0.64	0.57	0.46	0.57	0.43	0.36	0.63
	Std.				0.07	0.24	0.32	0.18	0.23	0.28	0.18	0.21	0.25

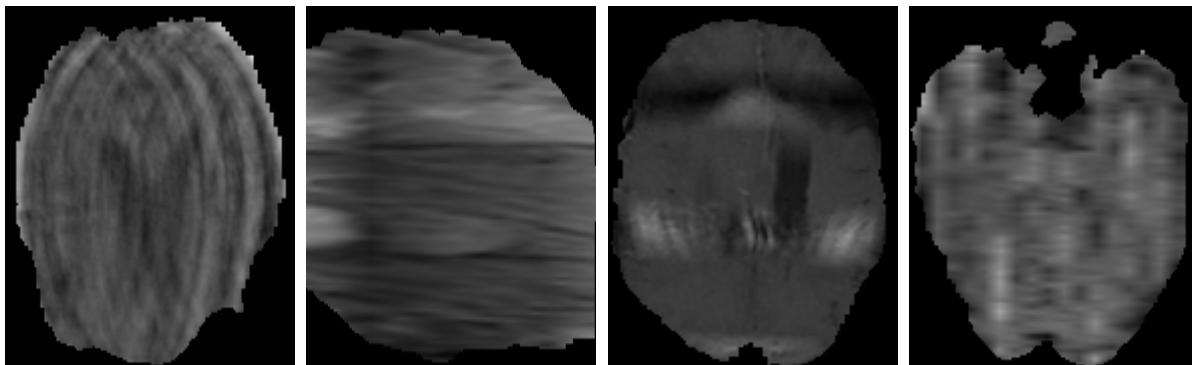


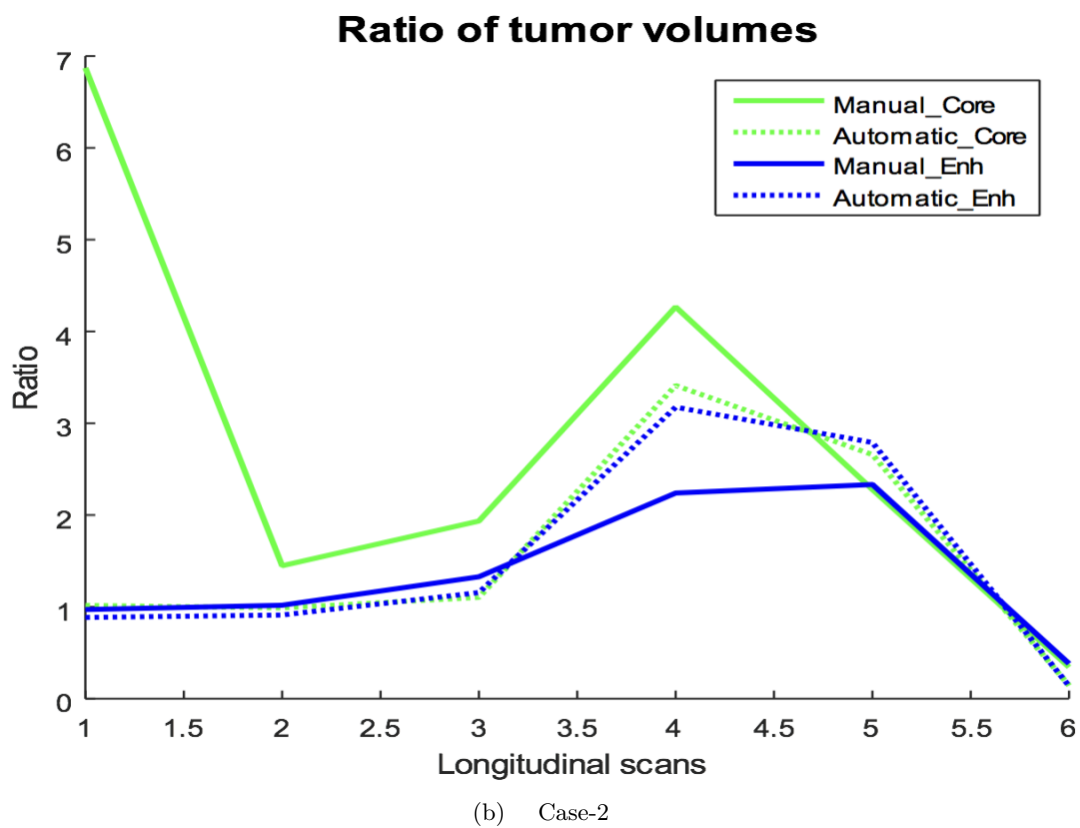
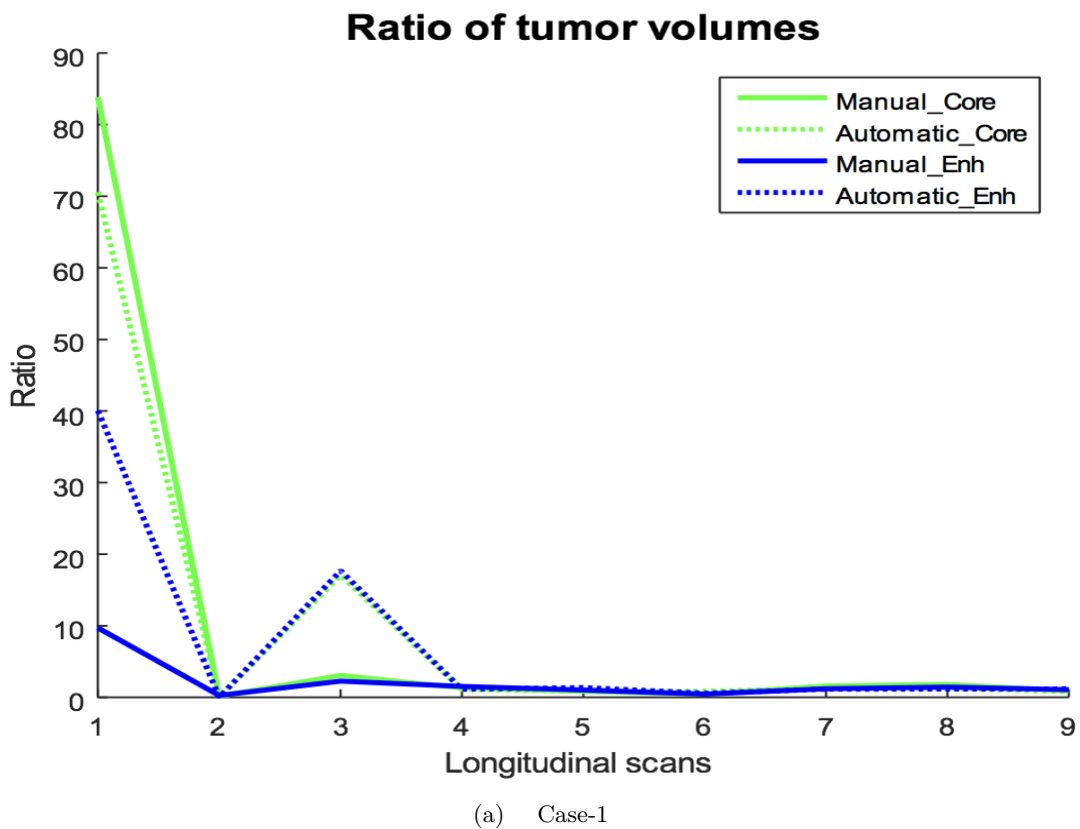
**Figure 29:** Example of some problematic images (imaging artifacts) in BRATS-2015 dataset. These images limits the classifiers performance and thus compromised the overall segmentation output of the proposed method.

Moreover, this study uses MR images of 30 patients in training dataset of BRATS-2013, which may not be enough to train the BTS automatic segmentation classifier.

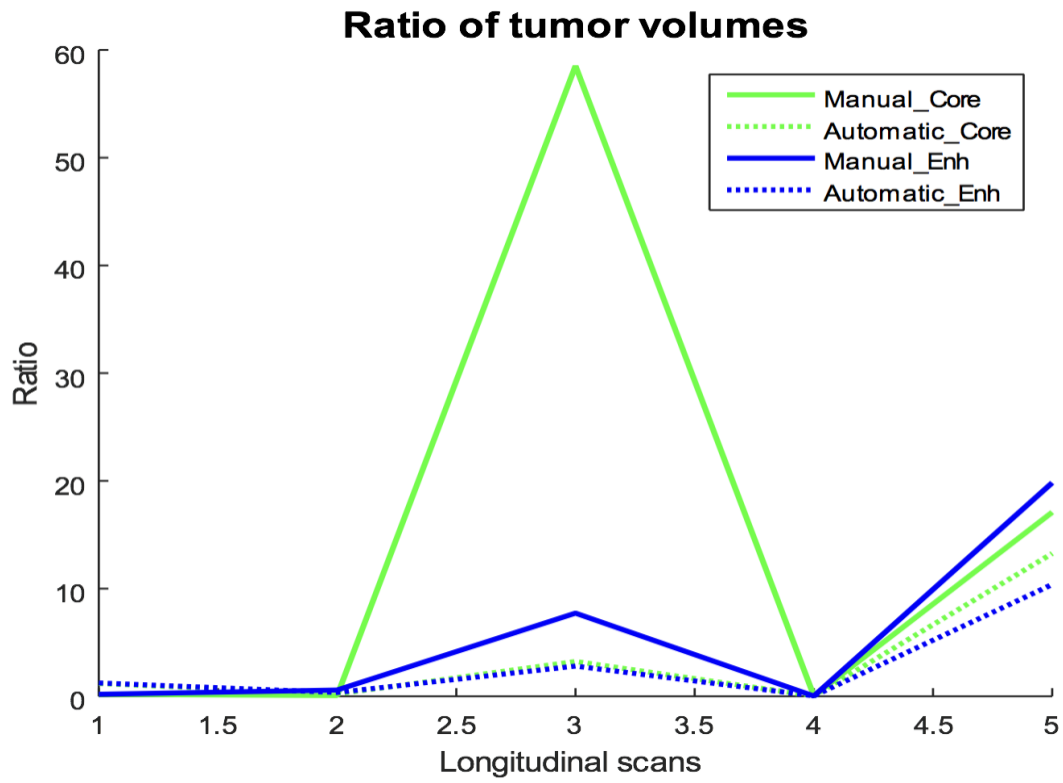
#### 4.5 TRACKING THE CHANGE OF TUMOR VOLUME

In order to assess the tumor volume change in longitudinal images, the method quantifies the changes ( $V^{t'}/V^t$ ) of both core and active part of the tumor. In this analysis, images of 13 patients those have more than 3 follow-up scans are used. However, as the data size is too low to train any machine learning algorithm, tumor volume change is assessed with the visual observation. Figure 30 shows plots of the volumetric changes for four example patients.

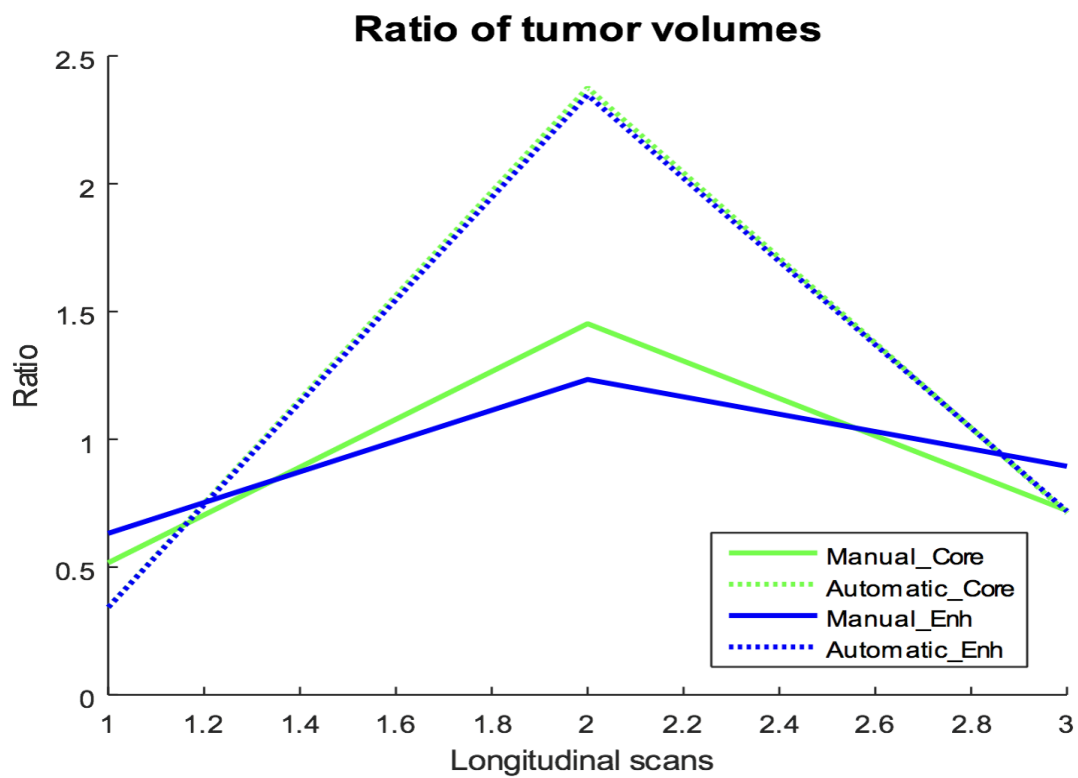




**Figure 30:** Plots of the volumetric changes in the longitudinal images. a) Stable after resection, b) decreasing after resection, c) progressing after sudden change, and d) stable.



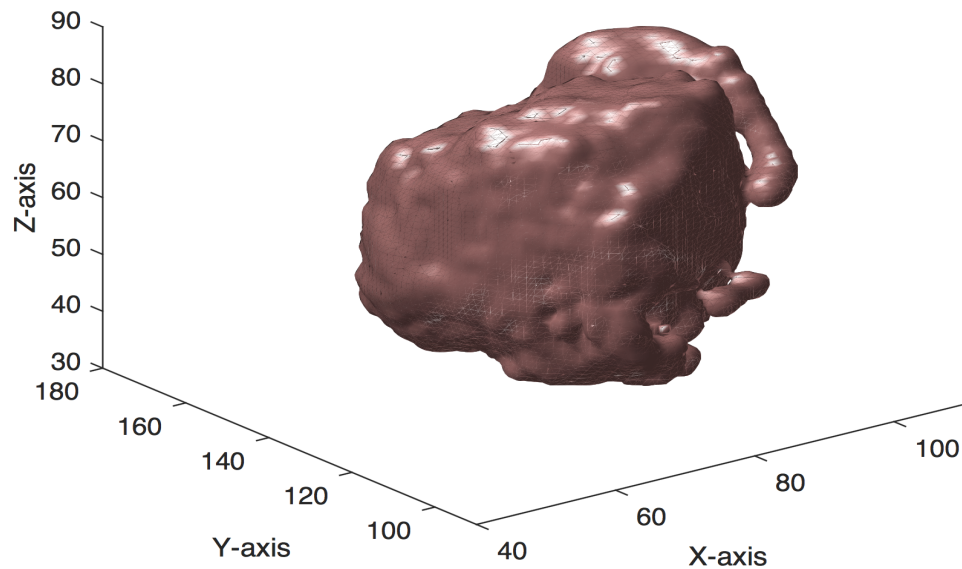
(c) Case-3



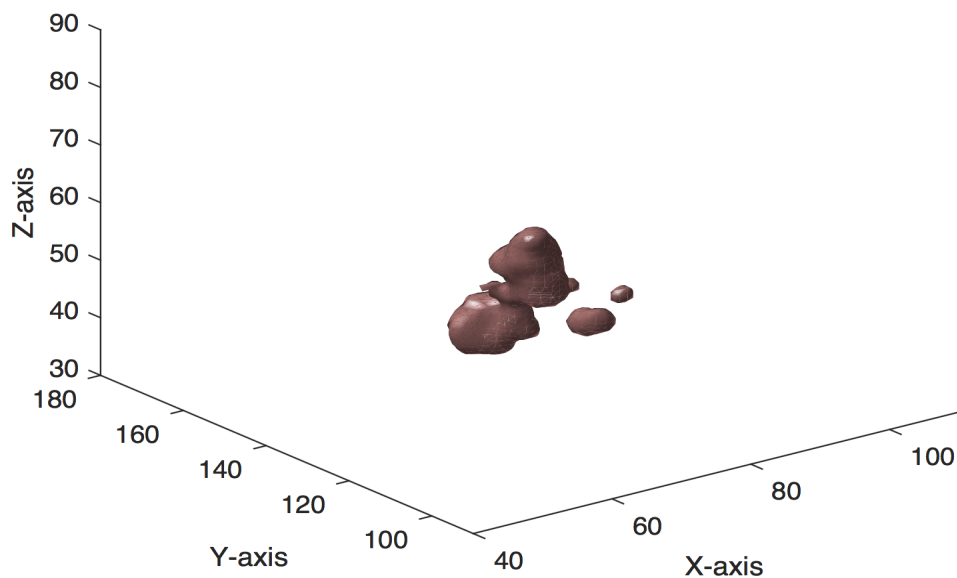
(d) Case-4

Figure 30. (continued)

To validate the proposed quantification in tracking the tumor volume using the volumetric plots, the original tumor volumes are also observed in longitudinal images (Figure 31) for a randomly selected patient, in this regard (*Case-3*) in Figure 30. The original tumor volumes of this particular patient indicates that after resection the tumor re-appeared later at time,  $Tp_6$ . Similar conclusion can be drawn from the volumetric plots and thus confirms the findings of our proposed volumetric quantification in tracking the change of tumor volume.



(a) Tumor volume at time,  $Tp_1$



(b) Tumor volume at time,  $Tp_2$

**Figure 31:** Original tumor volumes in longitudinal images of a patient. Confirmation of the possibility for volumetric ratio based tracking the change of tumor volume. The longitudinal images are shown for the patient that corresponds to *Case-3* in Figure 30.

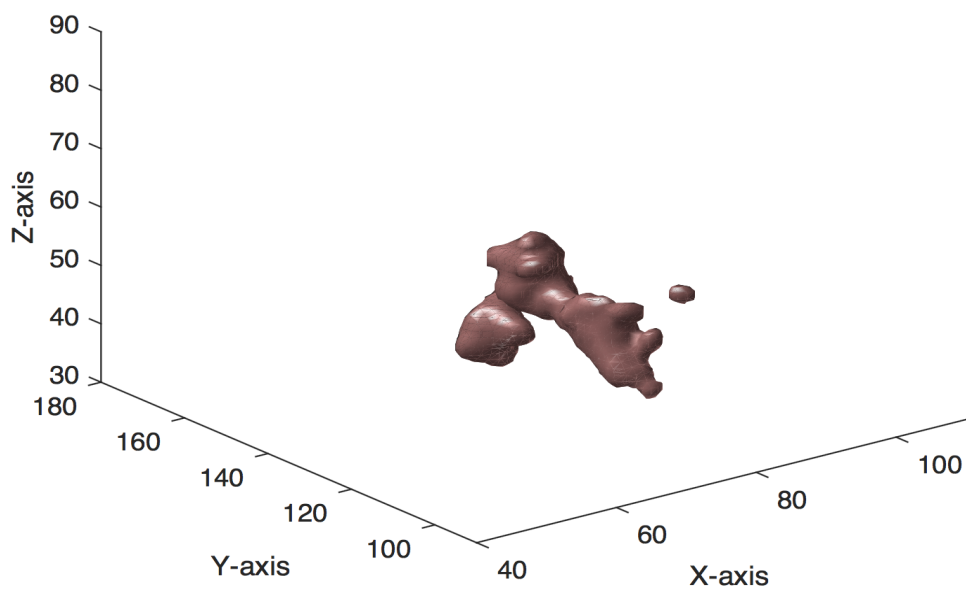
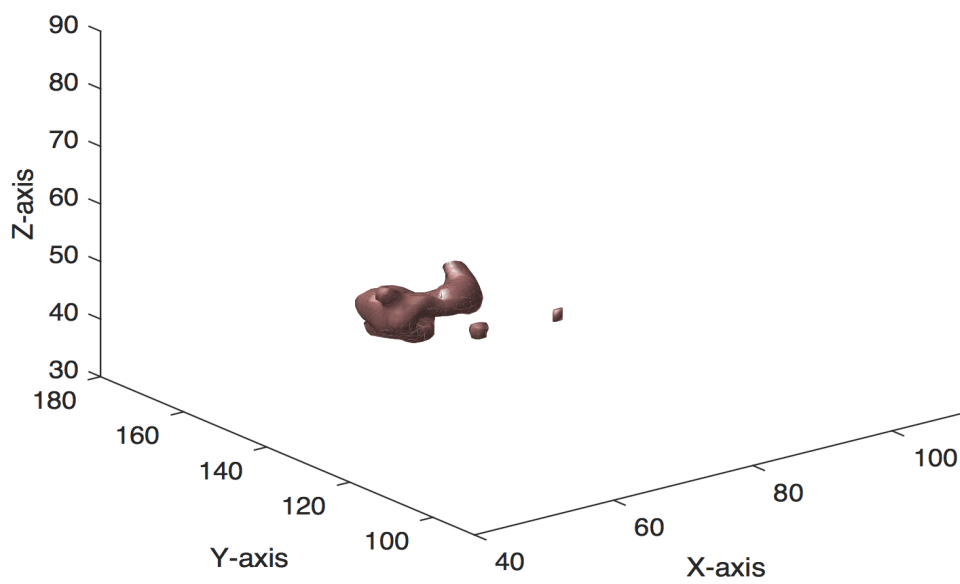
(c) Tumor volume at time,  $T_{p_3}$ (d) Tumor volume at time,  $T_{p_4}$ 

Figure 31. (continued)

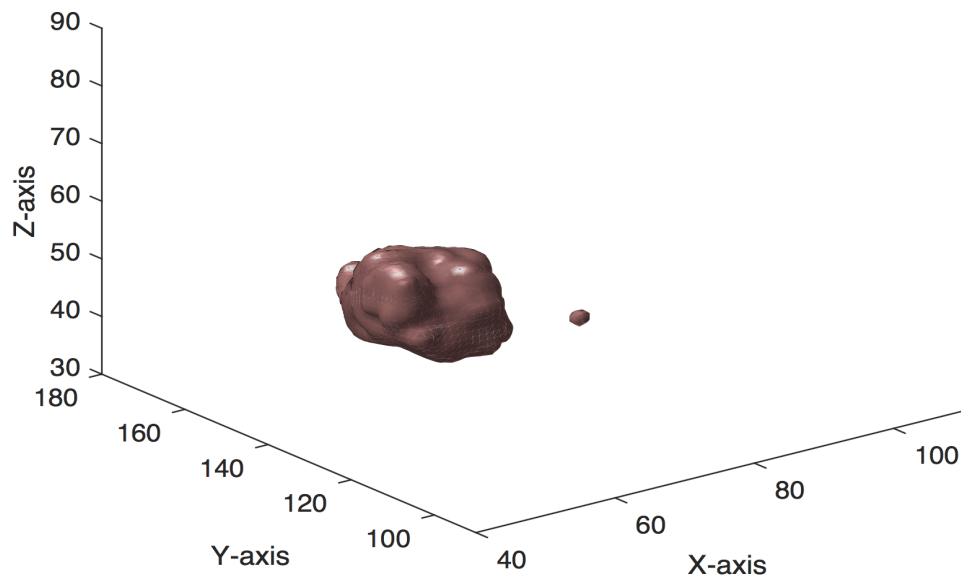
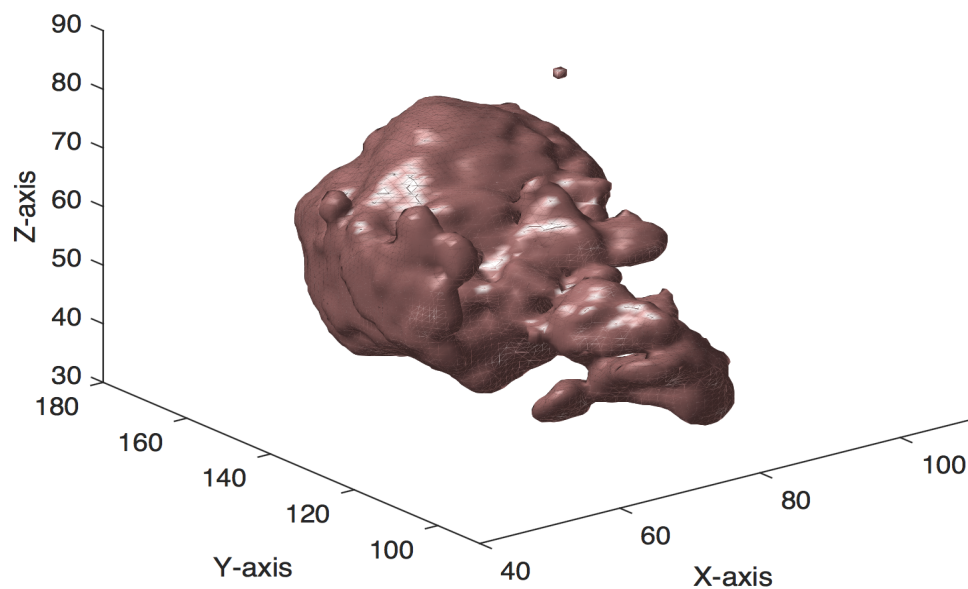
(e) Tumor volume at time,  $T_{p_5}$ (f) Tumor volume at time,  $T_{p_6}$ 

Figure 31. (continued)

## 4.6 DISCUSSION

In this work, a BTS method with complete post-processing steps is proposed to reduce the FPs. These FP reduction steps may be used in any tissue segmentation method that offers high sensitivity with moderate FP. The results are shown in Table 8 and Figure 26, 27, and 28 suggest that the proposed 3D texture features are effective in reducing FPs and thus improve the segmentation result. Scores in Table 8 shows that the method improves the overall tissue segmentation performance for all three defined tumor categories. The volumetric ratios shown in Figure 30 confirms the quantification of tracking the change of tumor volume using the proposed

method, which in turn evaluates the consistency of our proposed method in segmenting brain tumors in longitudinal images. In future, the overall performance can be further improved by training the BTS with more training data. Also, the future study plans to conduct several experiments; i) devise the original BTS method to consider inputs from both time scans ( $I_t, I_{t'}$ ), where  $I$  stands for input features, ii) generalize the proposed method so that single time scan data can also be tested by simply dropping the temporal classifier, and iii) apply the method with small size lesion.

## CHAPTER 5

# TEXTURE-BASED RADIOMICS FOR GLIOMA GRADING AND VALIDATION USING HISTOPATHOLOGY IMAGES

### 5.1 CHAPTER OVERVIEW

This work proposes novel non-invasive glioma grading using structural MR images that may be useful before an invasive biopsy is recommended. The proposed method suggests that grading of glioma tumors is possible using novel radiomic texture features in MRI. Tumor texture is characterized by employing a combination of DT analysis, MF DFA, and mBm. The efficacy of the proposed method is investigated using MRIs of 235 patients collected from two separate multi-center datasets. The proposed method is evaluated in two grading tasks such as HG versus LG glioma, and GBM versus LG glioma. In the first task, the evaluation of the method is obtained using MRIs from 168 HG and LG glioma patients in 2015 Brain Tumor Segmentation (BRATS) challenge. The results show that the mean area under the receiver operating characteristic curve (AUC) is 80% for HG versus LG tumor classification. In the second task, the proposed non-invasive tumor grading performance is evaluated using MRIs from 67 GBM and LG glioma patients obtained from NIH TCIA repository [75]. For validation, the method's performance is compared with an invasive grading in DP images for the same 67 patients obtained from NIH TCGA repository [76]. The AUCs are found to be 88% and 90% for classifying tumor grades using MR and DP images, respectively. The overall MR grading performance in both tasks confirms the efficacy of the proposed non-invasive radiomics method for glioma grading.

### 5.2 NON-INVASIVE GLIOMA GRADING METHOD

This section discusses the proposed non-invasive glioma grading using structural MR images. The overall flow diagram of the proposed method is shown in Figure 32. The method uses three commonly available MR modalities: T1c, T2, and Flair. Following standard MR image pre-processing, an automatic segmentation (BTS) method is employed to segment the tumors. The proposed features are then extracted from MR image slices of the segmented tumor region.

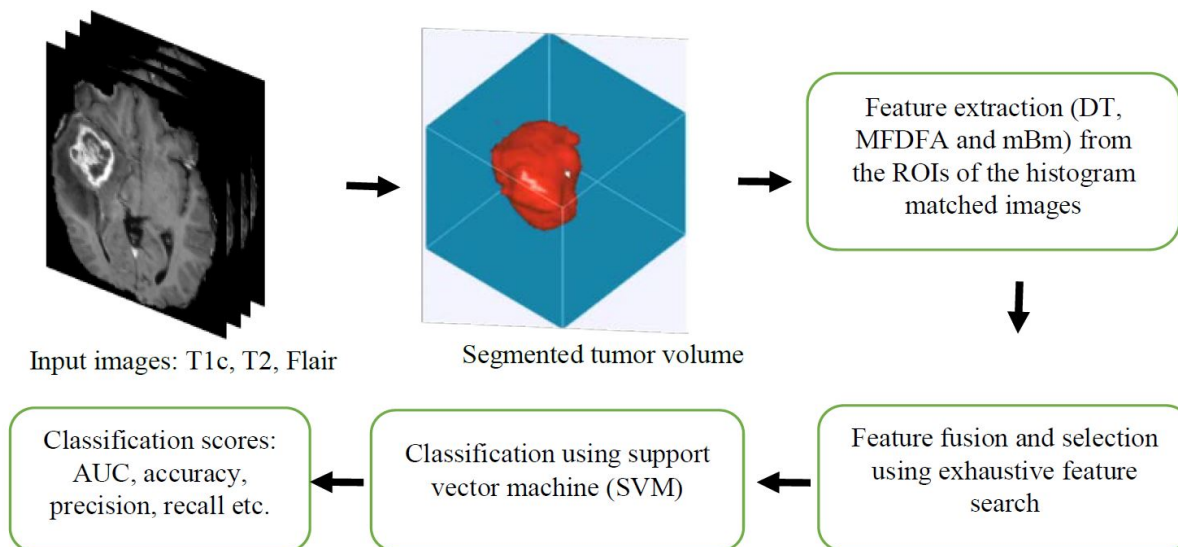


**Figure 32:** Overall flow diagram of the proposed method for automatic segmentation and classification of tumor grades in MR images.

A detailed description of each step in Figure 32 is given below.

### 5.2.1 AUTOMATIC TUMOR SEGMENTATION

In the first step, the method employs a texture feature-based automatic brain tumor segmentation (BTS) technique [7] which has demonstrated excellent performance in multiple global tissue segmentation challenges (e.g., ranked 3<sup>rd</sup> in BRATS-2013 [61], ranked 4<sup>th</sup> in both BRATS-2014 [62] and ISLES-2015 [3] competitions, respectively). In this work, the proposed method performs a multiclass (necrosis, edema, active tumor and non-tumor) abnormal tissue segmentation task. The segmented 3D tumor volume is considered as the region of interest (ROI) for extracting the proposed grading features.

### 5.2.2 FEATURE EXTRACTION FOR TUMOR GRADING

Several texture features including mBm, novel MFDFA, and 3D dynamic texture features are extracted from the 3D tumor region. The underlying mathematical model and algorithm for extracting these texture features are described below.



### 5.2.2.1 MULTI-RESOLUTION MBM TEXTURE FEATURE EXTRACTION

The multi-resolution fractal features are derived from the analysis of mBm process and have been effectively used in detection and segmentation of brain lesions [3][61][62]. However, in this grading task, the algorithm is customized to take the whole image instead of a sub-image as input for the classification task. Figure 33 represents algorithm to extract texture feature using the mBm process for the classification.

---

```

Input: image, wavelet, level
// image : N × MMRI image
Output: MultiFD
a. for a in 1 to level do
  | i. compute the wavelet coefficients at scale a as shown in (2)
  | ii. compute  $E\{|W_z(\vec{b}, a)|^2\}$ 
end
b. Compute  $H(\vec{u})$  using  $\log(E\{|W_z(\vec{b}, a)|^2\})$ 
   versus  $\log(a)$  as shown in (3)
c. Compute  $FD = 2 + 1 - H(\vec{u})$ 
return FD

```

---

**Figure 33:** Modified algorithm for texture extraction to classify brain gliomas using mBm process.

### 5.2.2.2 MFDFA FEATURE EXTRACTION

The MFDFA is a multi-fractal process that is used to investigate the long-range dependency in a random sequence or image. The method is successfully used in the time-series analysis [77], in predicting gold price fluctuations [78] and in detecting micro-calcification in [19] mammogram images. MFDFA is the multi-fractal process of the detrended fluctuation analysis (DFA).

For a given sub-image of size  $s$ -by- $s$ , the DFA is defined by the equation below,

$$F(v, w, s) = \sqrt{\frac{1}{s^2} \sum_{k1}^s \sum_{k2}^s (U_{v,w}(i, j) - \tilde{U}_{v,w}(i, j))^2}, \quad (12)$$

where,  $F(v, u, w)$  is the detrended fluctuation of the sub-image that is indexed by  $(v, w)$  of the original image.  $U_{v,w}(i, j)$  denotes the cumulative sum and  $\tilde{U}_{v,w}(i, j)$  is the fitted surface of the cumulative sum and  $1 \leq (i, j) \leq s$ . The  $q^{th}$  order fluctuation of each sub-image is given by Equation (13) and is determined for values of  $q = (-6, -4, -2, 2, 4, 6)$ . According to the L Hospital's rule, Eq. (14) is used for  $q = 0$ . The sum of all fluctuations is averaged over total

number of sub-images as follows

$$F_q(s) = \frac{1}{T} \left\{ \sum_y \sum_x [F(v, w, s)]^q \right\}^{\frac{1}{q}} \quad (13)$$

and,

$$F_0(s) = \exp \left\{ \frac{1}{T} \sum_y \sum_x \ln [F(v, w, s)]^q \right\} \quad (14)$$

where  $T$  is the total number of sub-images. The Hurst index,  $h(q)$  is given by the slope of the log-log plot of  $F_q(s)$  versus  $s$  in Eq. (15). An image has self-similarity, if the log-log plot of  $F_q(s)$  versus  $s$  indicates the power law scaling with a linear relation.

$$F_q(s) \sim s^{h(q)} \quad (15)$$

The dependence of  $\tau(q)$  on the scaling exponents  $q$  and  $h(q)$  in Eq. (16) is the necessary condition for multi-fractal images.

$$\tau(q) = q \times h(q) - E; \quad (16)$$

where,  $E = 2$ , is the Euclidean dimension of 2-D image. The Hölder exponent,  $\alpha = \hat{\tau}(q)$ , is used to find the singularity spectrum, and  $f(\alpha)$  is defined as the Hölder function as below,

$$f(\alpha) = q\alpha - \tau(q). \quad (17)$$

In this work, the MFDFA process measures the fluctuations (roughness of the surface) in an image at multiple ranges (scales) to estimate the Hurst index at different resolutions. Finally, the maximum and minimum values of the Hurst index,  $h(q)$ , maximum of Hölder function  $f(\alpha)$  and the corresponding  $\alpha$  values are used as the features following the above analysis. Figure 34 and 35 show the algorithm for feature extraction and the selected features within the corresponding plots, respectively.

---

**Input:**  $image, scale(s), order(q)$   
**Output:**  $max\_H(q), min\_H(q), max\_F(\alpha), \alpha_m$   
**for each value of  $s$  do**  
  i. calculate  $U_{v,w}(i, j)$  and  $\tilde{U}_{v,w}(i, j)$   
  ii. calculate  $F(u, w, s)$  using (12)  
  **for each  $q$  do**  
    | calculate  $F_q(s)$  and  $F_0(s)$  as in (13) and (14)  
  **end**  
**end**  
Find  $h(q)$  from the log-log plot of  $F_q(s)$  versus  $s$   
Calculate  $\tau(q)$  using equation (16)  
Plot  $f(\alpha)$  w.r.t  $\alpha$   
Find maximum of  $f(\alpha)$  and corresponding  $\alpha_m$   
**return**  $max\_H(q), min\_H(q), max\_F(\alpha), \alpha_m$

---

**Figure 34:** Algorithm of feature extraction using Multifractal detrended fluctuation analysis(MFDFA).

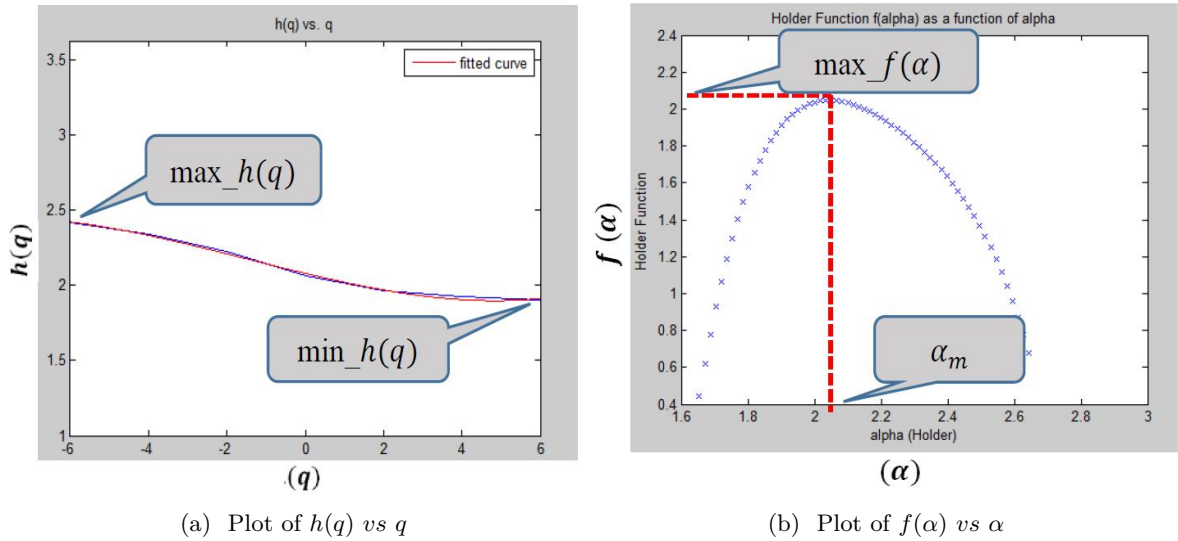


**Figure 35:** Plots of significant features for grading brain gliomas in MR images using MFDFA.

### 5.2.2.3 DYNAMIC TEXTURE FEATURE EXTRACTION

The dynamic texture, also known as the temporal texture, can be viewed as a continuously varying stream of images, which has resemblance with a fountain with continuous gushing water, a flickering fire, and a chimney with slowly puffing smoke. Recently, the analysis and synthesis

of dynamic texture have become active areas of research in computer vision and computer graphics and are gradually penetrating in the field of dynamic texture editing [79], pattern recognition [80], segmentation [18] and image registration [81]. In the proposed model for tumor grading, it is considered that the MR sequence of images in the tumor volume or ROI inherits continuously varying images and thus can be defined as a dynamic texture. Since tumors of different grade vary in their aggressiveness, the rate of continuously varying characteristics of MR image sequences may exhibit different values for different tumor grades. We adopt the linear dynamic system (LDS) method [82][83] by using state-space equations where the parameters of state equations are used as the dynamic texture descriptor. Figure 36 shows the DT analysis method adopting an open loop LDS system used in [82][83].

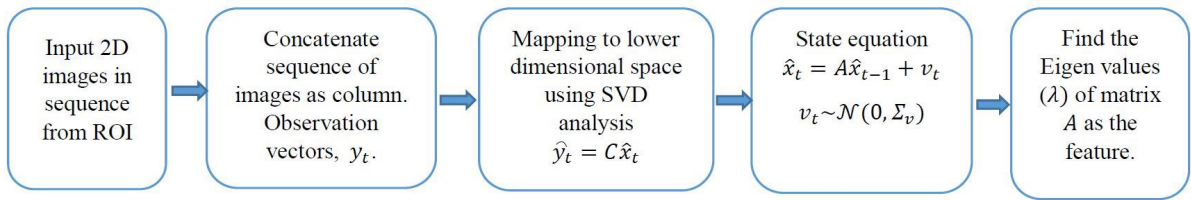


**Figure 36:** Framework for dynamic texture analysis using linear dynamic system.

To illustrate the DT analysis method, the mean value of the sequence of input images  $\{I_t\}_{t=1}^N$  are subtracted and concatenated to column vectors as observation vectors,  $y_t$ . The SVD analysis is performed to map the estimated observation vectors  $\{\hat{y}_t\}_{t=1}^N$  to the truncated hidden states,  $\{\hat{x}_t\}_{t=1}^{N/2}$  following Eq. (11). These truncated hidden states are actually the most significant principal components of the observation vectors. This study heuristically determined that first half of the most significant principal components yields promising results, so the last half columns of the original hidden states,  $x_t$  are truncated to obtain the estimated hidden state,  $\hat{x}_t$ .

$$\begin{aligned}
 [U, S, V] &= \text{svd}(y_t - \bar{y}_t); \\
 x_t &= S \times V'; \\
 \hat{x}_t &\leftarrow x_t; \\
 C &= U;
 \end{aligned} \tag{18}$$

where the observation matrix  $y_t$  is of size  $m \times n$  and  $U$ ,  $S$ ,  $V$  are of size  $m \times n$ ,  $m \times m$ , and  $n \times n$ , respectively. Since principal components can be ranked in descending order, a dimensionality reduction is performed by discarding some columns corresponding to the least important components and, hence the mapping function is given by  $\hat{y}_t = C \hat{x}_t$ . These reduced hidden states are used to fit a linear dynamic system and identify the parameters of the system

using Eq. (17). The state equation is described as below:

$$\hat{x}_{t_i} = A\hat{x}_{t_{i-1}} + v_t; \text{ where } v_t \sim N(0, \sigma_v) \quad (19)$$

Eq. (18) suggests that a hidden vector corresponding to the hidden states can be mapped linearly to its next hidden vector if the system is a dynamic process. The state parameter,  $A$ , is found through the following way,

$$A = \hat{x}_{t_i} \times \hat{x}_{t_{i-1}}. \quad (20)$$

The Eigen values  $\lambda$  of matrix  $A$  describes the pole location of the dynamic system and, hence, gives an estimate about the system stability. The pole locations of  $\lambda$  values are the discriminating features for tumor grading. Figure 37 shows the algorithm to extract DT features using the open loop LDS.

---

**Input:** 2-D *image sequences*  
**Output:**  $\lambda_{max}$   
 Find  $y_t$  from the input images  
 Perform  $y_t \leftarrow y_t - \tilde{y}_t$   
 Perform SVD analysis as in (18)  
 $\hat{y}_t = C\hat{x}_t$ ;  
 Set the LDS as in (19)  
 Find the state parameter,  $A$  as in (20)  
 Find the Eigen values  $\lambda$  of  $A$   
 Sort the  $\lambda$ s and find the  $\lambda_{max}$   
**return**  $\lambda_{max}$

---

**Figure 37:** Algorithm for dynamic texture analysis to extract useful feature.

### 5.2.3 FEATURE SELECTION AND CLASSIFICATION

A feature selection step is proposed to achieve two goals. First, the performance of tumor grading classification is improved by eliminating the effect of curse-of-dimensionality. Second, an optimal set of features is obtained that yield the most accurate classification of tumor grading. Standard variable selection algorithms such as sequential feature search, yield a suboptimal solution, whereas an exhaustive search algorithm guarantees to find the optimal features required for a classification task [84]. The machine learning pipeline for exhaustive feature search in this work is shown in Figure 38.

---

```

Input:  $n$  # of features
Output:  $mean\_AUC, std\_AUC$  of best feature combination
for  $r = 1, 2, 3 \dots n$  do
  Generate all combinations  $t = nCr$ 
  for Each combination of  $t$  do
    i. Evaluate  $k$  fold cross-validation
    ii. Measure the mean and std. of AUC
  end
  Rank feature combinations based of mean AUC
  Return mean and std of AUC of the top rank
end
return  $mean\_AUC, std\_AUC$ 

```

---

**Figure 38:** Algorithm for exhaustive feature search.

The exhaustive feature search algorithm evaluates all possible combinations of features, which is often prohibitive due to heavy computational cost. However, the exhaustive search is computationally feasible with the sample size and variable dimension (14-16) and it is worth learning the optimal features than presenting sub-optimal results using other feature selection algorithms. All possible combinations of features are evaluated using the linear support vector machine (linear-SVM) classifier model. The linear SVM is not only faster and efficient, it does not suffer from overfitting like other non-linear classifier models due to undersampling of the data [85]. The linear-SVM model trains the linear coefficients of features that simultaneously provide a parametric formulation of the decision boundary and importance of features [86]. The mean AUC, obtained over ten-fold cross-validation using linear-SVM model, is used to evaluate the classification performance of each combination of features. The goal of the exhaustive feature search is to find the optimal combination of features that yield the most accurate classification of the tumor grading.

### 5.3 AUTOMATIC GRADING USING DIGITAL PATHOLOGY IMAGES

The method outlined in [87] is used for automatic glioma grading using digital pathology images. However, instead of using a single image per patient as used in [87], this study uses the ROI outlined by a pathologist from all the available images of that patient. In the first step, an automatic cell nuclei segmentation is performed through color inhomogeneity correction, optical density estimation, color deconvolution for hematoxylin stain, contrast enhancement, and hysteresis thresholding. The geometric feature including area, major axis length and perimeter are subsequently extracted from each nucleus. These micro-anatomical features are important to distinguish different glioma grades.

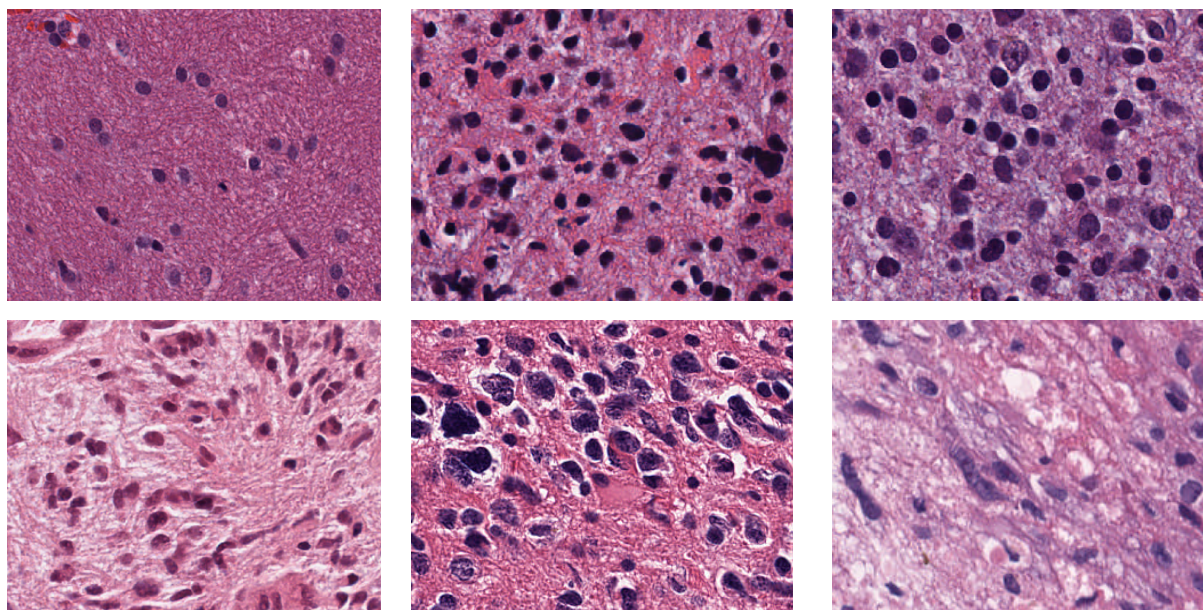
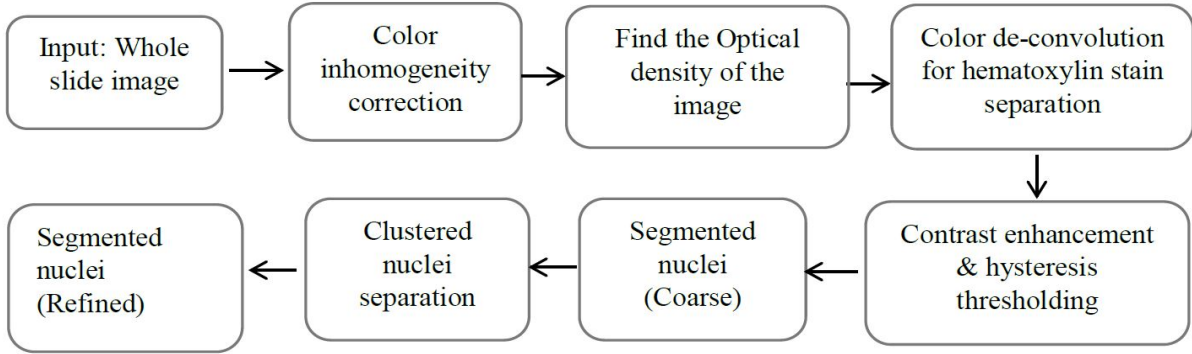


**Figure 39:** The significant presence of elongated nuclei in GBM (bottom row) in compared to LG (top row). This difference sets one of the grading characteristics between the two types of gliomas.

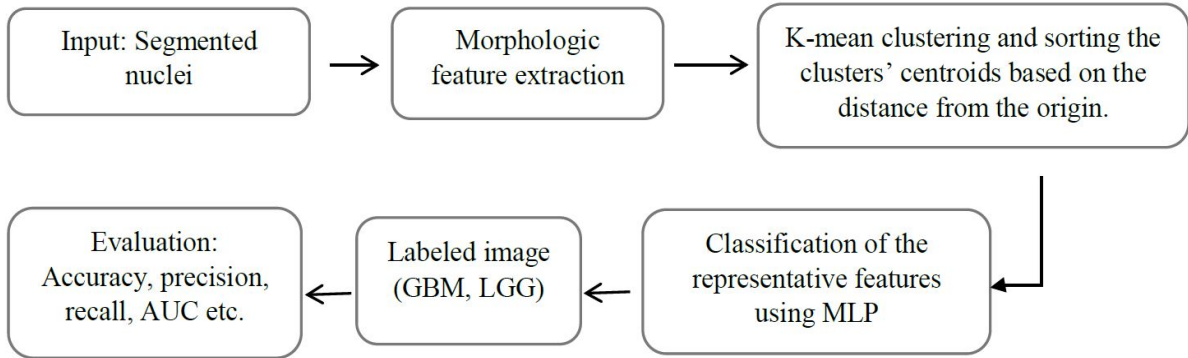
The nuclei in LG are predominantly circular with smaller morphologic characteristics, whereas nuclei in GBM are mostly elongated with irregular size. The prevalence of these irregular shaped nuclei, as shown in Figure 39, are different in GBM (WHO grade IV) and LG (WHO grade I & II) images and can be used as one of the grading characteristics. It is also noticed that similar grading criteria can be applied for HG (WHO grade III & IV) and LG classification. Intuitively, classifying HG vs LG is more challenging than GBM vs LG as grade-III (HG) and grade-II (LG) often show quite similarity in images. In this work, all the features are collected from each nucleus for individual patients and clustered them into five classes using the k-means algorithm. The cluster centroids are sorted according to the Euclidean distance from the origin and are used in the subsequent classification step. It is intuitive that some cluster centroids are similar in both GBM and LG images while the rest are dissimilar and become the basis of classification.

### 5.3.1 METHODOLOGY

The proposed method consists of two main steps. In the first step, the nuclei are segmented from the whole tissue slide images. In the second step, feature extraction and classification are performed. The overall flow diagram of the proposed method is shown in Figure 40.



(a) Simplified flow diagram of nuclei segmentation in Digital Pathology images.



(b) Classification/grading pipeline using nuclei morphology feature.

**Figure 40:** The overall flow diagram for grading brain gliomas in digital pathology images.

Brief descriptions for each step in the above flow diagram are given below.

### 5.3.1.1 DP IMAGE PRE-PROCESSING

All the images are stained with hematoxylin and eosin. As the images are scanned with multi-resolution varies from 20X to 40X, we sample all images to 20X with bi-cubic interpolation. Automatic contrast enhancement is applied to bring all the images with uniform color contrast.

### 5.3.1.2 FINDING THE OPTICAL DENSITY IMAGE

As the image intensities are of 8-bit depth, the maximum intensity,  $I_{max}$  is 256. The light absorbance of each pixel can be found by Beer-Lambert's law [88], where,  $I$  is the image intensity.

$$A = -\log_{10}\left(\frac{I}{I_{max}}\right) \quad (21)$$



### 5.3.1.3 COLOR DE-CONVOLUTION

Since the optical density is proportionate to the stain's concentration, color de-convolution process is applied on the optical density image. In this implementation the de-convolution matrix,  $M$  is defined as

$$M = \begin{bmatrix} m_{11} & m_{12} & m_{13} \\ m_{21} & m_{22} & m_{23} \\ m_{31} & m_{32} & m_{33} \end{bmatrix} = \begin{bmatrix} 0.550 & 0.398 & 0.754 \\ 0.758 & 0.634 & 0.077 \\ 0.351 & 0.600 & 0.652 \end{bmatrix} \quad (22)$$

where each row in matrix  $M$  indicates a specific stain and the columns represent the optical densities for the red, green and blue channels respectively. The color de-convolution is then performed with the following equation.

$$\hat{C} = M^{-1}Y \quad (23)$$

where  $Y$  denotes the optical density vector,  $\hat{C}$  is the de-convoluted vector. The hematoxylin stain is the first channel of the de-convoluted image.

### 5.3.1.4 HYSTERESIS THRESHOLDING

A contrast enhancement is done before the hysteresis thresholding. In this step, seeds are defined with an upper threshold and connected component by the lower threshold. The threshold values are in between 0 to 1. Cell nuclei are the connected component at the seed regions.

### 5.3.1.5 NUCLEI SEGMENTATION

The object pixels are removed at the concave boundary to separate the clustered nuclei [70]. Finally, the contour of the segmented nuclei is smoothed with linear interpolation of the boundary. Figure 41 shows step-wise example images for nuclei segmentation.

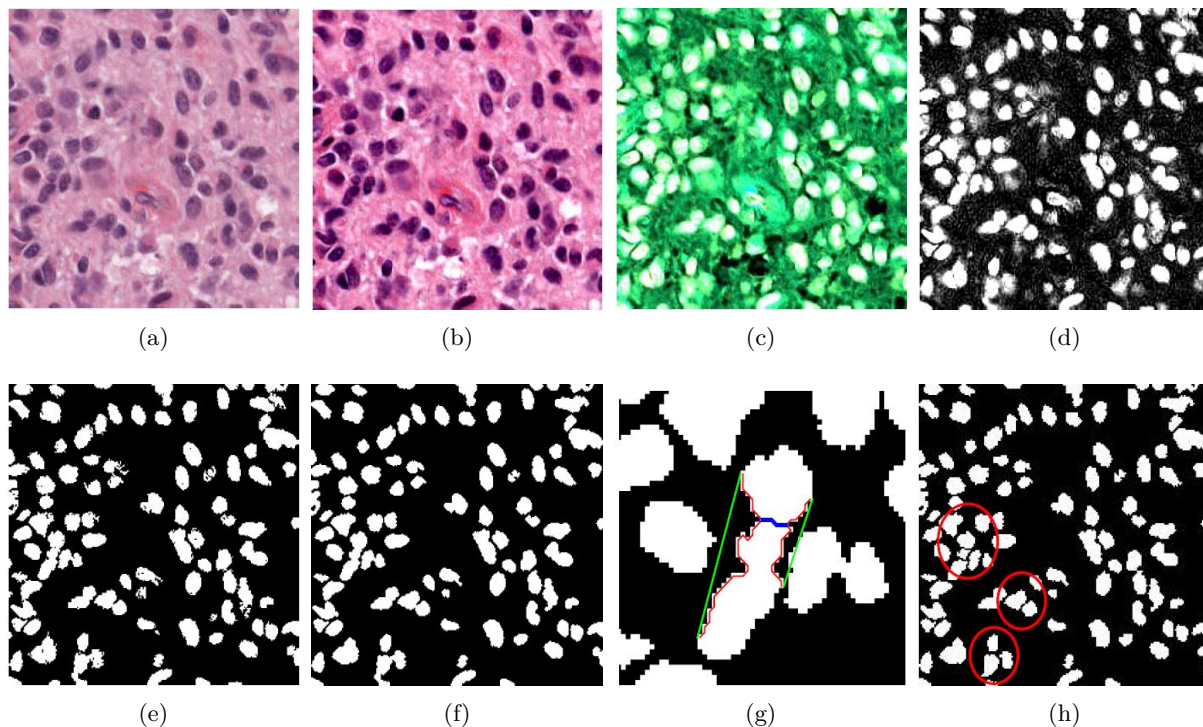


**Figure 41:** Example images of step by step nuclei segmentation in Digital Pathology images. (a) Original image, (b) color normalized image, (c) Optical density image, (d) density of hematoxylin component, (e) hysteresis thresholding, (f) boundary smoothing of segmented nuclei (g) illustration of clustered nuclei separation; green (convex hull boundary), red (concave boundary), blue (cutting line found in a single iteration), (h) final segmentation, clustered nuclei are separated (marked by a red circle).

### 5.3.1.6 MORPHOLOGICAL FEATURE EXTRACTION AND CLUSTERING

Morphologic features like area, perimeter, and major-axis length are extracted from the segmented nuclei. The above geometric features are clustered into 5 groups using k-mean clustering. Euclidean distances from the origin of the centroids are considered to determine the ascending order of the clusters. The centroids of the ordered clusters are used to characterize that individual image.

## 5.4 EXPERIMENTS AND RESULTS

### 5.4.1 DATA

MR images are collected from two separate multi-center datasets: BRATS-2015 and TCIA for HG/LG and GBM/LG grading respectively. Among these multicenter longitudinal MRI

data, only the first time brain scans are used that results in a total of 235 patients wherein 67 patients are obtained from the TCIA dataset and the remaining 168 patients are obtained from the BRATS-2015 training dataset. Histopathology images are collected from the TCGA digital pathology database. Since MR images in BRATS dataset are already skull-stripped and co-registered, we perform skull stripping, resampling and resizing only on the TCIA dataset. The inhomogeneity in MR intensity is corrected through channel-wise histogram matching with the images of a randomly selected patient as the reference. In this study, three MR modalities: T1c, T2 and Flair images are used as they are commonly available in both datasets. Finally, additional MRI images from another 30 patients in the BRATS-2013 dataset are used for training the tumor ROI segmentation classifier. The grading labels (HG/LG) for the BRATS-2015 dataset and (GBM/LG) for the TCIA dataset are already provided in these repositories, respectively. These labels are used for training and evaluation of the classifiers in this study.

#### 5.4.2 TUMOR ROI SEGMENTATION IN MRI

For tumor region segmentation, the BTS method is trained with the MRI from 30 patients in BRATS-2013 training dataset and tested on both TCIA and BRATS-2015 datasets. Details about the parameter setting of the random forest classifier for this multiclass segmentation can be found in [7]. Since the core part of the tumor region (necrosis, enhanced and non-enhanced tumor) retains the maximum clinical significance, the core region is considered and the edematous region is disregarded in this study. The bounding box of the tumor core region is considered as the ROI. Figure 42 shows example images of the segmented tumor and corresponding ROI of two slices selected randomly from two patients. Note that the tumor segmentation is done in 3D, however, for visualization purpose only 2D images are shown in Figure 42.

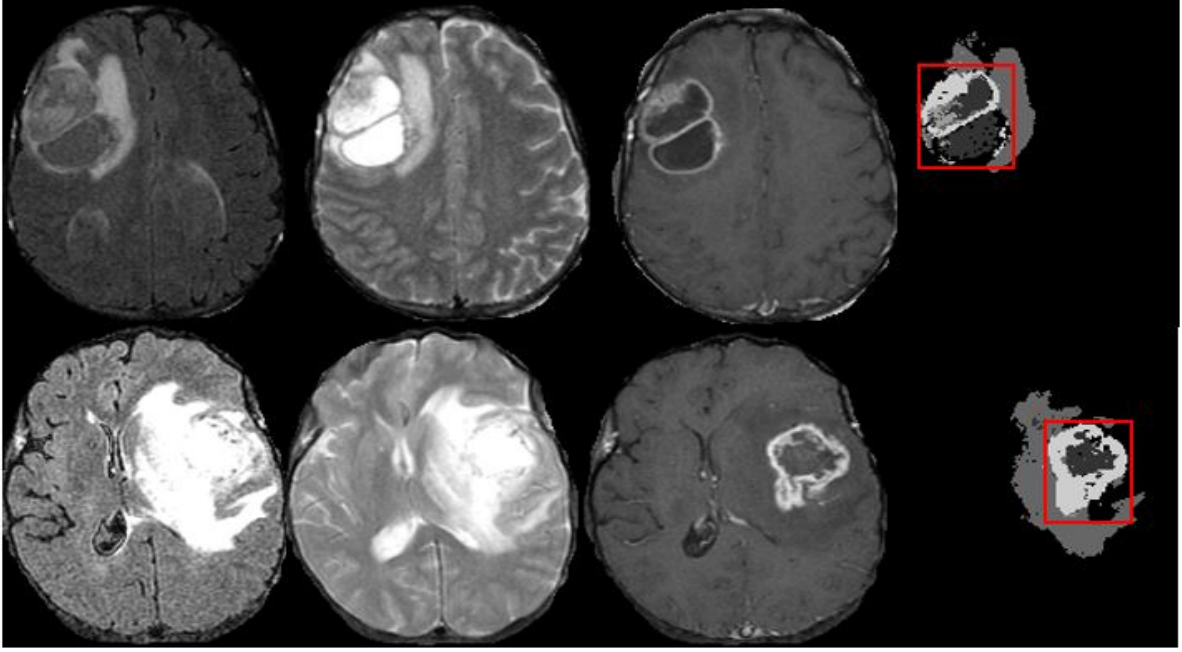


**Figure 42:** Example images of tumor segmentation using BTS with the ROI for dynamic texture analysis. Each row shows the corresponding input MR channels (Flair, T2 and T1c) and the segmented tumor with the ROI indicated in Red.

For dynamic texture feature extraction, the method considers all tumor bearing slices of the ROI in a volume. Therefore, the number of hidden states in Equation (12) is set as the half of total slices of the ROI. As the LDS analyzes system stability using the pole locations, only the absolute of maximum Eigen values from all three modalities are considered and these Eigen values are averaged to obtain the final dynamic feature for the grading task. Figure 43 shows that final features,  $\lambda_{max\_avg}$  of GBM tumors mostly lie outside of the unit circle as GBM tumors usually represent significantly varying textures in MRI slices than that of the LG tumors. Similarly, the MF DFA and mBm features are extracted for each MRI slices in the ROI and only the maximum of the extracted feature values is selected as the final feature for grading. A total of 16 features are extracted from three MRI modalities as follows:  $(1 \times 3)$  mBm,  $(4 \times 3)$  MF DFA, and the DT feature ( $\lambda_{max\_avg}$ ). These features are then taken to the SVM classifier for tumor grading as discussed below.

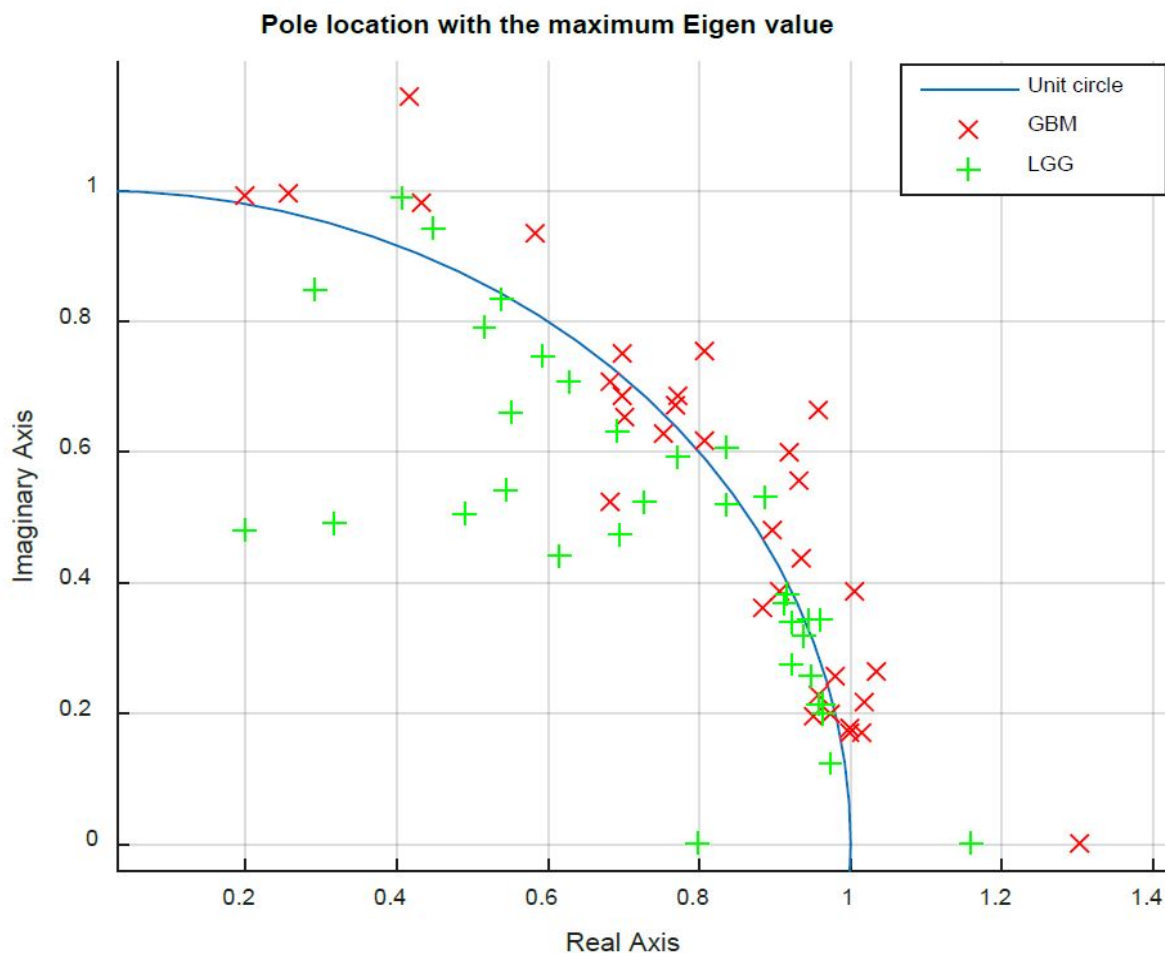


**Figure 43:** Pole locations ( $\lambda_{max\_avg}$ ) of GBM and LG patients. The locations indicates that the rate of signal variation through the MRI slices caused by the different types of tumor are different.

### 5.4.3 MICRO-ANATOMICAL FEATURE EXTRACTION IN DP IMAGES

In this study, another important goal is to validate the proposed MR-based non-invasive tumor grading. Therefore, the study also obtains automatic tumor grading using DP images for the same patients. The proposed method is cross-validated using DP images in TCIA dataset for GBM/LG classification and not in BRATS dataset for GBM/LG classification due to unavailability of the histopathology images in the BRATS. Figure 44 shows example image of the segmented nuclei and the five cluster centroids used as features for tumor grade classification.

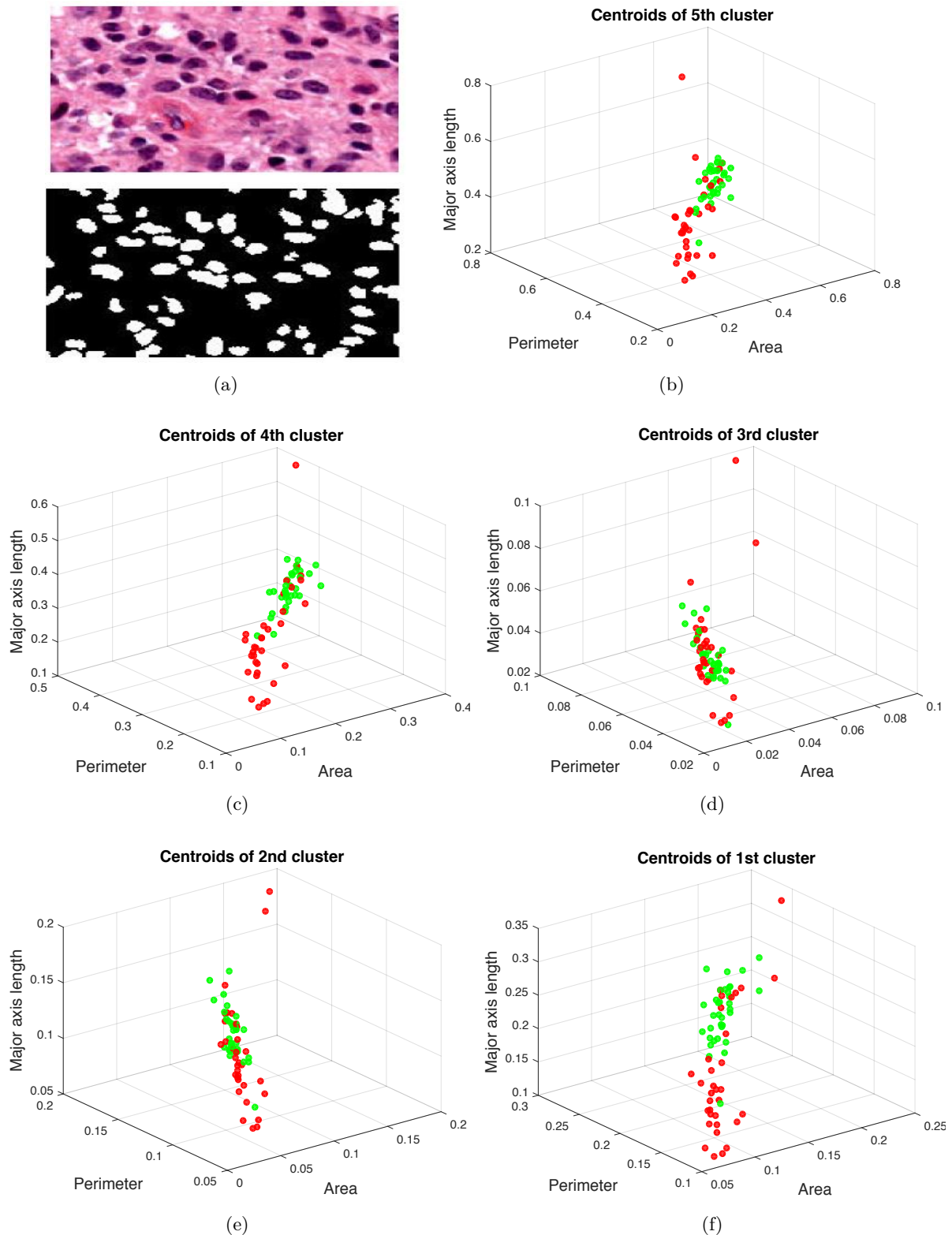


**Figure 44:** K-mean cluster centroids that used as a final features for grading in pathology images. Example images of the segmented nuclei and the five cluster centroids used as features for grading in pathology images [11]. (a) The original pathology image and segmented nuclei, and (b)-(f) five cluster centroids in descending order of the two tumor grades; GBM(red) and LG(green). Although the ROI outlined in the whole slide images are used in this study, only a small part, as shown in (a), is cropped from the original image for better visualization.

#### 5.4.4 SELECTING OPTIMAL SUBSET OF FEATURES

For selecting the optimal subset of the features, a ten-fold cross-validation is proposed to evaluate all feature combinations using the linear-SVM classifier. Experimental results show that for both GBM/LG and HG/LG MR grading a combination of six features that include the DT along with MF DFA and mBm features mostly from the T1c modalities yield the best classification performance. Figure 45(a) shows mean AUC along with the standard deviation versus the different number of feature combinations for GBM/LG grading in MR images while Figure 45(b) shows decision boundary between these two tumor grades defined by two features (mBm of T1c and DT) among the selected six optimal features. The decision boundary also indicates that the extracted radiomic features are effective and easily separable even with a linear SVM kernel.

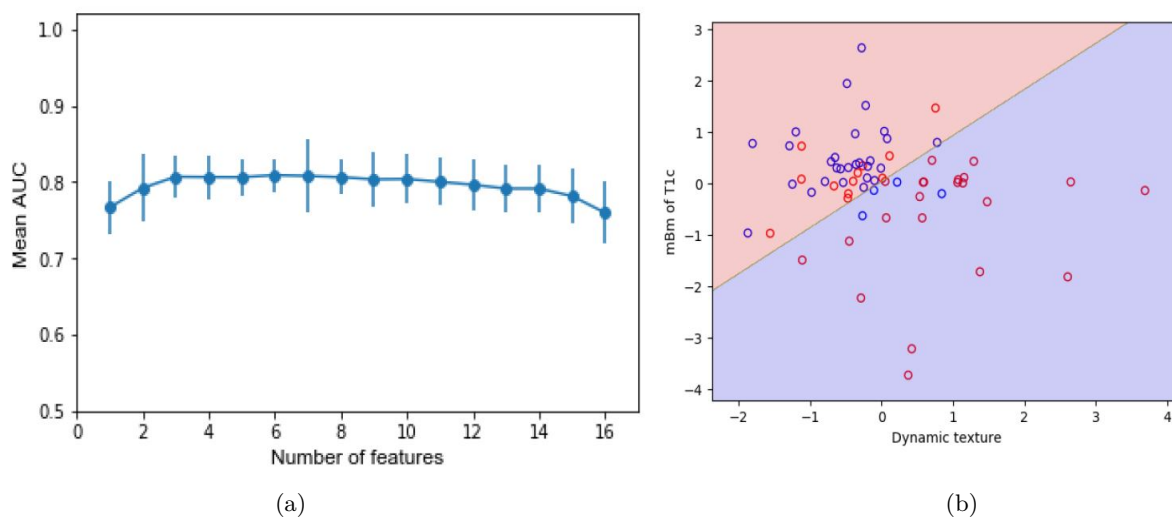


**Figure 45:** Classification performance of the optimal feature combinations using exhaustive feature search for classifying GBM/LG in MR images: a) mean AUC versus feature dimension b) decision boundary between two grades defined by a combination of two optimal features.

The same procedure is repeated for feature selection of DP-based grading of tumors. Figure 46(a) shows that combination of two features offers the highest mean AUC area for the different number of feature combinations. However, the high standard deviation is noticed as for a low sample size, miss-classification of few samples has a big impact on the overall performance. From the combination of optimal features, we observed that perimeter of 1st and area of 5th cluster provides best classification performance, which is also evident from the cluster centroids plots in Figure 44, as these two features in the above-mentioned clusters offer better separation between the grades. Figure 46(b) shows the decision boundary of the two HG/LG grades (classes) in 2D feature space.

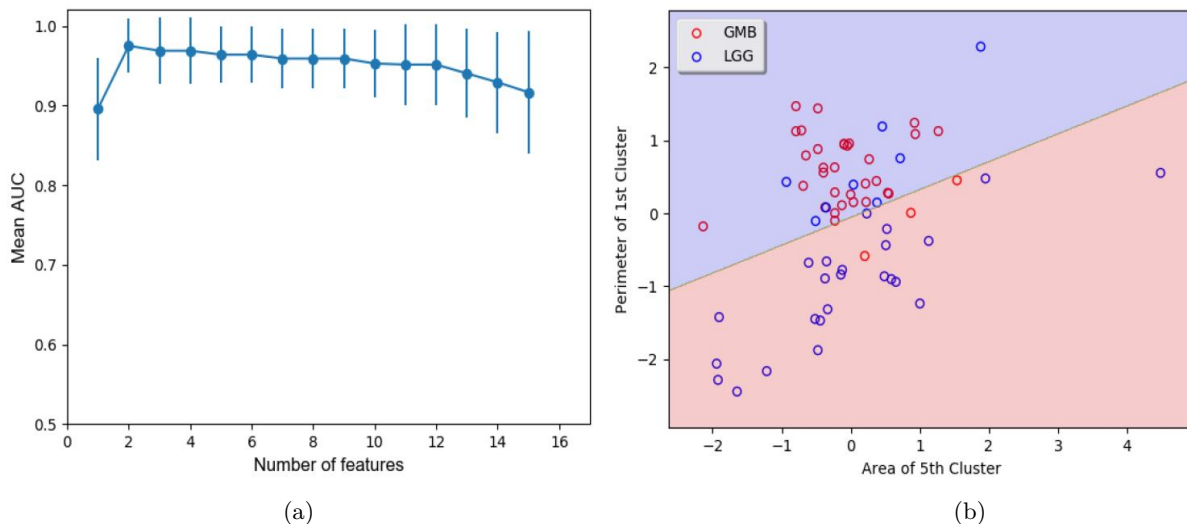


**Figure 46:** Classification performance of the optimal feature combinations using exhaustive feature search for classifying GBM/LG in DP images: a) mean AUC versus feature dimension b) decision boundary between two grades defined by a combination of two optimal features.

#### 5.4.5 HG/LG GRADING USING BRATS IMAGES

Using the selected features in the previous step, the LOO cross-validation offers an average 80% AUC for HG/LG classification. Figure 47 shows the ROC curve obtained from the LOO cross-validation using MR images of 168 patients in BRATS dataset. Quantitative scores such as sensitivity, specificity, F-measure are presented in the first row of Table 9. The quantitative scores in Table 9, shows that the imbalance of the BRATS data may have compromised the overall performance. Moreover, the BRATS MR images are highly re-sampled to yield isotropic MRI (1 mm  $\times$  1mm  $\times$  1mm) and, thus, may severely compromise the quality of extracted texture features.



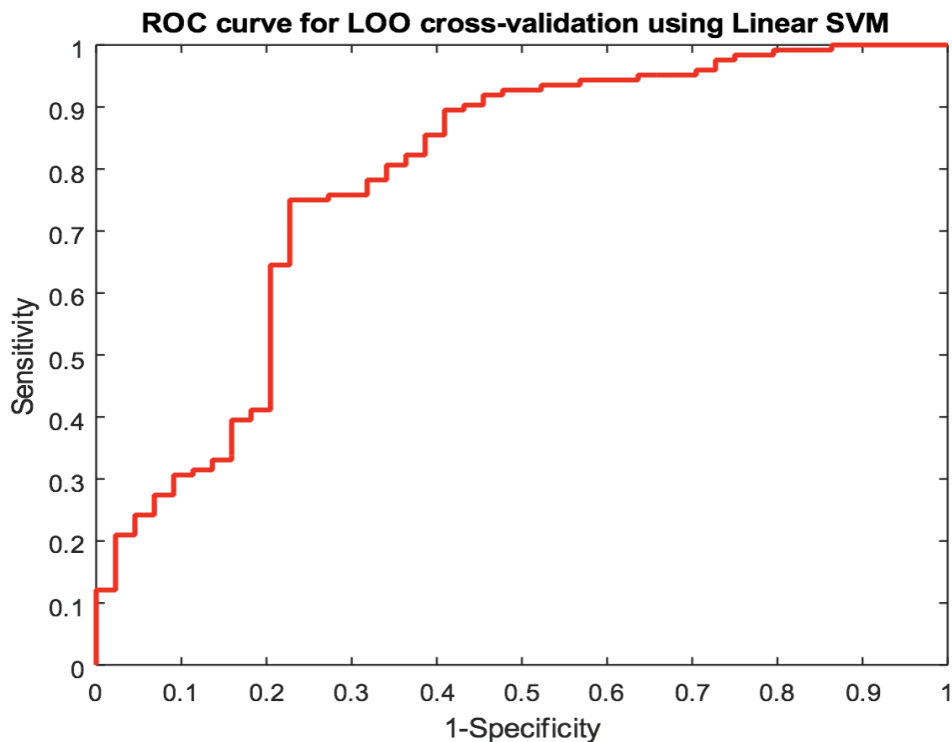


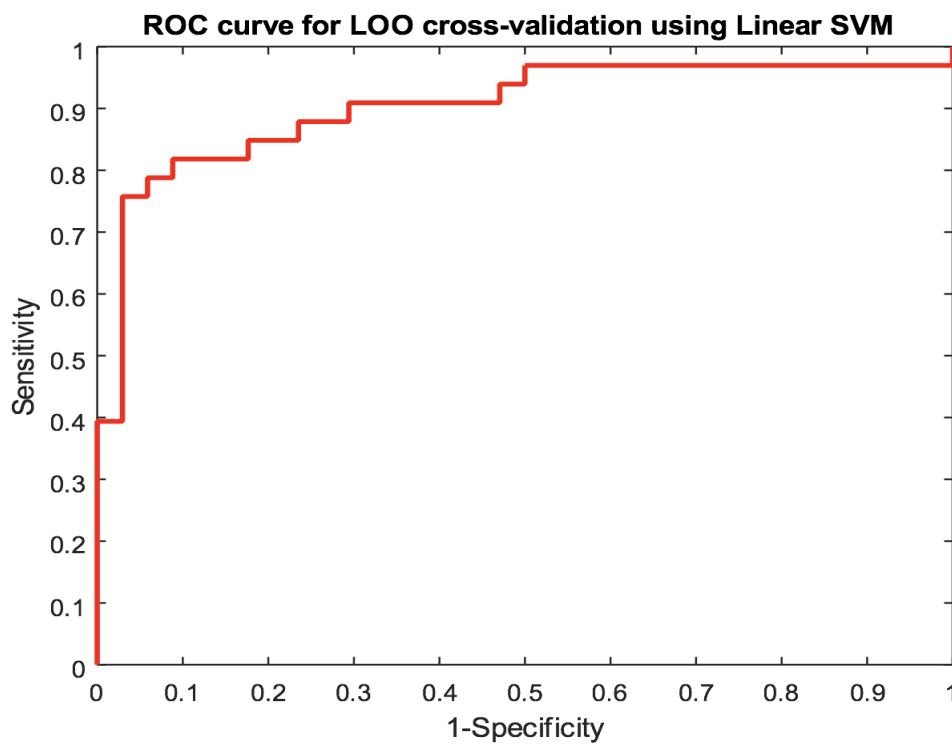
**Figure 47:** Corresponding ROC curve of LOO cross validation of proposed GBM/LG grading. Linear SVM is used for the HG/LG classification.

#### 5.4.6 GBM/LG GRADING IN MR AND VALIDATION WITH DP GRADING

Similarly, the LOO cross-validation for GBM/LG classification is performed using the corresponding images of 67 patients. On an average 88%, and 90% AUC are obtained for MR, and DP grading, respectively. Figure 48 shows the ROC curves following the LOO classifications. All other quantitative scores such as accuracy, sensitivity, specificity, precision, recall, and F-measure are shown in the second and third rows of Table 9 for MR and DP grading, respectively. The results in Figure 48 and Table 9 indicates that the performance of proposed MR-feature based non-invasive glioma grading framework is comparable with that of the invasive DP-based classification of GBM versus LG tumors.



(a)



(b)

**Figure 48:** Corresponding ROC curve of LOO cross validation of proposed GBM/LG grading. Linear SVM is used for both GBM/LG classification in a) MR, b) DP images.

**Table 9:** Quantitative scores, subjects and designs for grading. Results are shown for two different types of grading HG vs LG and GBM vs LG.

Dataset	No. of patients	AUC	Accuracy	Sensitivity	Specificity	Precision	Recall	F-measure
BRATS	HG (124), LG (44)	0.80	0.80	0.96	0.36	0.79	0.98	0.87
TCIA	GBM (33), LG (34)	0.88	0.82	0.85	0.79	0.80	0.85	0.82
TCGA		0.90	0.82	0.82	0.82	0.82	0.82	0.82

## 5.5 DISCUSSION

In this study, an efficient non-invasive glioma grading method is proposed using texture features extracted from structural MRI only. The method is evaluated using multicenter patient images and shows effectiveness in classifying HG/LG and GBM/LG. In the first classification task, it is observed that the performance for glioma grading is somewhat compromised due to possible MRI dataset imbalance and excessive interpolation in the pre-processing steps of BRATS MRI dataset. In the second classification task for GBM/LG grading, the proposed MRI-based method offers good cross-validation performance using that of histopathology images. In summary, while the first classification task is not validated with the non-invasive grading method due to unavailability of the DP images, the overall MR grading performance in both tasks confirms the efficacy of the proposed non-invasive radiomics-based glioma grading. Further study with a balanced dataset and MRIs with less pre-processing artifacts may be needed for improved MRI-based HG/LG tumor grading performance.

## CHAPTER 6

### CONCLUSION AND FUTURE WORKS

#### 6.1 CONCLUSION

This dissertation proposes computational models and experiments for robust segmentation of brain abnormal tissues (tumor and lesions), tracking the change of tumor volume in longitudinal images and grading of brain gliomas using novel texture features in MRIs. Robust segmentation of brain tumor and its different tissues (necrosis, edema, enhanced active, cyst etc.) is one of the requirements for reliable diagnosis and treatment planning to include tumor growth monitoring, dose determination, drug and therapy response monitoring and neuro-surgery. Multiple texture features, both in 2D and 3D, are developed and used to demonstrate the efficacy of BTS and tumor grading in large-scale clinical dataset. The performances of these methods are also compared and cross-validated with state-of-the-art methods. The texture-based computational models proposed in this study are expected to facilitate the clinical management of patients with the brain tumor by automating large scale imaging data analysis, reducing the human error and inter-observer variability and producing repeatable brain tumor quantitation and grading. In Chapter 3, experimental results using a huge multi-center clinical dataset indicate the robustness of the automatic segmentation process for multiclass abnormal tissue segmentation of brain tumor and stroke lesions. The segmentation performances of the proposed methods are competitive with that of state-of-the-art methods as demonstrated by the excellent ranking of our methods in multiple global tissue segmentation Challenges. One of the major contributions of this work is shown in [4], that is, no single segmentation method in the challenge has the best performance in all tissue categories and, hence, fusing the top ranking results may offer superior performance, even close to the manual segmentation. Although the multi-fractal texture-based method shows excellent performance in multi-class tumor tissues [3], further investigation is required to improve performance for lesion segmentation. From findings of the lesion segmentation challenge [89], we observe that multi-center data or changes in acquisition parameters poses serious challenges even for the best performing methods and the performance of these automated methods is still far from that of the manual ratings. From the patient-wise result in [87], it is noticed that the proposed method performs comparatively better for the lesions with a larger size. The overall performance is also compromised by the substantial presence of false positives and this needs further improvement. In order to improve the BTS performance, this study proposes a post-processing method in Chapter 4 using the variation of the tumor texture in the follow-up scans. The study shows that a combination of specific 3D texture features (spin image, RIFT and LBP) can effectively differentiate the tumor volumes from the non-tumors. Experimental

results show that the method is effective in reducing the FPs and may be applicable as a post-processing step for any segmentation method that offers high sensitivity with moderate FP. Scores in Table 8 shows that the method improves the overall performance for all three tumor categories such as core, complete, and enhanced active tumor. One of the purposes of improved tumor segmentation and outlining different tumor tissues (necrosis, edema, active enhanced tumor) is to provide a precise tumor location within its internal tissue compartments for advance diagnosis processes such as tumor growth monitoring in the longitudinal images. In Chapter 4, the volumetric ratios obtained using our method consistently matches with that of manual segmentation over the longitudinal scans. This consistent segmentation performance in longitudinal scans suggests that assessment the pattern of tumor volume changes is possible with the segmented tumor by the proposed method. In Chapter 5, an efficient non-invasive glioma grading method is proposed using texture features extracted from structural MRI only. The method is evaluated using multicenter patient images and shows effectiveness in classifying HG/LG and GBM/LG. In the first classification task, it is observed that the performance for glioma grading is somewhat compromised due to possible MRI dataset imbalance and excessive interpolation in the pre-processing steps of BRATS MRI dataset. In the second classification task for GBM/LG grading, the proposed MRI-based method offers good cross-validation performance using that of histopathology images. In summary, while the first classification task is not validated with the non-invasive grading method due to unavailability of the DP images, the overall MR grading performance in both tasks confirms the efficacy of the proposed non-invasive glioma grading. The overall contributions of this dissertation are summarized in Table 10 below.

## 6.2 FUTURE WORKS

In this dissertation, the analyses of the brain tumors and stroke lesions show complementary and competitive results in segmentation, tracking and grading when compared to state-of-the-art methods. However, few limitations of the work done in this dissertation are also noticed. Future studies are necessary to address these limitations to improve the performance and future clinical applicability of the proposed methods. Future studies are necessary for the following areas.

### 6.2.1 IMPROVEMENT OF THE BTS METHOD

Despite excellent results as demonstrated by the ranking of our methods in competitive challenges, the proposed BTS method offers comparatively higher dice overlap score for larger size tumors in comparison with smaller ones. Furthermore, the presence of substantial false positives outside of the tumor region and anomaly labeling in the tumor core area compromised the overall performance. More investigation for the tumors and stroke lesions with smaller size is required. Therefore, future work includes the study of more effective features and sophisticated feature selection technique. It is also noticed that intensity of the necrosis tissues in the core region are usually below the mean value of the whole image and have a tendency of being misclassified as non-tumor. A sophisticated intensity inhomogeneity correction preferable to address the issue.

**Table 10:** Summary of the research findings related to the proposed methods.

Chapter	Dissertation Goals	Description	Proposed Methods	Outcomes
3	Multi-tissue BTS and lesion segmentation	Multiclass abnormal tissue (edema, necrosis, enhanced and non-enhanced) segmentation.	Novel texture features (mBm, PTPSA). Random Forest (RF) as classifier.	Competitive results when compared with the state-of-the-art methods as demonstrated by results from multiple Challenges [4][5][6][7][63][90].
		Ischemic stroke lesion (sub-acute) segmentation.	Structure tensor based local gradient, mBm, and PTPSA texture features. RF as classifier.	Competitive performance but the overall accuracy needs further improvement as demonstrated by results in the Challenge [64][89].
4	Improved BTS using 3D texture features for tumor volume tracking	Improved BTS in longitudinal MRIs.	Original BTS with longitudinal information, False positive reduction using Spin image, RIFT, LBP feature. Relevance Vector Machine (RVM) and RF as classifier.	Improved tumor segmentation performance in longitudinal images[91].
		Tracking the tumor volume as stable, progress or shrinkage.	Volumetric ratio of different tumor tissues.	Effective tumor growth tracking with consistent tumor segmentation in follow-up images [91].
5	Tumor grading using texture radiomics and its validation using histopathology data	Non-invasive grading using only structural (T1c, T2, Flair) MR images.	Dynamic texture, MF DFA, and mBm features. Support Vector Machine (SVM) as classifier.	Non-invasive glioma grading as HG/LG and GBM/LG are possible using proposed radiomic features [92][93][94].
		Invasive grading in histopathology images.	Cell nuclei morphology with k-mean clustering. SVM as classifier.	Computationally inexpensive and highly efficient glioma grading as GBM//LG in DP images [87][93].

### 6.2.2 EXTEND THE POST-PROCESSING TECHNIQUE

The study shows a complete post-processing method to reduce the FPs for any segmentation method that offers high sensitivity with moderate FP. However, the developed method is designed only for longitudinal MR scans. In future, several extensions of the method can be conducted to include: i) devise the original BTS method to take inputs from both time scans ( $I_t, I_{t'}$ ), where  $I_t$  stands for input features, ii) generalize the proposed method so that single time scan data can also be tested by simply dropping the temporal classifier, and iii) apply the method with small sized stroke or multiple sclerosis lesions.

### 6.2.3 FULL-SCALE STUDY OF TRACKING THE CHANGE OF TUMOR VOLUME

The volumetric ratios obtained using the proposed method shows a good match with that of manual segmentation over the longitudinal scans. This consistent segmentation performance over the longitudinal scans suggests that the change of tumor volume assessment is possible with the segmented tumor by the proposed method. However, one of the major limitations of the proposed pilot study is the smaller sample size. In the experiment, there are only 13 patient samples which are too low to train any machine learning algorithm. Future study can be conducted using more samples for using machine learning schemes.

### 6.2.4 GRADING IN LONGITUDINAL IMAGES

In this study, the developed non-invasive grading method uses the single time point data. However, tumor progress in longitudinal images always offers more insight about the tumor nature. Future study can be conducted using the follow-up scans with 3D texture features such as Spin image, RIFT, and LBP that are already proven effective in tumor versus non-tumor classification in Chapter 4.

### 6.2.5 ADVANCED MICROSCOPIC FEATURES FOR GRADING IN DP IMAGES

The proposed grading scheme in DP images uses only the morphological features of cell nuclei. Although the experimental results show high efficiency and competitive performance with the state-of-the-art methods, there are other microscopic features that offer useful information too. In the future, I plan to include some important features such as the prevalence and divisional stage of mitotic cells, and the spread of necrosis in the tumor region for tumor grading in a more clinical fashion.

## BIBLIOGRAPHY

- [1] “Fact sheet on brain tumor and other central nervous system”  
<http://seer.cancer.gov/statfacts/html/brain.html> Accessed on: July, 10, 2017.
- [2] “Statistics on brain lesions”  
<http://www.stroke.org/> Accessed on: July, 10, 2017.
- [3] “Ischemic Stroke Lesion Segmentation Challenge 2015”,  
<http://www.isles-challenge.org/ISLES2015/> Accessed on: July, 10, 2017.
- [4] B. H. Menze, A. Jakab, S. Bauer, J. Kalpathy-Cramer, K. Farahani, J. Kirby, et al., “The multimodal brain tumor image segmentation benchmark (BRATS),” *IEEE transactions on medical imaging*, vol. 34, no. 10, pp. 1993-2024, 2015.
- [5] A. Islam, S. M. S. Reza, and K. M. Iftekharuddin, “Multi-fractal texture estimation for detection and segmentation of brain tumors,” *IEEE Transactions on Biomedical Engineering*, vol. 60, no. 11, pp. 3204-15, 2013.
- [6] S. Reza and K. M. Iftekharuddin, “Multi-fractal texture features for brain tumor and edema segmentation,” *SPIE Medical Imaging, International Society for Optics and Photonics*, vol. 9035, 2014.
- [7] S. Reza and K. Iftekharuddin, “Multi-class abnormal brain tissue segmentation using texture features,” *Multimodal Brain Tumor Segmentation, Medical Image Computing and Computer Assisted Intervention*, pp. 38-42, 2013. <http://martinos.org/qtim/miccai2013/>
- [8] E. C. Holland, “Progenitor cells and glioma formation,” *Current Opinion in Neurology*, vol. 14, no. 6, pp. 683-688, 2001.
- [9] “The new WHO classification of tumors affecting the central nervous system”  
<https://neurosurgery.mgh.harvard.edu/newwhobt.htm> Accessed on: July, 10, 2017.
- [10] M. Hadziahmetovic, K. Shirai, and A. Chakravarti, “Recent advancements in multimodality treatment of gliomas,” *Future Oncology*, vol. 7, no. 10, pp. 1169-1183, 2011.
- [11] K. M. Iftekharuddin, W. Jia, and R. Mash, “Fractal analysis of tumor in brain MR images,” *Machine Vision and Applications*, vol 13, no. 5, pp. 352-362, 2003.
- [12] S. Ahmed, K. Iftekharuddin, and A. Vossough, “Efficacy of texture, shape, and intensity feature fusion for posterior-fossa tumor segmentation in MRI,” *IEEE Transactions on Information Technology in Biomedicine*, vol 15, no. 2, pp. 206-213, 2011.
- [13] L. Breiman, “Random forest,” *Machine Learning*, vol. 45, no. 1, pp. 5-32, 2001.
- [14] A. E. Johnson, and M. Hebert, “Using spin images for efficient object recognition in cluttered



- 3D scenes," *IEEE Transactions on Pattern Analysis and Machine Intelligence*, vol. 21, no. 5, pp. 433-449, 1999.
- [15] S. Lazebnik, C. Schmid, and J. Ponce, "A sparse texture representation using local affine regions," *IEEE Transactions on Pattern Analysis and Machine Intelligence*, vol. 27, no. 8, pp. 1265-1278, 2005.
- [16] B. S. He, F. Zhu, and Y. G. Shi, "Medical image segmentation," *Advanced Materials Research*, vol. 760, pp. 1590-1593, 2013.
- [17] G. Zhao and M. Pietikainen, "Dynamic texture recognition using local binary patterns with an application to facial expressions," *IEEE Transactions on Pattern Analysis and Machine Intelligence*, vol. 29, no. 6, pp. 915-928, 2007.
- [18] G. Doretto, D. Cremers, P. Favaro, and S. Soatto, "Dynamic texture segmentation," *IEEE International Conference on Computer Vision*, vol. 2, pp. 1236-1242, 2003.
- [19] F. Soares, P. Andruszkiewicz, M. Freire, P. Cruz, and M. Pereira, "Self-similarity analysis applied to 2D breast cancer imaging," *International Conference on Systems and Networks Communications*, pp. 77, 2007.
- [20] J. Barker, A. Hoogi, A. Depeursinge, and D. L. Rubin, "Automated classification of brain tumor type in digital pathology images using local texture patches," *Medical Image Computing and Computer Assisted Intervention, Brain Tumor Digital Pathology Challenge*, pp. 5-8, 2014.
- [21] Y. Xu, Z. Jia, F. Zhang, Y. Ai, M. Lai, and E. I-Chao Chang, "Deep convolutional activation features for large brain tumor histopathology image classification," *Medical Image Computing and Computer Assisted Intervention, Brain Tumor Digital Pathology Challenge*, pp. 25-29, 2014.
- [22] J. Kong, L. A. Cooper, F. Wang, J. Gao, G. Teodoro, L. Scarpace, and D. J. Brat, "Machine-based morphologic analysis of glioblastoma using whole-slide pathology images uncovers clinically relevant molecular correlates," *PloS One*, vol. 8, no. 11, pp. e81049, 2013.
- [23] C. H. Lee, M. Schmidt, A. Murtha, A. Bistriz, J. Sander, and R. Greiner, "Segmenting brain tumor with conditional random fields and support vector machines," *Lecture Notes in Computer Science*, vol. 3765, pp. 469-478, 2005.
- [24] J. J. Corso, A. L. Yuille, N. L. Sicotte, and A. W. Toga, "Detection and segmentation of pathological structures by the extended graph-shifts algorithm," *Medical Image Computing and Computer Aided Intervention*, vol. 1, pp. 985-994, 2007.
- [25] K. Popuri, D. Cobzas, A. Murtha, and M. Jagersand, "3D variational brain tumor segmentation using Dirichlet priors on a clustered feature set," *International Journal of Computer Assisted Radiology and Surgery*, vol. 7, no. 4, pp. 493-506, 2012.
- [26] T. Leung and J. Malik, "Representing and recognizing the visual appearance of materials

- using three-dimensional textons,” *International Journal of Computer Vision*, vol. 43, no. 1, pp. 29 – 44, 2001.
- [27] D. Zikic, B. Glocker, E. Konkolglu, J. Shotton, A. Criminisi, D. H. Ye, C. Demiralp, O. M. Thomas, T. Das, R. Jena, and S. J. Price, “Context-sensitive classification forests for segmentation of brain tumor tissues,” *Medical Image Computing and Computer Aided Intervention-BRATS*, pp. 1-9, 2012.
- [28] S. Bauer, T. Fejes, J. Slotboom, R. Weist, L. P. Nolte, and M. Reyes, “Segmentation of brain tumor images based on integrated hierarchical classification and regularization,” *Medical Image Computing and Computer Aided Intervention-BRATS*, pp. 10-13, 2012.
- [29] E. Geremia, B. H. Menze, and N. Ayache, “Spatial decision forest for glioma segmentation in multi-channel MR images,” *Medical Image Computing and Computer Aided Intervention-BRATS*, pp. 14-18, 2012.
- [30] N. Tustison, M. Wintermark, C. Durst, and B. Avants, “ANTs and Árboles,” *Medical Image Computing and Computer Aided Intervention-BRATS*, pp. 47-50, 2013.
- [31] R. Meier, S. Bauer, J. Slotboom, R. Wiest, and M. Reyes, “A hybrid model for multimodal brain tumor segmentation,” *Medical Image Computing and Computer Aided Intervention-BRATS*, pp. 31-37, 2013.
- [32] S. Bauer, T. Fejes, J. Slotboom, R. Wiest, L. P. Nolte, and M. Reyes, “Segmentation of brain tumor images based on integrated hierarchical classification and regularization,” *Medical Image Computing and Computer Aided Intervention-BRATS*, pp. 31-37, 2012.
- [33] D. M. Ghoneim, G. Toussiant, J. Constans, and J.D. Certains, “Three dimensional texture analysis in MRI: A preliminary evaluation in gliomas,” *Magnetic Resonance Imaging*, vol. 21, no. 9, pp. 983-987, 2003.
- [34] C. Pachai, Y. M. Zhu, J. Grimand, M. Hermier, A. D. Badin, A. Boudraa, G. Giemenez, C. Confavreux, and J. C. Froment, “A pyramidal approach for automatic segmentation of multiple sclerosis lesions in brain MRI,” *Computerized Medical Imaging and Graphics*, vol. 22, no. 5, pp. 399-408, 1998.
- [35] A. Pitioit, A. Toga, N. Avache and P. Thomson, “Texture based MRI segmentation with a two-stage hybrid neural classifier,” *International Joint Conference on Neural Networks*, vol. 3, pp. 2053-2058, 2002.
- [36] A. Derntl, C. Plant, P. Gruber, et al., “Stroke lesion segmentation using a probabilistic atlas of cerebral vascular territories,” *International Workshop on Brainlesion: Glioma, Multiple Sclerosis, Stroke and Traumatic Brain Injuries*, pp. 21-32, 2015.
- [37] F. Forbes, S. Doyle, D. Garcia-Lorenzo, C. Barillot, and M. Dojat, “Adaptive weighted fusion of multiple MR sequences for brain lesion segmentation,” *IEEE International Symposium on Biomedical Imaging: From Nano to Macro*, pp. 69-72, 2010.
- [38] Y. Kabir, M. Dojat, B. Scherrer, F. Forbes, and C. Garbay, “Multimodal MRI segmentation

- of ischemic stroke lesions,” *International Conference of the IEEE Engineering in Medicine and Biology Society*, pp. 1595-1598, 2007.
- [39] A. L. Martel, S. J. Alder, G. S. Delay, P. S. Morgan, and A. R. Moody, “Measurement of infarct volume in stroke patients using adaptive segmentation of diffusion weighted MR Images,” *International Conference on Medical Image Computing and Computer-Assisted Intervention*, pp. 22-31, 1999.
- [40] O. Maier, M. Wilms, J. von der Gablentz, U. M. Krämer, and H. Handels, “Ischemic stroke lesion segmentation in multi-spectral MR images with support vector machine classifiers,” *SPIE Medical Imaging, Computer-Aided Diagnosis, International Society for Optics and Photonics*, vol. 9035, pp. 903504, 2014.
- [41] O. Maier, M. Wilms, J. von der Gablentz, U. M. Krämer, H. Handels, et al., “Extra tree forests for sub-acute ischemic stroke lesion segmentation in MR sequences,” *Journal of Neuroscience Methods*, vol. 240, pp. 89-100, 2015.
- [42] N. Chitphakdithai, V. L. Chiang, and J. S. Duncan, “Tracking metastatic brain tumors in longitudinal scans via joint image registration and labeling,” *International Workshop on Spatio-temporal Image Analysis for Longitudinal and Time-Series Image Data*, vol. 240, pp. 124-136, 2012.
- [43] C. Elliott, S. Francis, D. Arnold, D. Collins, and T. Arbel, “Bayesian classification of multiple sclerosis lesions in longitudinal MRI using subtraction images,” *Medical Image Computing and Computer-Assisted Intervention*, vol. 240, pp. 290-297, 2010.
- [44] E. D. Angelini, J. Delon, A. B. Bah, L. Capelle, and E. Mandonnet, “Differential MRI analysis for quantification of low grade glioma growth,” *Medical Image Analysis*, vol. 16, no. 1, pp. 114-126, 2012.
- [45] L. Weizman, L. B. Sira, L. Joskowicz, D. L. Rubin, K. W. Yeom, S. Constantini, et al., “Semiautomatic segmentation and follow-up of multicomponent low-grade tumors in longitudinal brain MRI studies,” *Medical Physics*, vol. 41, no. 5, 2014.
- [46] S. Bauer, J. Tessier, O. Krieter, L. P. Nolte, and M. Reyes, “Integrated spatio-temporal segmentation of longitudinal brain tumor imaging studies,” *International Medical Image Computing and Computer-Assisted Intervention Workshop on Medical Computer Vision*, pp. 74-83, 2013.
- [47] E. Alberts, G. Charpiat, Y. Tarabalka, T. Huber, M. A. Weber, J. Bauer, C. Zimmer, and B. H. Menze, “A nonparametric model for brain tumor segmentation and volumetry in longitudinal MR sequences,” *International Medical Image Computing and Computer-Assisted Intervention Workshop on Brain Lesion*, 2015.
- [48] Z. Karimaghloo, H. Rivaz, D. L. Arnold, D. L. Collins, and T. Arbel, “Temporal hierarchical adaptive texture CRF for automatic detection of gadolinium-enhancing multiple sclerosis Lesions in brain MRI,” *IEEE Transactions on Medical Imaging*, vol. 34, no. 6, pp. 1227-1241, 2015.

- [49] M. A. Weber, S. Zoubaa, M. Schlieter, E. Juttler, H. B. Huttner, K. Geletneky, C. Ltrich, M. P. Lichy, A. Kroll, J. Debus, F. L. Giesel, M. Hartmann, and M. Essig, "Diagnostic performance of spectroscopic and perfusion MRI for distinction of brain tumors," *Neurology*, vol. 66, no. 12, pp. 1899-1906, 2006.
- [50] Q. Wang, E. K. Liacouras, E. Miranda, U. D. Kanamalla, and V. Megalooikonomou, "Classification of brain tumors using MRI and MRS data," *SPIE Medical Imaging, Computer-Aided Diagnosis, International Society for Optics and Photonics*, vol. 6514, 2007.
- [51] E. I. Zacharaki, S. Wang, S. Chawla, D. S. Yoo, R. Wolf, E. R. Melhem, and C. Davatzikos, "Classification of brain tumor type and grade using MRI texture and shape in a machine learning scheme," *Magnetic Resonance in Medicine*, vol. 62, no. 9, pp. 1609-1618, 2009.
- [52] N. Tustison and J. Gee, "N4ITK: Nick's N3 ITK implementation for MRI bias field correction," *The Insight Journal*, 2010.
- [53] L. G. Nyul, J. K. Udupa, and X. Zhang, "New variants of a method of MRI scale standardization," *IEEE Transaction on Medical Imaging*, vol. 19, no. 2, pp. 143-150, 2000.
- [54] J. Kleesiek, A. Biller, G. Urban, U. Kothe, M. Bendszuz, and F. Hamprecht, "Ilastik for multi-modal brain tumor segmentation," *Medical Image Computing and Computer Aided Intervention-BRATS*, pp. 12-17, 2014.
- [55] K. M. Iftexharuddin, S. Ahmed, R. J. Ogg, and F. H. Laningham, "Efficacy of texture, shape and intensity features for robust posterior-fossa tumor segmentation in MRI," *SPIE Medical Imaging, International Society for Optics and Photonics*, vol. 2009, pp. 726020-1, 2009.
- [56] B. B. Mandelbrot, "The fractal geometry of nature," *New York: WH Freeman*, vol. 173, 1983.
- [57] S. Arseneau, "Tutorial and Demonstration of the uses of structure tensors using gradient representation",  
<http://www.cs.cmu.edu/~sarsen/structureTensorTutorial/> Accessed on: July, 10, 2017.
- [58] H. Peng, F. Long, and C. Ding, "Feature selection based on mutual information criteria of max-dependency, max-relevance, and min-redundancy," *IEEE Transactions on Pattern Analysis and Machine Intelligence*, vol. 27, no. 8, pp. 1226-1238, 2005.
- [59] M. Wiener and A. Liaw, "Classification and regression by random forests," *R News*, vol. 2, no. 3, pp. 18-22, 2002.
- [60] A. Criminisi, J. Shotton, and E. Konukoglu, "Decision forests: A unified frame-work for classification, regression, density estimation, manifold learning and semi-supervised learning," *Foundations and Trends® in Computer Graphics and Vision*, vol. 7, no. 2-3, pp. 81-227, 2012.
- [61] "Multimodal brain tumor segmentation (BRATS) 2013",  
<https://vsd.unibe.ch/WebSite/BRATS/Start2013/> Accessed on: January, 10, 2014.

- [62] “Multimodal brain tumor segmentation (BRATS) 2014”,  
<https://sites.google.com/site/miccaibrats2014/>. Accessed on: November 10, 2014.
- [63] S. M. S. Reza, A. Islam, and K. M. Iftekharuddin, “Texture estimation for abnormal tissue segmentation in brain MRI,” *The Fractal Geometry of the Brain*, Springer New York, pp. 333-349, 2016.
- [64] S. M. S. Reza, L. Pei, and K. M. Iftekharuddin, “Ischemic stroke lesion segmentation using local gradient and texture features,” *Medical Image Computing and Computer Aided Intervention-Workshop on Ischemic Stroke Lesion Segmentation*, pp. 21-24, 2015.
- [65] “Ischemic stroke lesion segmentation (ISLES) 2015”,  
<https://www.virtualskeleton.ch/ISLES/Start2015> . Accessed on: January 20, 2016.
- [66] D. G. Lowe, “Distinctive image features from scale-invariant keypoints,” *International Journal of Computer Vision*, vol. 60, no. 2, pp. 91-110, 2004.
- [67] M. Pietikäinen, A. Hadid, G. Zhao, and T. Ahonen, “Local binary patterns for still images,” *Computer Vision Using Local Binary Patterns*, Springer London, pp. 13-47, 2011.
- [68] H. Ling and K. Okada, “An efficient earth mover’s distance algorithm for robust histogram comparison,” *IEEE Transactions on Pattern Analysis and Machine Intelligence*, vol. 29, no. 5, pp. 840–853, 2007.
- [69] M. E. Tipping, “Sparse Bayesian learning and the relevance vector machine,” *Journal of Machine Learning Research*, vol. 1, no. Jun, pp. 211–244, 2001.
- [70] “Code for relevance vector machine (RVM)”,  
<https://github.com/covartech/PRT/blob/master/class/prtClassRvm.m>. Accessed on: January 20, 2017.
- [71] Y. Rubner, C. Tomasi, and L. J. Guibas, “The earth mover’s distance as a metric for image retrieval,” *International Journal of Computer Vision*, vol. 40, no. 2, pp. 99–121, 2000.
- [72] “Multimodal brain tumor segmentation (BRATS)-2015”,  
<https://www.smir.ch/BRATS/Start2015>. Accessed on: January 10, 2016.
- [73] “Code for earth movers distance (EMD)”,  
<http://www.mathworks.com/matlabcentral/fileexchange/22962-the-earth-mover-s-distance>. Accessed on: January 10, 2016.
- [74] “MATLAB tutorial on *perfcurve* for optimal thresholding on ROC”,  
<https://www.mathworks.com/help/stats/perfcurve.html>. Accessed on: January 10, 2016.
- [75] “The image data in The Cancer Imaging Archive (TCIA)”,  
<http://www.cancerimagingarchive.net/>. Accessed on: January 10, 2016.
- [76] “The image data in The Cancer Genome Atlas (TCGA)”,  
<http://cancergenome.nih.gov/>. Accessed on: January 10, 2016.

- [77] G. F. Gu and W. X. Zhou, "Detrended fluctuation analysis for fractals and multifractals in higher dimensions," *Physical Review E*, vol. 74, no. 6, pp. 061104, 2006.
- [78] J. W. Kantelhardt, S. A. Zschiegner, E. Koscielny-Bunde, S. Havlin, A. Bunde, and H. E. Stanley, "Multifractal detrended fluctuation analysis of nonstationary time series," *Physica A: Statistical Mechanics and its Applications*, vol. 316, no. 1, pp. 87-114, 2002.
- [79] G. Doretto and S. Soatto, "Editable dynamic textures," *IEEE Computer Society Conference on Computer Vision and Pattern Recognition*, vol. 2, pp. II-137, 2003.
- [80] P. Saisan, G. Doretto, Y. N. Wu, and S. Soatto, "Dynamic texture recognition," *IEEE Computer Society Conference on Computer Vision and Pattern Recognition*, vol. 2, pp. 58-63, 2001.
- [81] A. W. Fitzgibbon, "Stochastic rigidity: Image registration for nowhere-static scenes," *IEEE International Conference on Computer Vision*, vol. 1, pp. 662-670, 2001.
- [82] S. Soatto, G. Doretto, and Y. N. Wu, "Dynamic textures," *IEEE International Conference on Computer Vision*, vol. 1, pp. 439-446, 2001.
- [83] L. Yuan, F. Wen, C. Liu, and H. Y. Shum, "Synthesizing dynamic texture with closed-loop linear dynamic system," *European Conference on Computer Vision*, pp. 603-616, 2004.
- [84] F. J. Ferri, P. Pudil, M. Hatef, and J. Kittler, "Comparative study of techniques for large-scale feature selection," *Pattern Recognition in Practice IV*, pp. 403-413, 1994.
- [85] Y.W. Chang, C.J. Hsieh, K.W. Chang, M. Ringgaard, and C.J. Lin, "Training and testing low-degree polynomial data mappings via linear SVM," *Journal of Machine Learning Research*, vol. 11, no. Apr, pp. 1471-1490, 2010.
- [86] Y. W. Chang and C. J. Lin, "Feature ranking using linear SVM," *Causation and Prediction Challenge*, pp. 53-64, 2008.
- [87] S. M. S. Reza, and K. M. Iftexharuddin, "Glioma grading using cell nuclei morphologic features in digital pathology images," *SPIE Medical Imaging, International Society for Optics and Photonics*, vol. 9785, 2016.
- [88] "The BEER-LAMBERT Law",  
<http://www.chemguide.co.uk/analysis/uvvisible/beerlambert.html>. Accessed on: January 10, 2015.
- [89] O. Maier, B. H. Menze, J. von der Gablentz, L. Häni, M. P. Heinrich, M. Liebrand, D. Christiaens, et al., "ISLES 2015-A public evaluation benchmark for ischemic stroke lesion segmentation from multispectral MRI," *Medical Image Analysis*, vol. 35, pp. 250-269, 2017.
- [90] S. Reza and K. M. Iftexharuddin, "Improved brain tumor tissue segmentation using texture features," *Medical Image Computing and Computer Aided Intervention-BRATS*, pp. 27-30, 2014.
- [91] S. M. S. Reza, J. Chen, and K. M. Iftexharuddin, "Longitudinal brain tumor volume

segmentation and tracking using 3D temporal hierarchical texture features in MRI,” (*Under Preparation*).

- [92] S. M. S. Reza, M. D. Samad, K. A. Jones, and K. M. Iftekharuddin, “Texture-based radiomics for glioma grading and validation using histopathology images,” (*Under Preparation*).
- [93] S. M. S. Reza, R. Mays, and K. M. Iftekharuddin, “Multi-fractal detrended texture feature for brain tumor classification,” *SPIE Medical Imaging, Computer-Aided Diagnosis, International Society for Optics and Photonics*, vol. 9414, pp. 22, 2015.
- [94] S. M. S. Reza, R. Mays, and K. M. Iftekharuddin, “Multifractal detrended fluctuation analysis shows promise for brain tumor grading,” *Imaging and Applied Optics, Technical Digest (online), Optical Society of America, IW4C.5*, 2014.

## VITA

Syed Mohammad Shamim Reza  
Department of Electrical and Computer Engineering  
Old Dominion University  
Norfolk, VA 23529

Syed M. S. Reza received his B.S. degree in Electrical and Electronic Engineering from the Bangladesh University of Engineering and Technology in 2007. In Fall 2011, he started his Ph.D. program in the ECE Vision Lab at Old Dominion University. The motivation of his current research is to develop computational modeling to facilitate the clinical management of patients with the brain tumors and stroke by automating large scale imaging data analysis, reducing the human error, inter-observer variability and producing repeatable brain tumor quantitation and grading. Prior to his graduate studies, he taught electrical engineering courses at the undergraduate level for two years at the Presidency University in Dhaka, Bangladesh. He also worked as Radio Network Design engineer at LM Ericsson Bangladesh Limited. His research interest include medical image analysis, machine learning, and computer vision.